2015

Graphene Based Heterojunctions for Nano-Electronic and Sensing Applications

Md A. Uddin
University of South Carolina - Columbia

GRAPHENE BASED HETEROJUNCTIONS FOR NANO-ELECTRONIC AND SENSING APPLICATIONS

by

Md Ahsan Uddin

Bachelor of Science
University of Dhaka, 2009

Master of Science
University of Dhaka, 2010

Master of Science
University of Notre Dame, 2011

Submitted in Partial Fulfillment of the Requirements

For the Degree of Doctor of Philosophy in

Electrical Engineering

College of Engineering and Computing

University of South Carolina

2015

Accepted by:

Goutam Koley, Major Professor

Mohammod Ali, Committee Member

MVS Chandrashekhar, Committee Member

Thomas Vogt, Committee Member

Lacy Ford, Vice Provost and Dean of Graduate Studies

ACKNOWLEDGEMENTS

First, I would like to thank my advisor, Prof. Goutam Koley for endless support and patient guidance throughout my graduate study and research. Prof. Koley gave me the opportunity to conduct cutting-edge research in the area of graphene and related materials, always encouraged me to think and improvise new ideas and gave me freedom to pursue those. I have been extremely benefited from his training on scientific writing which would be helpful for my future career.

I thank and appreciate my PhD committee members, Prof. Ali, Dr. Chandrashekhar, and Prof. Vogt for their valuable suggestions and insightful questions for my research work. I am grateful to Prof. Ali and Prof. Vogt for taking the hassle and rearranging their schedule to accommodate my proposal defense within a very short notice.

I would like to express my gratitude to Prof. Sudarshan, who generously allowed me to use his clean room facility without which I would not be able to fabricate my devices. I would also like to thank Dr. Chandrashekhar for giving me his valuable time frequently to answer all the questions both related to research as well as for troubleshooting of various equipment in cleanroom. His suggestion about the impedance spectroscopy related study and allowing me to use the set-up is particularly important for chapter 5 of this dissertation. I am also grateful to Prof. Webb from Physics for allowing access to his lab facilities and for the collaboration on magneto-transport study described in chapter 6.

I would like to thank Dr. Voevodin at Air Force Research laboratory (AFRL), for providing the BN samples. Without the access of Raman spectroscopy set-up at Prof. Williams lab in Chemical Engineering, it would have been really difficult to carry out graphene related research. I would like to thank Dr. Ghoshroy and stuffs at electron microscopy center, for their help.

I would also like to express my gratitude to past and present members of Dr. Koley's lab, Dr. Chandra's lab, Dr. Sudarshan's lab, Dr. Webb's lab who have been always helpful to me throughout my graduate study and research. Particularly, I thank Amol for helping me out with various measurements and processing. Together we solved many problems. I really appreciate for the help of Bochen (Physics) regarding Hall measurement and Nick Glavin (AFRL) for BN samples. I am really grateful to the friends from Bangladeshi student community and faculty members at University of South Carolina, who made my stay at Columbia bearable. A big thanks also goes to staff at the department of Electrical Engineering specially Nat, Ashley, Alicia to help me out in administrative works.

Finally, I would like to express my gratitude to my family members, who have always been a source of encouragement and provided guidance throughout my life.

ABSTRACT

Graphene, an atomically thin and semi-metallic two dimensional material, has been extensively researched over the past decade due to its superior intrinsic carrier velocity, electrical and chemically tunable work function, ability to form layered heterostructure with other materials, and relevant potential applications in electronics, sensing, optoelectronics, energy storage, etc. However, the confinement of charge carriers within one atomic layer results in an electrical transport that is extremely sensitive to the surrounding environment, which is beneficial for sensing applications, but at times unfavorable for electronic applications due to scattering from extrinsic impurities. In addition, due to its rather delicate structure, engineering a high quality gate dielectric without altering its characteristic electronic structure while enabling optimal surface passivation and gate control is one of the major challenges for graphene device development.

Hexagonal Boron Nitride (hBN) has emerged as a possible option to meet the challenges, and has been exploited to alter graphene electronic structure by intentional crystallographic misalignment between the layers at the time of transfer or synthesis. The variation in electronic structure by hBN is possible due to its unique properties such as inert surface, similar hexagonal and nearly lattice matched structure with graphene

and high surface optical phonon modes. Low temperature Pulsed laser deposition (PLD) grown amorphous BN on SiO_2/Si, phase transformed to hBN by forming gas annealing, has been employed for graphene device application. Graphene field effect transistor (FET) fabricated from layered heterostructure of graphene/hBN on SiO_2/Si exhibited electrical performance enhancement over graphene on SiO_2/Si substrate in terms of mobility, carrier inhomogeneity and extrinsic doping.

In a parallel effort, taking advantage of graphene's tunable work function, a novel genre of sensor based on noble metal nanoparticle functionalized graphene/Si heterojunction Schottky diode has been developed for sensing non-polar H_2, and enhancing response for polar NH_3 molecular species. Reverse bias operation of the diode sensor exhibited orders of magnitude higher response compared to graphene FET based sensors due to exponential change in reverse current originated from interface barrier height change. The reverse bias operation also allows low power operation and modulation of the Fermi level of graphene, which can lead to the tuning of sensitivity and expansion of the dynamic range. Impedance Spectroscopic analysis of the diode sensor has been carried out to understand the underlying current transport mechanism. Fitting the impedance spectra for different gaseous exposure conditions with an equivalent circuit model, the changes in junction resistance and capacitance have been extracted. Along with these two parameters, experimentally obtained 3-dB cut off frequency for each gas exposure has been utilized for multimodal sensing by the diode sensor.

Finally, temperature dependent magneto-transport study of PdH_x passivated graphene has been carried out to elucidate the effect of metal nanoparticle assisted doping and molecular adsorption on graphene electrical transport properties. It has been observed

from the systematic study that, the dominant scattering mechanism in bilayer graphene switched from coulomb scattering to thermal excited surface optical phonon scattering after PdH_x passivation, and Hall mobility exhibited significant enhancement at the measurement temperature range of 298 to 10 K. Due to recent interests in exploiting metallic nanoparticles as dopant for 2D crystals, as well as enhancing sensitivity of chemical sensors and photodetectors, the findings are significant and would pave the way for future research efforts in this area.

TABLE OF CONTENTS

LIST OF FIGURES

CHAPTER 1

INTRODUCTION

Graphene, a two-dimensional (2D) allotrope of sp^2 bonded carbon atoms, has drawn huge research interests since its discovery in 2004 [1] due to its extraordinary material properties including remarkably high charge carrier mobility in the range of 10^5 to 10^6 cm^2/Vs [2, 3], very high thermal conductivity [4], and mechanical strength [5], as well as high degree of chemical inertness at room temperature. In addition several other exciting properties such as optical transparency [6], superior intrinsic carrier velocity, electrical and

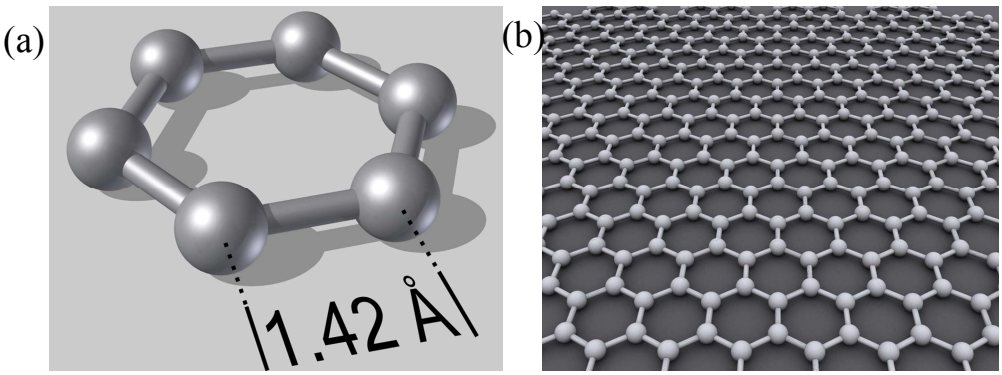

Figure 1.1 (a) Schematic representation of single planner hexagon consisting of 6 C atoms connected to each other by sp^2 bonding with C-C bond length of 1.42 Å [13]. (b) Periodic repetition of hexagonal unit resulting in 2-dimensional honeycomb structure of graphene [13].

chemically tunable work function [7], and possibility of heterostructure with other 3D/2D/1D materials [8], etc. made it really attractive for novel applications. With unique combination of all these characteristics, graphene appeared as one the possible alternatives

to surpass the obstacles faced by the conventional semiconductor based electronic applications. The atomically thin nature of graphene means that injected charge carriers are confined to a surface just one atom thick (~0.34 nm). In principal, this alone may allow graphene-based devices to push the limits of device scaling beyond those of silicon and other conventional semiconductor by enabling improved gate control and, opening up the possibility of new device paradigm such as low power and high speed, vertical and in-plane Schottky devices and tunneling transistors by forming multilayer heterostructures with other lower dimensional semiconductors. The 2D nature of graphene coupled with delocalized π electrons resulting from sp^2 hybridization in C-C bond makes it highly suitable for sensing applications. The 2D nature makes it essentially a surface (as seen in

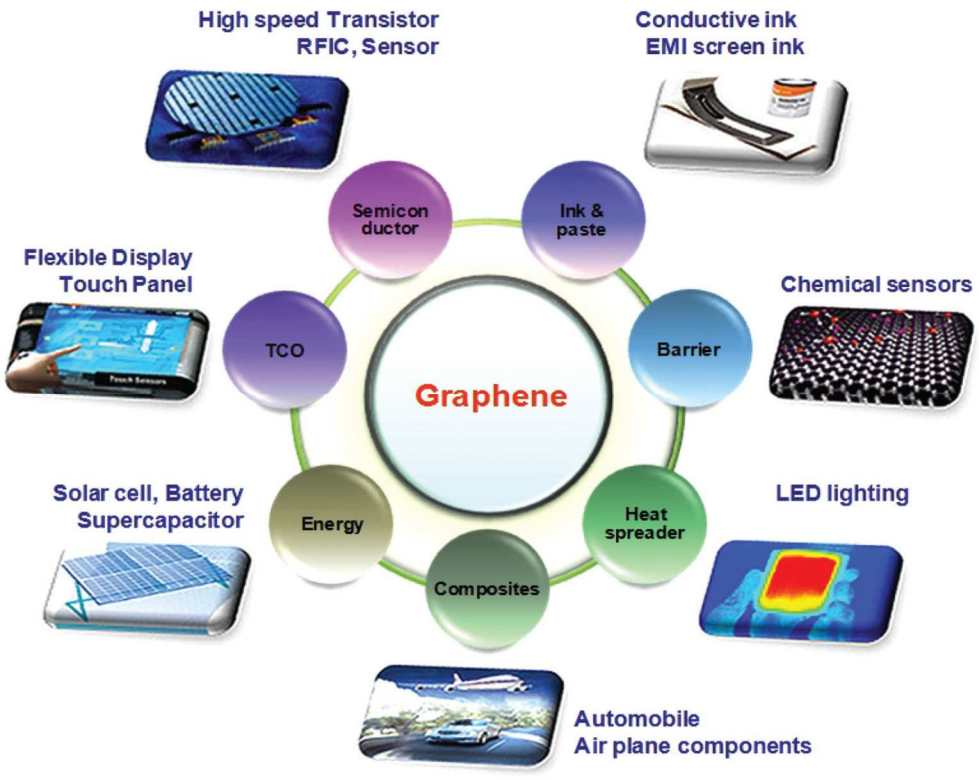

Figure 1.2 Overview of graphene applications in different sectors ranging from chemical sensors to light emitting devices, composites, energy, touch panels and high frequency electronics [12]

Fig 1.1), enabling analyte molecules to adsorb very efficiently and produce the maximum change in its physical properties. On the other hand, the presence of delocalized π electrons makes it sensitive to a large variety of analytes that can adsorb on its surface and exchange charge with it or modify its surface properties. The noise characteristics of graphene have also been very impressive in the range of 10^{-9} to 10^{-7} Hz^{-1} when compared with carbon nano tubes [9]. In general graphene shows very low 1/f and thermal noise [10]. These exceptional material properties have led to the demonstration of graphene based sensors that are capable of detecting down to a single analyte molecule [11]. The combination of various amazing properties of the graphene enables its application in variety of diverse

Table 1.1 Graphene Enabled Potential Technologies and Applications

features	Enabled applications / technologies	Impact
Atomic thinness	Flexible devices; thin and flexible electronic components; modular assembly / distribution of portable thin devices	Spectrum of new forms of devices, thus enabling new concepts of integration and distribution
Foldable material	Engineering new materials by stacking different atomic planes or by varying the stacking order of homogeneous atomic planes	
All-surface material	Engineering novel 2d crystals with tuneable physical/chemical properties by control of the surface chemistry. Platform for new chemical /biological sensors	Realization of new (non-existing so far) materials, which properties could be engineered and customized for new applications
Solution - processable	Novel composite materials with outstanding physical properties (*e.g.* high thermal conductivity, κ; high Young modulus and tensile strength); Novel functional materials	
High carrier mobility (μ)	Ultra-high frequency electronic devices	New highly-performing devices available at low cost and large scale, thus allowing major step forwards in many social impact fields (*e.g.* environmental monitoring, communications, health / medical applications, etc)
Optical (saturable) absorption; photo-thermoelectric effect	Novel optoelectronic and thermoelectric devices; photodetectors	
Field-effect sensitivity	Highly sensitive transducers	
High intrinsic capacitance; high specific surface area (SSA)	Outstanding supercapacitors	Significant steps forward in the realization of sustainable devices and green-energy systems
Photovoltaic effect, broad-range optical transparency; photocatalytic effects	Energy conversion; energy harvesting; self-powered devices	
Theoretically predicted "chiral superconductivity"	High Tc superconductors	New devices based on yet experimentally unexplored physics
Dirac fermions; pseudospin	Valleytronics	

areas (Fig 1.2) such as terahertz devices, high speed transistors, displays, batteries, ultracapacitors, hydrogen storage, solar cells, membrane for separation of gases, magnetic, charge, strain, and biological sensors, composites etc. to name a few [12]. This list has been ever expanding as new applications come to light by choosing, mixing and matching the properties of graphene alone or with combination with other materials. Table 1.1 shows the possible applications and impacts in a wide range of fields enabled by graphene's excellent properties [12].

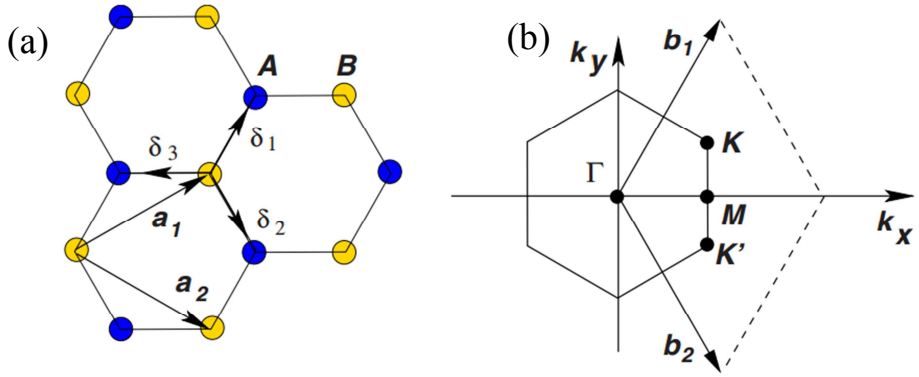

Figure 1.3 Hexagonal lattice of graphene and Brillouin zone. (a) The 2D lattice of graphene consisting of two triangular lattices (shown as A & B) interpenetrating each other. **a1** and **a2** are unit lattice vectors. (b) The Brillouin zone of graphene showing K & K' as location of Dirac cones [13].

1.1 Electronic Structure of Graphene

The physical and chemical properties of materials is determined by their crystal structure and electronic structure. Many unique properties of graphene are tightly linked to its 2D crystalline nature and the resulting band structure. In 2D crystalline hexagonal lattice of graphene, each carbon atom is connected to nearest neighbors through characteristic C-C bond length, a = 1.42Å [Fig 1.1(b)] and each atom has 3 nearest neighbors in a plane [Fig 1.1(b)] and shares a sp^2 hybridized σ bond with them. The forth orbital, p_z consisting

of single electron, is in z direction which is perpendicular to the graphene plane, and is responsible for conductivity in graphene. These p_z electrons from each carbon atom hybridize to form π and π^* bands which give rise to many peculiar electronic properties of graphene [13]. The unit cell and corresponding reciprocal lattice of graphene is shown in Figure 1.3 [13]. The unit cell consists of two interpenetrating triangular lattice shown by A and B type atoms.

The basis of unit cell consists of two atoms. The lattice vectors, and reciprocal lattice vectors are given by Equation 1.1 and 1.2.

$$\boldsymbol{a_1} = \frac{a}{2}\left(3, \sqrt{3}\right), \quad \boldsymbol{a_2} = \frac{a}{2}\left(3, -\sqrt{3}\right) \qquad (1.1)$$

$$\boldsymbol{b_1} = \frac{2\pi}{3a}\left(1, \sqrt{3}\right), \quad \boldsymbol{b_2} = \frac{2\pi}{3a}\left(1, -\sqrt{3}\right) \qquad (1.2)$$

From this lattice structure, the energy dispersion relationship of graphene can be determined by invoking tight binding model or linear combination of atomic orbitals (LCAO) following the original work of Wallace in 1947 [14].

In order to obtain dispersion relationship we need to consider the interaction of carbon atoms to nearest and next nearest neighboring carbon atoms. As seen from Figure 1.1(a) each carbon atom has 3 nearest and 6 next nearest neighbors. The hopping of p_z electron is possible to nearest site (from A to B) or next nearest site (A to A). The interaction energy involved is given by t ~ 2.9 eV for A to B hopping and t' ~ 0.1 eV for A to A atoms hopping. Solving the Hamiltonian for unit cell with assumption of only nearest neighbor interaction being important, the dispersion relation is given by the following expression.

$$E(\boldsymbol{k}) = \pm t\sqrt{3 + 2\cos\left(\sqrt{3}k_y a\right) + 4\cos\left(\frac{\sqrt{3}}{2}k_y a\right)\cos\left(\frac{3}{2}k_x a\right)} \qquad (1.3)$$

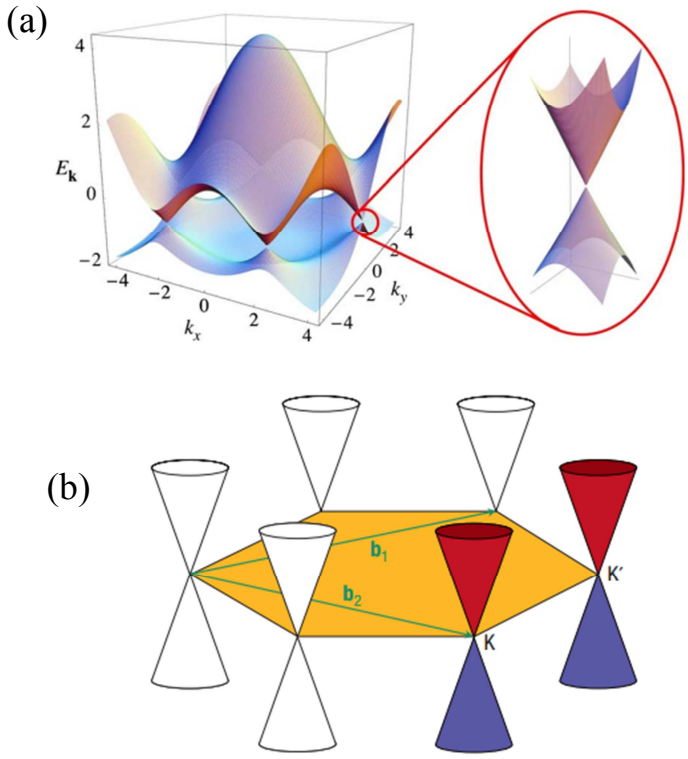

Figure 1.4 (a) Energy bands in monolayer graphene in the units of t = 2.7 eV (the nearest neighbor hopping energy). The upper band is conduction band and lower one is valence band. The blown up diagram shows linear relationship close to Dirac point where conduction band and valance band meet. (b) Low-energy electronic structure of graphene showing 6 Dirac points such points of contact. Two distinct corners of Brillouin zone are shown as K and K' [14, 15].

Where **k** is reciprocal lattice vector. The positive term in Equation 1.3 corresponds to conduction band and negative is for valence bands as plotted in Figure 1.4(a) appears linear near low energy points in reciprocal lattice space called as Dirac point. The conduction band and valence band touch each other at these Dirac point at 6 places [15] on the corner of a graphene's Brillouin zone [Figure 1.4(b)] referred as K and K' points with the following position vectors in the reciprocal space.

$$\boldsymbol{K} = \left(\frac{2\pi}{3a}, \frac{2\pi}{3\sqrt{3}a}\right); \boldsymbol{K}' = \left(\frac{2\pi}{3a}, -\frac{2\pi}{3\sqrt{3}a}\right) \qquad (1.4)$$

The dispersion relation at K and K' points and within ±1 eV vicinity of the Dirac point is given by the following linear relationship.

$$E(\boldsymbol{k}) = \pm\hbar v_F|\boldsymbol{k}| = \pm v_F\sqrt{k_x^2 + k_y^2} \qquad (1.5)$$

where, v_F is Fermi velocity given by

$$v_F = \frac{3at}{2\hbar} \approx 0.9 \times 10^6\ m/s \qquad (1.6)$$

This linear dispersion relationship at low energy makes charge particles (electrons and holes) move with v_F, as described by Equation 1.6, which is close to relativistic velocity. Therefore electrons and holes close to Dirac point in graphene is called as Dirac fermions. This is in stark contrast with most of the bulk semiconductors which exhibit parabolic dispersion relationship at low energies. The linear dispersion relationship of graphene is also responsible for properties like vanishing density of states (DOS) at Dirac points. The DOS in graphene is given by equation 1.7 [16].

$$DOS = {}^{E}/_{2\pi\hbar^2 v_F^2} \qquad (1.7)$$

The zero band gap state of graphene at Dirac point is called intrinsic state. Therefore the intrinsic graphene refers to a state at which graphene has minimal charge carriers.

1.2 Electronic Transport and Field Effect Behavior of Graphene

Electric field applied perpendicular to graphene plane can induce charge carriers, electrons or holes, also referred as electric field effect. The Fermi level (E_F) can move up in conduction band inducing electrons, and can move down in valance band inducing holes depending upon the direction of the field. This results in ambipolar nature of graphene channel. In absence of externally applied electric field, the E_F should ideally be coinciding with the zero Dirac point in graphene according to Equation 1.7. However in graphene channel there is always finite charge present due to either thermal generation or induction

due to impurities at graphene and substrate interface even in absence of applied electric field. For this reason the threshold voltage beyond which graphene based field effect transistor can turn on or off does not really exist. The minimum to maximum current ratio in graphene based FETs remains in the range to 5-10 and hence render them unsuitable for switching application despite of their high mobility values. On the other hand, the charge carrier type in graphene channel can be easily tuned by applying electric field at an

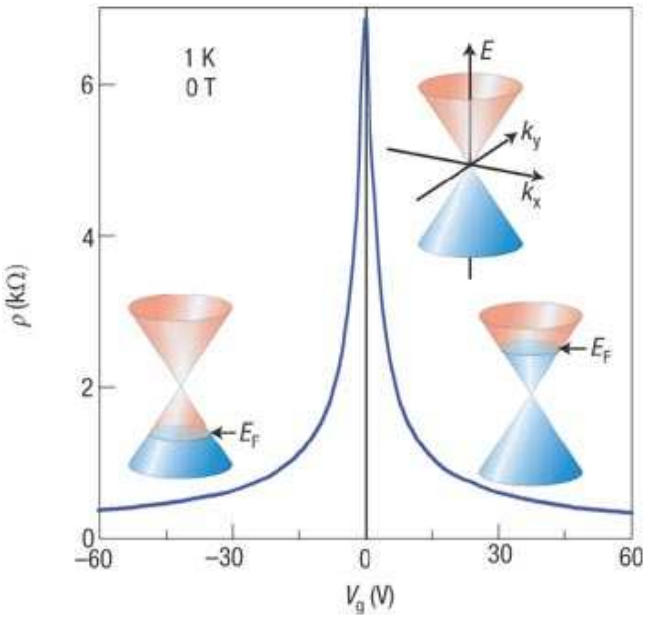

Figure 1.5 Ambipolar response of a single-layer pristine graphene [1]. The Fermi level E_F is located at Dirac point for $V_g = 0$V. At negative V_g the E_F is below Dirac point and for positive V_g, E_F goes above it.

insulated gate as shown in Figure 1.5 [1].

The main scattering mechanisms limiting the mobility in graphene are phonon scattering [17], Coulomb scattering [18], and short range scattering [19] primarily due to defects such vacancies and cracks in graphene. Due to heavy dependence of these scattering mechanisms in graphene the mobility is strongly dependent upon the quality of graphene and underlying substrates. For instance at room temperature surface polar

phonons and defects are two major scattering mechanism for monolayer graphene on SiO_2. The typical mobility values of pristine graphene on SiO_2 ranges from 10000 to 15000 cm^2/Vs [20]. These mobility numbers are much higher in those reported in conventional semiconductors and ever higher than 2D electron gas systems. Removing the substrates or using the one free from trapped charges has been shown to improve the mobility. Engineering extreme growth and process steps mobility can be enhanced several orders, such as, graphene nano-ribbon transistor fabricated from epitaxial graphene grown on etched sidewalls of (0001) surfaces of SiC exhibited mobility close to 10^7 cm^2/Vs [3].

In pristine graphene the current minimum is at zero gate bias, however, in most of the practical devices, non-zero Dirac point is observed indicating the presence of unwanted extrinsic doping. Due to presence of disorder in graphene in the form of defects, impurities, ripples etc. produces fluctuations in the graphene's electrostatic potential. These fluctuations become significant at the Dirac point where their screening is weak due to low charge density. The fluctuations in charge density has been proposed to be electron-hole puddles which have also been observed in scanning probe methods on graphene/SiO_2 samples [21]. This behavior has been attributed to the experimental observation of minimum conductivity of graphene in the range of $4e^2/h$ even though DOS approaches to zero at Dirac point. The other claim for the observation of minimum conductivity is the presence of impurities concentration in SiO_2 [22].

1.3 Present Status, Opportunities and Challenges

Despite of being highly promising material for various kind of applications graphene still remains a comparatively new material. It therefore offers many challenges to be solved like any other new material system such as nitride semiconductors before it

could become a commercial success. Among the major challenge graphene faces are growth, reasonable transport properties in terms of mobility, contacts, suitable gate dielectric, etc. Growing device quality, large area graphene still remains a challenge for mass production. Two approaches appears promising, namely epitaxial and chemical vapor deposition bases graphene growth.

Epitaxial growth is well established for producing large area graphene of high quality by thermal annealing of SiC wafers [23]. This method takes advantage of well-established SiC epitaxy, 6-H or 4-H polytype of SiC is heated in the temperature range of 1200 – 1600 ^{o}C in ultra-high vacuum (UHV) of 1×10^{-10} Torr for several minutes. At this high temperature Si leaves the SiC surface owing to its higher vapor pressure than carbon. The remaining C rich surface then rearranges on the hexagonal lattice of SiC to generate single to few-layer graphene [24]. The major advantage of this technique is growth of quite uniform, wafer scale and high quality graphene is possible, taking advantage of the precise control of process parameters in a commercial SiC growth chamber. One of the disadvantages of this method of graphene synthesis is that it is very difficult to remove or transfer the graphene to another desired substrate, due to the challenges involved in controllably etching SiC. Therefore, processing of graphene devices needs to be done on the SiC substrate itself. This can be expensive due to the high cost of SiC substrates, and also it does not readily allow the usage of a back gate for realizing transistors, or sensors requiring back-gate modulation and integration with majority of current semiconductor technologies including industry work horse Si CMOS process, is much tougher. Due to these reasons, chemical vapor deposition (CVD) method appeared as an alternative growth technique where graphene is widely grown on either Cu or Ni substrate and subsequently

transferred on the substrate as needed depending on the nature of device and applications [25]. Recently, Van Der Waals epitaxy of other layered semiconductor employing CVD [26] appeared as very exciting opportunity with the prospect of achieving vertical and/or in-plane Schottky and tunneling devices.

The other major challenge graphene offers is careful control of its properties since it is one atom thick therefore its properties are highly affected by its environment and surroundings. Thus, there is a need to understand and develop better fabrication technique which would allow preserving its distinctive properties. Initial proof of concept device demonstrations were done by fabricating devices on oxidized heavily doped Si which is also used as back gate, is still one of the major device fabrications methods for its versatility. Even for large scale device fabrication, there has been lots of challenges [27] in case of graphene devices on any substrate including SiO_2/Si such as graphene transfer from growth catalyst metal foil to the substrate with minimum damage, graphene adhesion with substrate, reduction of impurity concentration and extrinsic doping, minimizing the carrier scattering for better electrical transport, etc.

Atomically thin nature of graphene means that injected charge carriers are confined to a surface just one atom thick (~0.3 nm). In principal, this alone may allow graphene-based devices to push the limits of device scaling beyond those of silicon and other conventional semiconductors by enabling improved gate control and forming multilayer heterostructures with other lower dimensional semiconductors. However, the extreme confinement means that charge carriers are also directly exposed to the surrounding environment, making transport through graphene highly sensitive to scattering from extrinsic impurities. This sensitivity has presented a serious engineering challenge to

realizing high-performance devices that take full advantage of graphene's intrinsic qualities. Graphene has no native oxide layer and has a chemically inert surface with no dangling bonds, making it difficult to integrate dielectric passivation without chemically altering the graphene surface and degrading the transport properties of the graphene channel. The fundamental challenge in the development of graphene field-effect transistors has been engineering a dielectric that provides optimal capacitive coupling to the gate, while also minimizing degradation of device performance [28].

To meet these challenges, we need both bottom substrate and top dielectric which has similar crystal lattice structure both in terms of type and lattice constant to reduce strain and extrinsic doping, similar phonon mode for better heat dissipation and less scattering, inert surface like graphene such that growth or incorporation as top dielectric should not change graphene's functionalities, with sufficiently high dielectric constant for capacitive coupling to gate and minimize the coulomb scattering, high thermal conductivity for better heat dissipation, better surface optical phonon characteristics, etc. Hence, dielectric engineering is one of the major bottleneck for both development and integration of graphene based devices.

Due to its two-dimensional (2D) nature that makes it essentially a surface, and very high carrier mobility [1], graphene is especially suited for sensing applications [11]. Although it has excellent sensitivity to a large variety of polar molecules, (i.e. NO_2 and NH_3) it is insensitive to most non-polar molecules, such as H_2, with which it does not exchange charge. A surface functionalization is therefore necessary for detecting these non-polar molecules. It has been demonstrated that surface functionalization of graphene by catalytically active noble metals (such as Pd and Pt) leads to charge transfer between

graphene and the metal hydride formed in presence of H_2 facilitating its detection [29-31]. Of these, only the chemically synthesized graphene nanoribbon network based sensor has so far shown good H_2 sensitivity (producing ~55% change in resistance for 40 ppm H_2), while others showed much lower sensitivity in the range of few percent for tens of ppm H_2 exposure and long response time. Thus, better sensor in terms of sensitivity, sensing tunability, response and recovery time, power consumption is very important to realize graphene's complete potential. Recent demonstration of graphene/Si Schottky heterojunction [32], and its usage in several devices from solar cells [33-34] to "barristors" [7] have opened up the possibility for developing a new class of "chemi-diode" sensors. Due to the atomically thin and semimetalic nature of graphene, its Fermi level can be easily modulated by electrical, optical or chemical means which in-turn changes the Schottky barrier height (SBH) at the heterointerface. Since the reverse saturation current is exponentially proportional to SBH change, sensor based on graphene/Si Schottky diode would provide new paradigm in 2D material based sensors.

In addition to realizing novel sensing paradigm, it is important to understand the inherent mechanism. Since the sensing mechanism is dominated by electrical transport, how different device component responds to the sensing condition and quantifying those changes is necessary to obtain efficient sensing mechanism. For that, we might even need specialized electrical spectroscopic technique which would help to get better insight as well as new sensing parameters. Besides this, modelling the electrical response analytically with representative parameters for different device components and extrapolating the relevant change would help in achieving multimodal sensing archetype. Finally, analyzing the

change in all the experimental and theoretical parameters would help even selective sensing of analytes.

Metal nanoparticle (NP) functionalization of 2D materials and its effect on device characteristics and sensing has attracted significant attention recently, since this method can change the doping of atomically thin materials [35], enhance sensitivity of sensors by higher adsorption [36], boosting photosensitivity due to electromagnetic scattering [37], etc. However, there has not been any comprehensive study of the effect of NP decoration and subsequent sensing on fundamental electrical properties such as mobility, carrier concentration, scattering mechanism, etc. This sort of study is very essential to improve the sensor performance which might even lead to new applications based on conventional and non-conventional semiconductor materials and devices.

1.4 Outline of the Dissertation

In this dissertation, CVD method has been used to grow high quality, large area, single and bilayer graphene on cupper foil for the investigation of graphene based electronic and sensing devices. Chapter 2 started with CVD graphene growth steps including substrate preparation, annealing and final growth phase, etc. Raman spectroscopy is a non-invasive technique for structural characterization which is used to assess the quality of graphene. Details of graphene transfer on arbitrary substrate utilizing widely used PMMA assisted aqueous transfer method is described next. Fabrication process for graphene field effect transistor and other electrical characterization test structures such as Transmission Line Method (TLM) patterns for contact, Hall Bars for magneto-transport study, etc. has been developed for CVD graphene which can be extended to any other 2D material. Electrical characterization of CVD graphene on SiO_2/Si substrate to study field effect mobility, Hall

mobility, metal contacts, etc. have been performed and processing steps has been included for improvement.

In chapter 3, Pulsed Laser Deposition (PLD) grown boron nitride (BN) [38] has been introduced as an alternative substrate and dielectric for graphene electronics due to certain unique characteristics which would help to achieve better performance of graphene based devices. Low temperature growth of BN is described along with elemental and structural analysis such as XPS, Raman, AFM, etc. Afterwards, graphene device fabrication on BN, electrical characterization, and comprehensive analysis has been performed along with comparative study of electrical transport properties on SiO_2 substrate.

In chapter 4, the sensing response of catalytically active noble metal functionalized Graphene/Si Schottky diode H_2 sensor is presented. The sensor operated in reverse bias, takes advantage of the exponential change in current due to SBH change, and exhibits several times higher sensitivity compared to the best performance of graphene based chemiresistor type H_2 sensor functionalized similarly. The reverse bias operation also allows modulation of the Fermi level of graphene depending on the magnitude of the bias, which can lead to the tuning of sensitivity of the sensor and expansion of the dynamic range. Another advantage of the reverse bias operation of the sensor is its low power requirement due to low steady state current in the range of μA flowing in reverse bias.

In chapter 5, dc amperometric measurement of graphene/p-Si Schottky diode has been carried out to study the *Polar* gaseous molecular (NH_3) sensitivity enhancement by noble metal (Pt, Pd and Ag) nano-particle functionalization. To understand the sensing mechanism AC impedance spectroscopy (IS) has been used as a sensing measurement

technique. In addition to the dc amperometric measurement, analyzing the IS response utilizing an equivalent circuit model, the change in junction capacitance and resistance has been obtained for both polar NO_2 and NH_3, and non-polar H_2 gaseous species. Finally, change in 3dB cut-off frequency for each gas exposure has been utilized as a sensing parameter. The mentioned parameters have been compared for all three molecular species to obtain multimodal sensing methodology.

In chapter 6, temperature dependent electrical transport study of CVD graphene in Hall geometry has been carried out at different condition: as fabricated, after Pd NP deposition and subsequent H_2 exposure to study the effect of graphene electrical properties such as mobility for NP functionalization and in H_2 environment. Hall measurement of single layer graphene showed increase in mobility with decrease in temperature, which implies that substrate surface optical phonon scattering is the dominant scattering mechanism. For bilayer graphene, Hall mobility increases with temperature in the range of 10 - 298 K, indicating Coulomb scattering is the most prevailing scattering mechanism. Mobility reduced after 2 nm Pd NP deposition on bilayer graphene. However, with H_2 exposure, temperature dependent Hall mobility of the Pd-functionalized bilayer graphene enhances significantly and the dominant scattering mechanism switched to thermal excited surface optical phonon scattering. In chapter 7, the dissertation research is summarized and possible future direction is discussed briefly.

CHAPTER 2

GRAPHENE GROWTH, MATERIAL AND ELECTRICAL CHARACTERIZATION

The chapter starts with detailed discussion on developed CVD graphene synthesis procedure including substrate preparation, annealing and final growth phase, etc. for high quality, large area, single and bilayer graphene growth on cupper foil for the investigation of graphene based electronic and sensing devices. Structural and material characterization of as grown and transferred graphene has been carried out by Raman spectroscopy, scanning electron microscopy (SEM) and atomic force microscopy (AFM). Graphene transfer on arbitrary substrate by PMMA supporting layer in aqueous medium is discussed. Fabrication process for graphene field effect transistor and other electrical characterization test structures such as Transmission Line Method (TLM) patterns for contact, Hall Bars for magnetotransport study, etc. for CVD graphene is described subsequently. Electrical characterization of CVD graphene on SiO_2/Si substrate to study field effect mobility, Hall mobility, metal contacts, etc. have been carried out and improvised processing steps is included for performance enhancement.

2.1 Chemical Vapor Deposition Growth of Graphene

Chemical vapor deposition (CVD) involves the activation of gaseous reactants or precursors and the subsequent chemical reaction, followed by the formation of a stable solid deposit over a suitable substrate. The energy for the chemical reaction can be supplied by different sources such as heat, light, or electric discharge as in thermal, laser-assisted, or plasma-assisted CVD respectively. Two types of reactions could be possible for the deposition process namely homogeneous gas-phase reactions, which occur in the gas phase and may results in formation of powders, and heterogeneous chemical reactions which occur on or near a heated surface leading to the formation of powders or films. Though CVD can be used to produce ultrafine powders, but in case of depositing extremely thin graphene films heterogeneous chemical reactions should be favored and homogeneous chemical reactions are avoided during the designed experiments. The CVD technique of graphene growth has assumed prominence due to its ability to grow large area, monolayer, low defect graphene on inexpensive substrates such as cold rolled, high-purity (99.999%), 25 μm thick Cu foils using inexpensive CVD growth hardware and operational cost. Cu substrate has proved to be excellent candidate for making large-area, uniform thickness (95%) monolayer graphene due to the low solubility of C in Cu [1].

The CVD setup consists of the three gas cylinders, each for CH_4, H_2 and Ar connected to the corresponding mass flow controllers (MFC) through manual valves and ¼" stainless steel tubing. The stainless steel tubing serves to provide higher conductance path and better leak characteristics as compared to polyethylene tubing. The MFCs were MKS Type 1179A each calibrated for the gas being used. Ar MFC was 1000 sccm range for flow larger amount of Ar and a carrier and diluent gas. H_2 and CH_4 MFCs were 200

Figure 2.1 The home-build CVD graphene growth system

and 50 sccm range for keeping CH_4 to H_2 ratio low during the growth. The output from MFCs are joined together using a Swagelok Union Cross. One end of the cross is connected to the ¼" quartz delivery tube by a stainless steel bellows. The reaction chamber consist of 1½" diameter wide and 2' long quartz tube. It is also fitted with ¼" thick compressed BN heat blocker at both the ends. The enclosure is formed by stainless steel end caps with sleeves. The sample or substrate is mounted on a flat quartz boat. The other end of the chamber has one outlet connected to stainless steel tubing with bellows. A barometer and a Pirani gauge (MKS 901P, loadlock transducer) are attached downstream to this stainless tubing to monitor the pressure of the system. This tubing then connects to the inlet of a mechanical pump. The mechanical pump is a rotary vane pump from Pfeiffer Vacuum (Model: Duo 10 M) with a capability of 4.5 mTorr ultimate pressure. However the base system pressure remains in the range of 100 mTorr. The outlet of the pump is connected to room exhaust line though a manual valve which keep the CVD system isolated from exhaust and saves from occasional oil leak of other pumps which are also connected to

exhaust. The quartz tube reactor is housed inside a horizontal single zone split tube furnace from Carbolite. This furnace is capable of operating at 1100 °C for prolonged hours and takes about 45 min to reach that temperature. The temperature is controlled by Carbolite 301 controller. Split furnace was chosen to have a faster cooling rate which has bearing in Ni based CVD and also to cut-down process time. Figure 2.1 shows the picture of this home built graphene CVD system where precursor gas cylinders and mechanical pumps are not in the frame. The picture shows stainless steel tubing, MFCs, their controller and read-outs, horizontal split-tube furnace and its controller, quartz tube reactor fitted with stainless steel ends caps, pressure gauge and read-out etc.

Graphene growth has been optimized on copper (Cu) foil, which acts as the catalyst for growth. The distinct advantage of using Cu over other transition metals (as for example, Ni) for graphene growth, low solubility of C atoms in Cu (< 0.001 atoms % at 1000℃) results in high quality single or bilayer graphene growth on Cu. The sample preparation

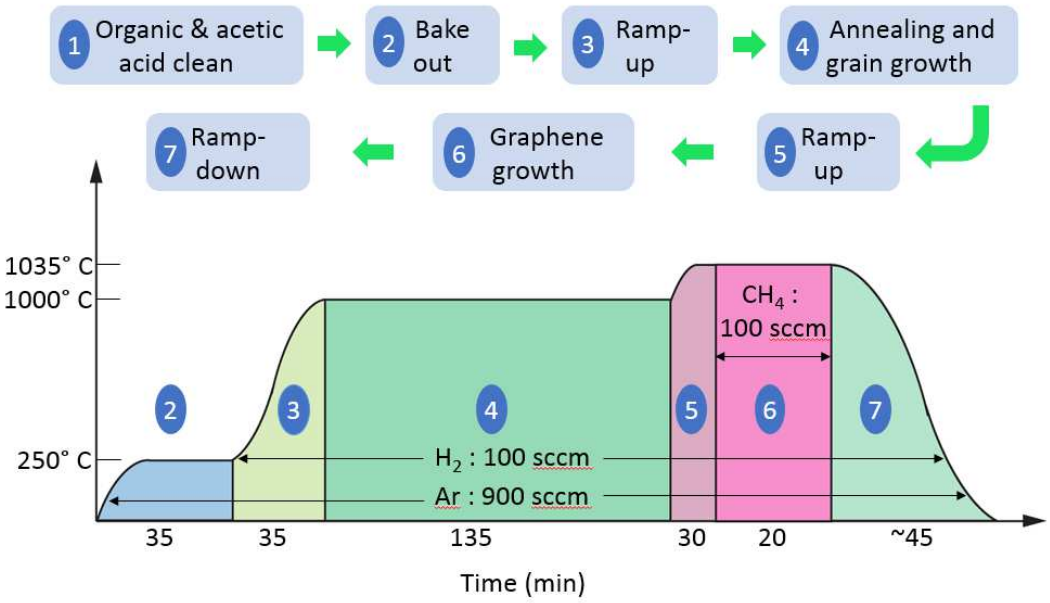

Figure 2.2. Series of steps involved in growing monolayer graphene on Cu foils. The optimized process parameters are shown in the schematic plot.

involves a good cleaning procedure for getting rid of copper oxides such as CuO and Cu_2O which are present in Cu foils. The Cu foils were first cleaned in acetone and isopropanol, and then sonicated in acetic acid to remove oxide. After loading the Cu foil under Ar over pressure, the growth chamber was evacuated and then Ar was flown at 250℃ for bake out. H_2 was flown for 2 hours at 1000℃ to anneal Cu to increase its crystalline quality and remove any remaining and newly formed oxide. The actual growth was performed at further elevated temperature of 1035℃ in presence of CH_4. Figure 2.2 shows the optimized process parameter and sequence of steps for our thin (mono and bi-layer) graphene growth.

2.2 Structural and Material Characterization of Graphene

In order to understand the type and quality of CVD graphene and to device the strategy to improve the CVD, a reliable and quick feedback is very important. In case of graphene, Raman spectroscopy provides quick and immediate feedback on as-grown graphene on metal catalyst without any need for sample preparation [2]. Raman spectroscopy is based upon vibrational spectrum of a material system. It is sensitive to strain and can detect stress in the semiconductor in very small region due to the ability of focusing light beam in very small region [3]. For our study, LabRAM 1B from Horiba Raman Spectrometer has been used.

The Raman peaks of interest in graphene material system for routine characterization lies in the Raman shift range of 1200 to 3000 cm^{-1}. The prominent peaks in the Raman spectra of graphene system are G, D and 2D bands occurring at ~1580, 1350 and ~2700 cm^{-1}, respectively as shown in Figure 2.3 [4]. The G band corresponds to doubly degenerate in-plane transverse optic (iTO) and longitudinal optic (LO) phonon mode that corresponds to E_{2g} symmetry at the Brillouin zone canter [5]. Physically speaking, it result

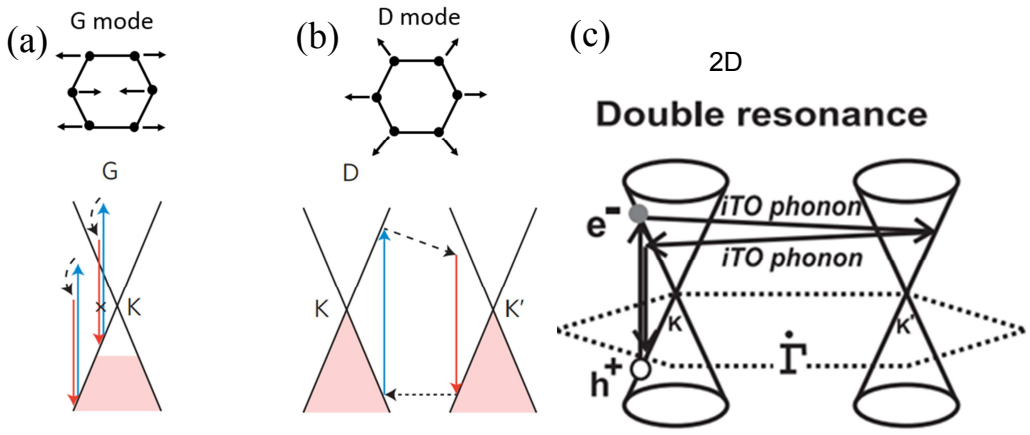

Figure 2.3 (a) G band resulting from in-plane C-C band stretching of the ring and is characteristic of sp^2 carbon system. Electron excitation and phonon generation is shown as resonance process in the E-k diagram of graphene. (b) The radial breathing mode responsible for D peak. It involves inter-valley phonon and defect scattering [4]. (c) A two-phonon second-order Raman spectral processes giving rise to the 2D band.

from bond stretching of all pairs of sp^2 atoms both in rings and chains as seen in Figure 2.3(a) [4]. It is the only band that occurs from first order Raman scattering process in the graphene. The presence of G peak confirms the presence of carbonaceous material with sp^2 bonding and its intensity is proportional to the thickness of the carbonaceous material.

There is defect related peak in graphene referred as D. The D band corresponds to the double resonance radial breathing modes of sp^2 bonded atoms in the ring [Figure 2.3(b)] [5]. This band is Raman forbidden and only occur when the periodicity of hexagonal lattice is broken by a point defect, grain boundary, line defect, graphene edge, dopant atom etc. The other prominent band 2D, shown in Figure 2.3(c), results from a second order scattering process that involves double resonance and two iTO phonons near K point. Since D band involves one iTO phonon and a defect, the 2D band gets its name for being overtone of D band which means ω_{2D} is about twice the ω_D. It helps in determining the number of monolayers present in the sample, based upon shape and width of 2D band. After rigorous

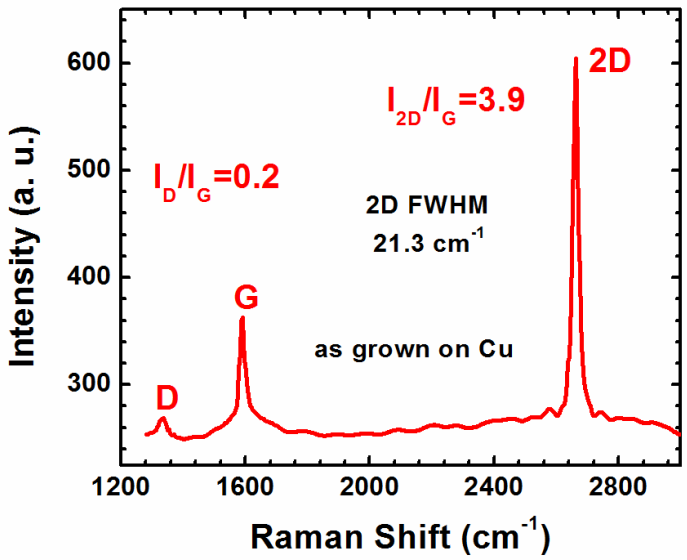

Figure 2.4 Raman spectra of graphene as-grown on Cu foils by CVD growth technique. The I_{2D}/I_G of 3.9 and 2D FWHM of 21.3 cm^{-1} is indicative of monolayer graphene.

optimization (parameters shown in Figure 2.2) single layer graphene has been grown routinely for different device and sensing applications. Figure 2.4 shows the Raman spectrum of as grown graphene samples on Cu. The I_D/I_G ratios of less than 0.2 indicates good quality of the graphene with very low defect density [6]. The I_G/I_{2D} ratio of 3.9 and the shape of 2D peak characterized by single Lorentzian peak with full width at half maximum (FWHM) of ~21.33 cm^{-1} indicates the presence of single layer graphene [2].

AFM image of graphene on SiO_2/Si substrate is shown in Figure 2.5(a) where the PMMA residues are visible along with few wrinkles just after transfer without any annealing. It has been demonstrated that with vacuum or forming gas annealing at 300 - 400 °C, significant amount of PMMA residue evaporates and graphene becomes much cleaner [7]. Figure 2.5(b) is showing the false colored SEM image of suspended graphene over the trench formed on SiO_2/Si substrate, exhibiting structural uniformity and monolayer thickness.

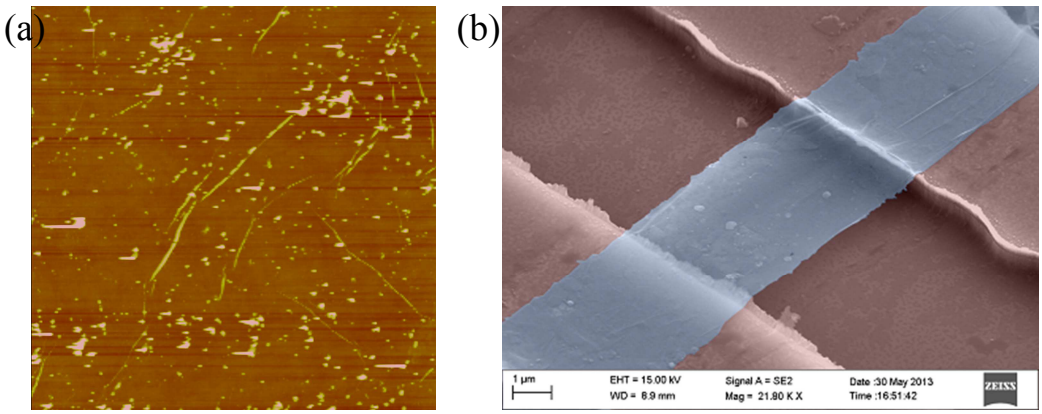

Figure 2.5 (a) $20 \times 20\ \mu m^2$ AFM image of transferred graphene on SiO_2/Si without annealing is showing PMMA residue and wrinkles. (b) False color SEM image of suspended graphene over the trench formed on SiO_2/Si substrate showing uniform structural quality and monolayer thickness.

2.3 Graphene transfer

In CVD based graphene growth on transition metal catalyst, the grown graphene cannot be used directly. It needed to be transferred on a desired substrate for all possible characterization and device fabrication. In our graphene growth on Cu foil it grows on both sides and the bottom side graphene is in general inferior quality as compared to the one gown on the top side of the foil. The top side graphene is protected by spin coating of poly methyl methacrylate (PMMA) twice at 2000 rpm for 40 sec resulting in approximately 800 nm thickness of film. It also provides mechanical strength to graphene in the subsequent processing steps. The PMMA coated sample is loaded upside down in reactive ion etching (RIE) chamber upside down in order to expose the bottom graphene layer. This graphene layer is removed by O_2 plasma at 150 W RF power and 300 mTorr pressure for 180 sec. The sample is then kept in concentrated Cu etchant over night for complete removal of Cu. Both $FeCl_3$ and $(NH_4)_2S_2O_8$ (ammonium persulfate) have been used. This results in graphene/PMMA layer floating in the etchant and resultant byproducts. The floated

graphene is rinsed multiple times in deionized water (DI). A desired substrate can then be slid underneath the floating graphene/PMMA and scooped off from the liquid solution. The substrate containing transferred graphene/PMMA is allowed to dry in air and then baked at 220 ˚C above the glass transition temperature of PMMA to allow its reflow in order to

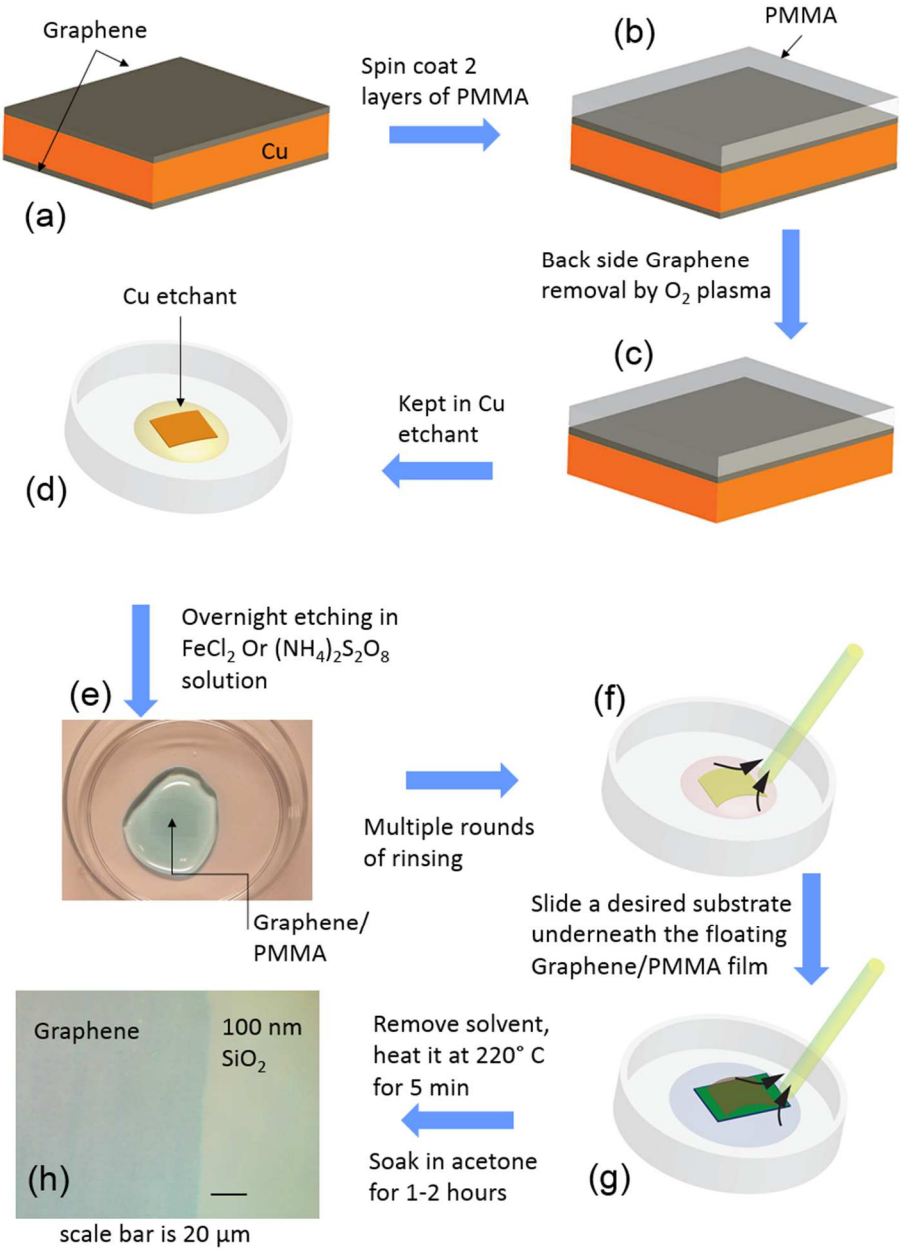

Figure 2.6 Processing steps for graphene transfer on any desirable substrate.

reduce the wrinkles in graphene originated while transfer on substrate. The sample is then dipped in acetone for 2-3 hours to remove PMMA from top of transferred graphene. This

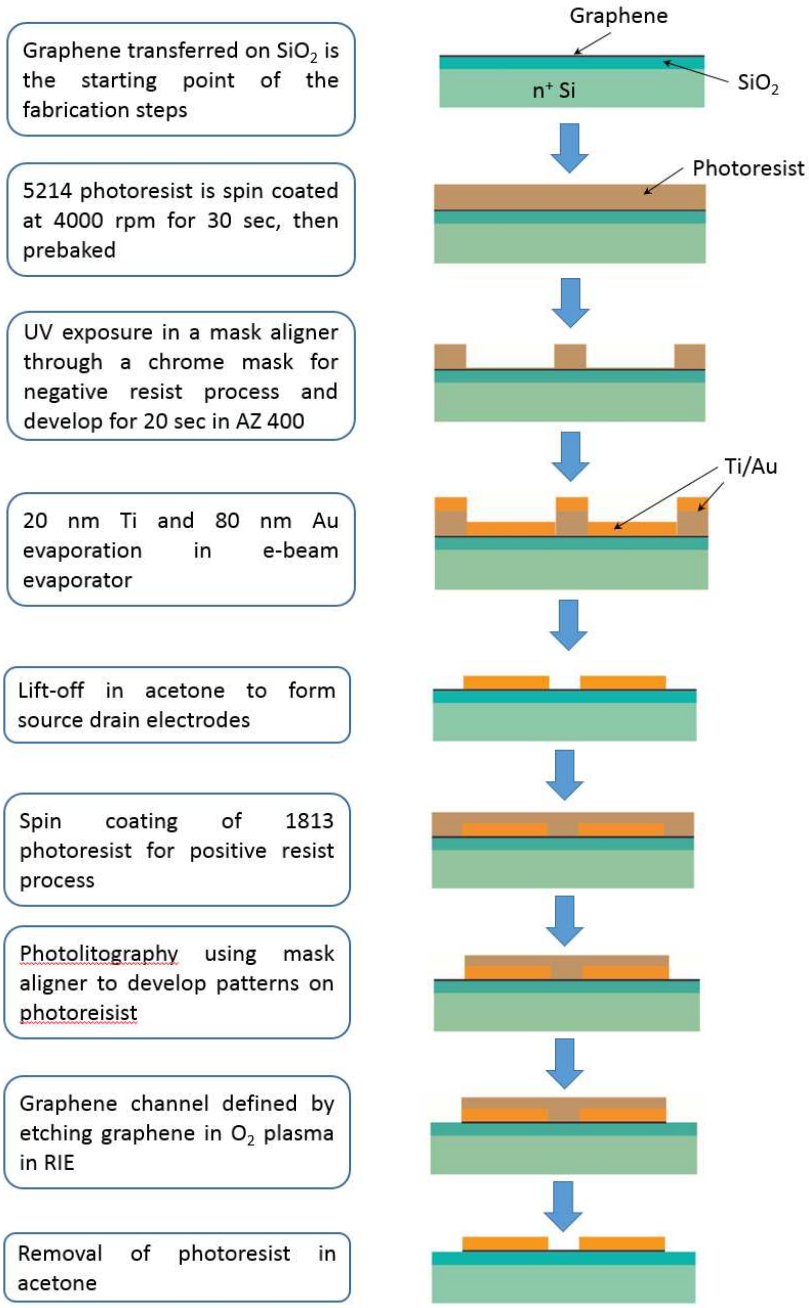

Figure 2.7 Device processing steps for fabrication of graphene FET which will serve as chem-FET.

is followed by organic cleaning of the sample in acetone and IPA.

2.4 Graphene FET and Electrical Test Pattern fabrication

The complete fabrication process flow for graphene FET fabrication on SiO_2/Si substrate is shown schematically in Figure 2.7. The highly doped Si has low resistivity in the range of 0.008–0.02 Ω-cm, serves as global back-gate and the SiO_2 with thickness of 100/300 nm acts as the gate dielectric. The graphene was transferred on top of SiO_2/Si using process described in previous section. The graphene was then spin coated with

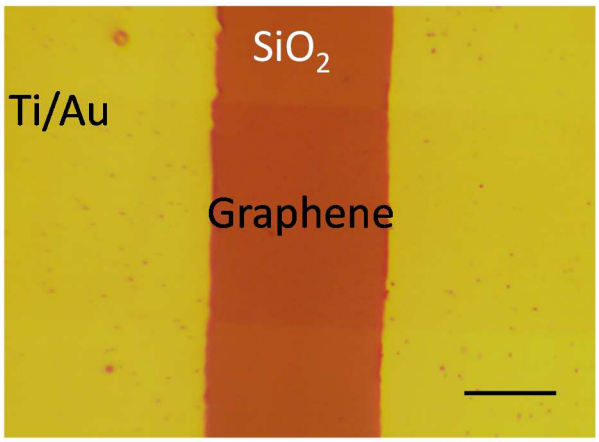

Figure 2.8 Optical micrograph of graphene FET showing 20 µm long and 30 µm wide graphene channel on top of 300 nm SiO_2 substrate. The scale bar is 10 µm.

photoresist and UV exposure was performed in mask aligner and subsequently developed in AZ400K to define pattern on resist. Oxygen plasma in RIE chamber was used to define graphene pattern. The resist was then removed in acetone. The patterned graphene was again coated with photoresist for second round of lithography to make metal contacts on graphene. The patterns for metal contacts were made using lithography as before. 20 nm of Ti or Cr, and 80 nm of Au were evaporated in e-beam evaporator at 10^{-6} Torr. The contacts were finally formed using metal lift-off in acetone. The order of the two

lithography processes are interchangeable. As fabricated device optical image is shown in Figure 2.8.

2.5 Electrical Characterization of Graphene Devices

To evaluate the electrical performance of CVD graphene, we have carried out series of measurements in the form of transmission line method (TLM) patterns and field effect transistors to evaluate contact resistance, sheet resistance, mobility, impurity concentrations, current on/off ratios, etc. One of the obstacles in the progress of graphene device performance is metal-graphene contact [8], which needs to be improved with the emphasis of ultralow contact resistance to exploit its unprecedented potential.

The semiconductor resistance is defined by sheet resistance R_{sh}. The interaction of semiconductor or semimetal (for example graphene) with metal contacts is characterized by contact resistance, R_c (Ω) and specific contact resistivity, ρ_c (Ω-cm^2). TLM pads are

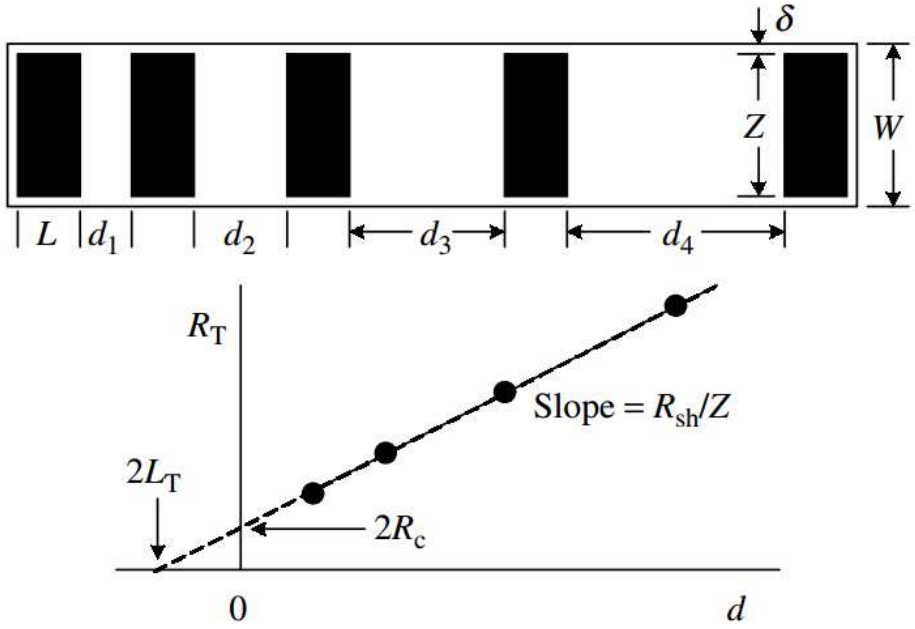

Figure 2.9 Schematic of TLM pads with various geometrical parameters. A plot of total resistance across two pads from IV measurements as a function of pad spacing d shows how to extract sheet and contact resistance [9].

very simple test structure that lets us measure these parameters for metal semiconductor contacts as shown in Figure 2.9. The relationship between these parameters with the total measured resistance as a function of pad spacing (d) is given by equation 2.1. [9] The specific contact resistance, ρ_c, is independent of contact area, therefore becomes important term for comparing ohmic contacts of different materials and processes. The transfer length (L_T) can be considered as the distance over which most of the current transfer from material to metal contact or vice versa. It can be defined as the distance over which the voltage drops to 1/e times and from the extracted values of transfer length and sheet resistance, specific contact resistivity (ρ_c) can be determined with the relationship equation 2.2.

$$R_{Total} = 2R_C + L\frac{\rho_s}{d} \qquad (2.1)$$

$$\rho_C = \rho_s L_T^2 \qquad (2.2)$$

To examine these parameters for graphene, 200 µm × 200 µm wide 20nm Ti/80 nm Au pads with varying separation. Fabricated TLM patterns are shown in Figure 2.10 (a). The current-voltage measurements were performed using a Keithly 2612A System Source Meter unit. Figure 2.10(b) shows TLM characterization on device fabricated on graphene sample which didn't go through any extra processing in between transfer and fabrication steps shown in Figures 2.6 and 2.7. The extracted sheet resistance, R_{sh} is 834.1Ω/□. The L_T was ~3 µm and R_c was 26.6 Ω. The specific contact resistivity, ρ_c obtained from R_{sh} and L_T using Equation 3.1 is 2.75×10^{-4} Ωcm^2. This value of ρ_c is on high side but matches well with reported values of contacts on graphene.

There is a possibility of moistures, PMMA residues and other impurities trapped at the time of graphene transfer may cause ρ_c to become large. To investigate further,

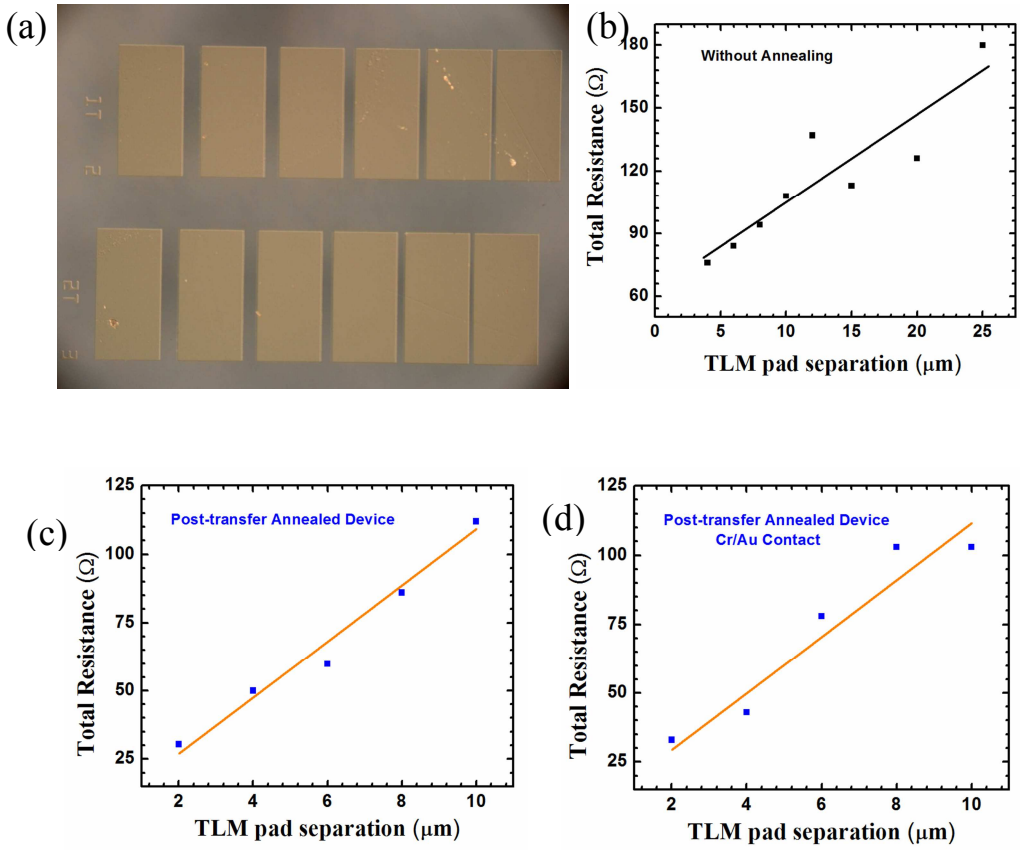

Figure 2.10 (a) Optical Image of TLM test patterns with pad dimensions of 200 μm × 200 μm. TLM characterization experimental data points (black) and linear fitted line for Ti/Au contacts (b) without post-transfer annealing, and (c) with annealing in forming gas after graphene transfer on SiO_2 substrate. (d) Cr/Au contact with post transfer annealing.

additional step has been introduced in the fabrication process. This time the samples were annealed in forming gas for 90 minutes at 400 °C. The forming gas was obtained by flowing UHP Ar and H_2 at a flow rate of 800 and 200 sccm respectively. The TLM measurements performed on one such sample is shown in Figure 2.10(c). The R_{sh} obtained on these annealed devices was 1972 Ω/□ which is more than double for the value of graphene that was not annealed. The higher sheet resistance value of graphene most likely originating from annealing process induced reduction in carrier density. The L_T was obtained as ~0.4 μm which resulted ρ_c of 2.8×10^{-6} Ωcm^2 and the R_c was found to be 3.8 Ω. These low values

of contact resistance and ρ_c are quite impressive and highlights the importance of annealing in transferred CVD graphene for device fabrication. Figure 2.10(d) is showing the TLM results for Cr/Au contact with post graphene transfer annealing and it produced similar results as before with ρ_c of 7.2×10^{-6} Ωcm^2 and R_c of 6 Ω. Thus, the improvised fabrication steps is applicable to both Ti and Cr adhesion metal layer for Au contact of CVD graphene.

The transfer characteristics of back gated graphene FET is shown in Figure 2.11(a). The I_{DS} vs. V_{bg} plot is ambipolar in nature which is a direct consequence of liner dispersion relation in graphene with zero band gap. The minimum conductivity point in transfer characteristics, also referred as Dirac point, was at V_{bg} of 12 V. The positive Dirac point reaffirms that CVD graphene transferred on SiO_2 is p-type in nature. Figure 2.11(b) shows family of I_D-V_{DS} curves with back-gate bias V_{bg} varied from -20 to 0 volt with an increment of ΔV_{bg} of 5V. At each fixed back gate bias V_{DS} varied from 0 to 5V. The decrease is current at a particular V_{DS} with increasing back gate bias also shows p-type behavior of transferred graphene in negative V_{bg} range. Another important device parameter that can

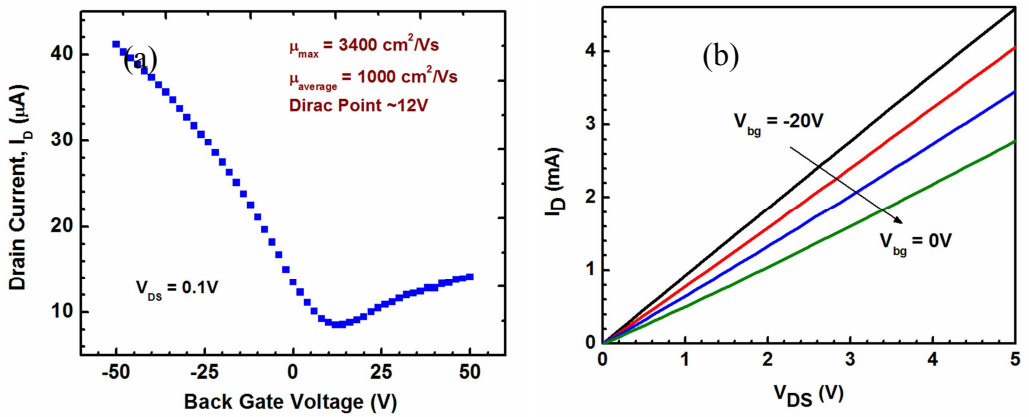

Figure 2.11 (a) Family of curves for graphene FET showing increase in I_{DS} with more negative V_{bg} indicating p-type behavior. (b) I_{DS}-V_{bg} transfer characteristics of the chem-FET with Dirac point at 12 V, indicating p-type behavior of graphene transferred on SiO_2.

be obtained from transfer characteristics of this device is field-effect mobility, μ_{FET}, given by the equation 2.3.

$$\mu_{FET} = g_m \, L/W \, C_{ox} \, V_{DS} \qquad (2.3)$$

Where g_m is transconductance $g_m = \Delta I_D / \Delta V_{bg}$, L is length of graphene channel, W is width of the graphene channel, C_{ox} is the oxide capacitance per unit area. With the improvement in graphene growth quality and fabrication process, obtained average and maximum mobility values are ~1000 and 3424 cm^2/Vs, respectively.

CHAPTER 3

ENHANCED GRAPHENE ELECTRICAL TRANSPORT PROPERTIES ON PLD GROWN BN ON SILICON DIOXIDE/SILICON SUBSTRATE

3.1 Introduction

Graphene has been subjected to extensive research effort due to its outstanding electrical, optical and mechanical characteristics such as atomically thin structure, high mechanical strength, high mechanical flexibility, high thermal conductivity, optical transparency, superior intrinsic carrier velocity and mobility, electrical and chemically tunable work function, and possibility of heterostructure with other 3D/2D/1D materials, etc. With unique combination of all these characteristics, graphene appeared as one the possible alternatives to surpass the obstacles faced by the conventional semiconductors [1].

The 2-D nature of graphene means that injected charge carriers are confined to a surface just one atom thick (~0.34 nm). In principal, this alone may allow graphene-based devices to push the limits of device scaling beyond those of silicon and other conventional semiconductors by enabling improved gate control and, opening up the possibility of new device paradigm such as low power and high speed, vertical and in-plane Schottky devices and tunneling transistors by forming multilayer heterostructures with other lower dimensional semiconductors. However, the extreme confinement means that charge carriers are also directly exposed to the surrounding environment, making transport

through graphene highly sensitive to scattering from extrinsic impurities. This sensitivity has presented a serious engineering challenge in realizing high-performance devices that take full advantage of graphene's intrinsic qualities [2].

Graphene has no native oxide layer and has a chemically inert surface with no dangling bonds, making it difficult to integrate dielectric passivation without chemically altering the graphene surface and degrading the transport properties of the graphene channel. The fundamental challenge in the development of graphene field-effect transistors (GFET) has been engineering a dielectric that provides optimal capacitive coupling to the gate, while also minimizing degradation of device performance [2]. To meet these challenges, hexagonal boron nitride (hBN) has emerged as an exceptional dielectric for GFET application. hBN is a wide bandgap material (5.97 eV) [3], sharing the same layered-hexagonal crystal structure as graphite but with boron and nitrogen atoms occupying the A and B sublattices in the Bernal structure. The strong in-plane bonding of the hexagonal structure (with only 1.7% lattice mismatch to graphene [4]) makes the surface free of dangling bonds and, thus, chemically inert, presenting a nearly ideal dielectric interface to

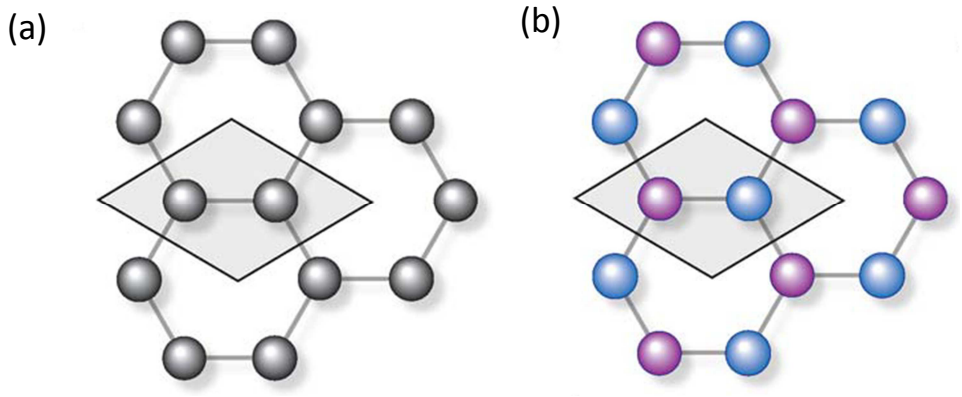

Figure 3.1 Crystal lattice structures of (a) graphene and (b) hexagonal Boron Nitride have the similar hexagonal ring where carbon atoms, and boron and nitrogen atoms form the unit cell, respectively, shown by the rectangle [2].

graphene. The crystal lattice structure of graphene and hBN is shown in Fig. 3.1 (a) and (b), respectively [2]. Following the assumption, devices fabricated on exfoliated hBN substrate exhibited an order of magnitude improvement in device mobility, reduced carrier inhomogeneity, lower extrinsic doping, reduced chemical reactivity, and improved high-bias performance in comparison to devices fabricated with conventional oxide dielectrics [2]. The dielectric properties of hBN ($\varepsilon \sim 4$ and $V_{Breakdown} \sim 0.7$ V/nm) compare favorably with SiO_2 [5, 6], and the excellent thermal conductivity of hBN [7], 600-times higher than silicon dioxide, and high surface optical (SO) phonon modes, is advantageous for FET applications to improve heat dissipation as well as reducing the SO Phonon scattering. [2, 8]

In addition to the improvement of electronic quality of graphene-based devices on hBN, graphene's electronic spectrum also becomes modified, acquiring a complex, energy-dependent form caused by difference between the graphene and substrate crystal lattices [9-11]. In particular, for graphene placed on hBN, the difference between their lattice constants and crystallographic misalignment generate a hexagonal periodic structure known as a moiré pattern [9-13]. The resulting periodic perturbation, usually referred to as a superlattice, acts on graphene's charge carriers and leads to multiple minibands [14] and the generation of spectra with secondary Dirac points. The properties of secondary Dirac fermions in graphene can be affected by a periodic sublattice symmetry breaking and modulation of electron hopping amplitudes, in addition to a simple potential modulation [15]. The possibility of creating gaps at specifically chosen energies by controllably rotating graphene or other two dimensional crystals can be used to design novel electronic and optoelectronic devices.

In general, the methods for synthesizing hBN require either high growth or high annealing temperature (~1000 °C) [16-18]. Pulsed laser deposition (PLD) offers an attractive alternative to overcome the high temperature requirement by increasing the excitations of deposited atoms and extending resonance time of the energetic species presence at the condensation surface. This facilitates low temperature growth of amorphous BN (a-BN) [19] which can then be phase transformed to polycrystalline hBN by low temperature annealing [20]. Here, we are reporting the electrical characterization of chemical vapor deposition (CVD) graphene on 5, 20 and 30 nm BN grown on SiO_2/Si substrate initially by PLD at 200 °C, and annealing at 400 °C for transformation to polycrystalline hBN. As synthesized BN improved the electrical properties of graphene by significantly enhancing mobility, reducing carrier inhomogeneity and lowering extrinsic doping compared to graphene transferred on SiO_2/Si substrate.

3.2 Synthesis of Boron Nitride by Pulsed Laser Deposited

Current methods for synthesizing h-BN nano-sheets include mechanical and chemical exfoliation [8, 21-23], high temperature chemical vapor deposition [16-18], and PVD techniques including reactive sputtering followed by high temperature annealing [24] and pulsed laser deposition of boron nitride nano-sheets [25]. Mechanically exfoliated h-BN flakes have been used for proof of concept demonstration of numerous configurations incorporating graphene and other two dimensional materials, but the device size is limited to the size of the flake and the exfoliation thickness is not well predictable, which hinders scale-up for device fabrication. Most of the CVD routes for h-BN growth include the use of metal substrates or catalysts and high growth temperature. Only recently, a direct growth of polycrystalline few-layer h-BN on sapphire and silicon substrates using CVD techniques

was successfully demonstrated with a deposition of polyborazylene film at moderate temperatures and subsequent conversion to h-BN by annealing at 1000 °C [24]. This also includes recent reports on the direct CVD growth of h-BN on the surface of epitaxial graphene with an ammonia borane precursor in a vertical tube furnace at 1075 °C [26].

From the literature survey, one major challenge for large area, 2D h-BN material synthesis is the reduction of the growth or annealing temperatures. Pulsed laser deposition is a technique, where a high energy, focused laser beam pulse causes rapid heating on the

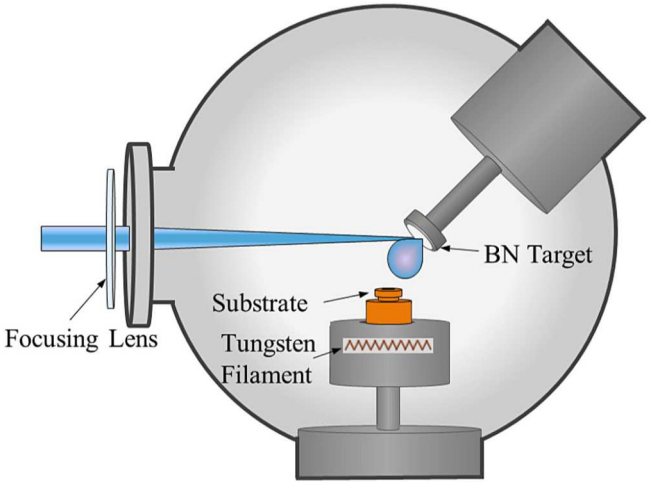

Figure 3.2 Schematic of Pulsed Laser Deposition set-up for BN deposition [19].

face of the target, causing both ionized and neutral components to accelerate from the target in the form of a plasma plume normal to the target surface. The plasma plume propagates in the direction of the substrate and can be thermalized by collisions with the background gas, depending on the pressure and target-to-surface distance. The resulting film quality and composition on the substrate can be affected by parameters including laser wavelength, power, pulse rate, pulse duration, target-to-substrate working distance and relative orientation, background gas type and pressure, and substrate temperature [19].

Few-layer boron nitride films were deposited in an ultra-high vacuum chamber with residual base pressures of 2×10^{-9} Torr [19]. Ablation from an amorphous boron nitride target (99.99% pure) was carried out using a Lambda Physik LPX300 248 nm KrF excimer laser at pulse energies of 900 mJ/pulse, 30 ns duration, and 1 Hz repetition rate. A 1000W Astex ECR power supply supplied heat to the substrate by means of joule heating a tungsten filament to a sample temperature of 200 °C, calibrated using a thermocouple spot-welded on the block just beneath the substrate. Depositions were performed in nitrogen background gas, where pressure was controlled by a butterfly valve to preset values within

Figure 3.3 Optical Image of amorphous Boron Nitride (a) 5nm (b) 10nm and (c) 20nm grown on 300 nm SiO_2/Si at 200 °C.

10^{-4} to 50 mTorr range and keeping the flow of ultra-high purity nitrogen gas (99.9999%) at 30 sccm. After deposition, the substrate was allowed to cool to room temperature before removal from the vacuum chamber. A schematic of the deposition chamber and process is shown in Fig 3.2. Optical Image is showing continuous, uniform, and smooth surface coverage of 5, 10 and 20nm BN grown on SiO_2/Si over large area in Fig 3.3(a), (b) and (c), respectively and change in color with increase in BN thickness. In case of CVD grown BN on Cu/Ni, comparably thicker layer growth has been reported along the grain boundaries [18], which has not been observed for PLD grown BN.

3.3 Boron Nitride Material Characterization

In order to assess film composition, X-ray photoelectron spectroscopic (XPS) analysis was carried out using a Kratos AXIS Ultra spectrometer with a monochromatic Al Kα x-ray source (1486.7 eV) operated at 120W(12 kV, 10 mA) and at approximately 4×10^{-9} Torr. Representative high resolution spectra of the B1s and N1s regions are shown in Fig. 3.4(a) and (b) [19]. The B 1s peak is fit with two components at 190.6 eV and 192.1 eV, corresponding to BN and BN_xO_y, respectively. The small amount of BN_xO_y observed as a

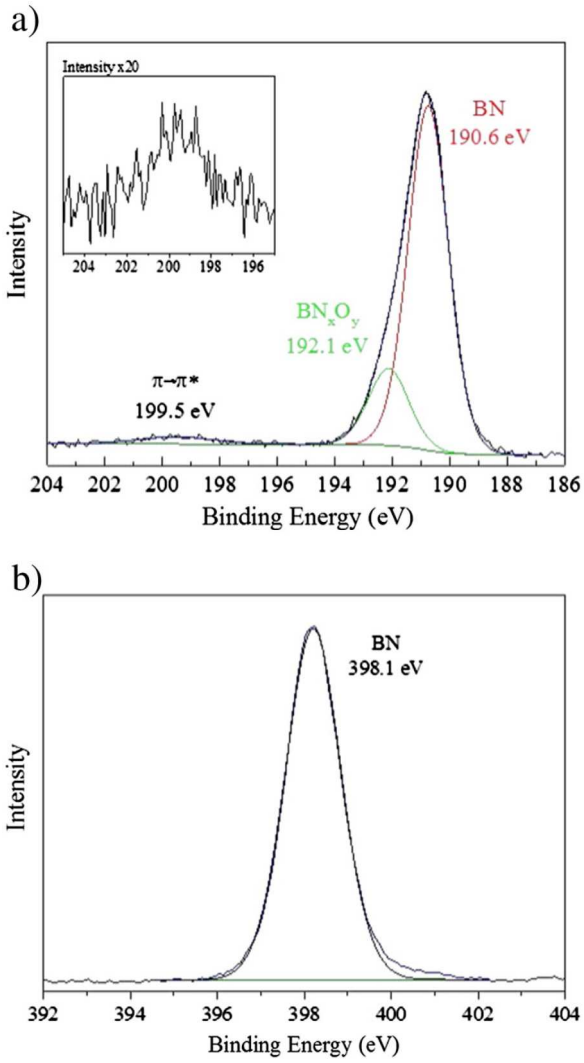

Figure 3.4 (a) Representative XPS scan of the B 1s peak as well as the π→π* satellite shifted 9 eV from the B 1s peak, and (b) a representative scan of the N 1s peak [19].

shoulder on the B 1s spectra is seen in other polycrystalline h-BN films [27], and is most likely due to exposure to ambient conditions and oxidation at the polycrystalline grain edges. The N 1s peak is fit with a single component at 398.1 eV. Next, to determine structural properties, BN samples were examined with Raman spectroscopy and AFM topography. AFM topographical images of BN on SiO_2/Si were acquired using a Bruker Dimension Icon AFM while operated in tapping mode. AFM topographical scans indicated

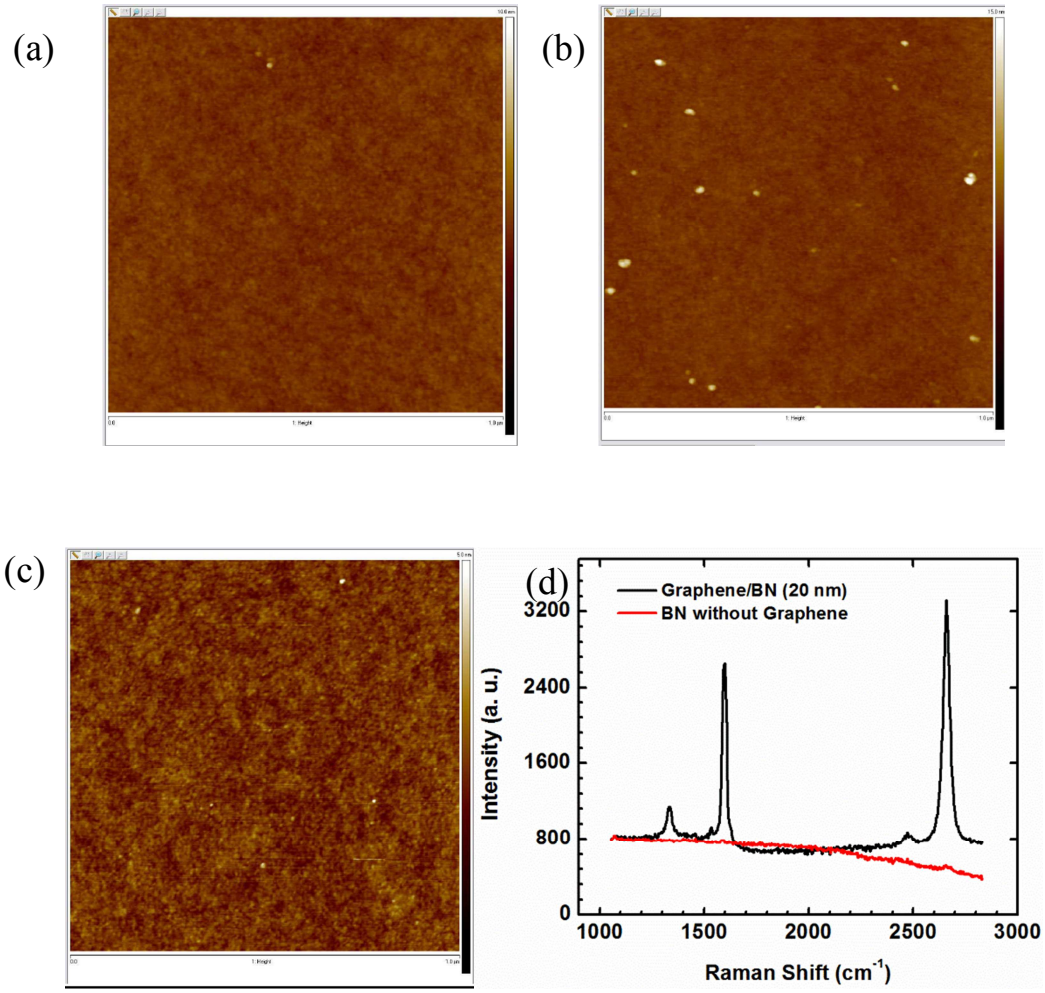

Figure 3.5 AFM topographical Image of amorphous Boron Nitride (a) 5nm (b) 10nm and (c) 20nm grown on 300 nm SiO_2/Si at 200 °C, and (d) Raman Spectra of as grown BN and graphene/BN. Without annealing there is no hBN E_{2g} peak showing the amorphous nature of as grown BN on SiO_2/Si.

large-area film coverage as shown in Fig. 3.5(a), (b) and (c) for 5, 10 and 20 nm BN on SiO_2/Si substrate. The RMS roughness of the BN did not follow any trend other than having the intrinsic roughness of the substrate underneath. Obtained roughness for three different thickness of 5, 10 and 20 nm are 0.23, 0.39 and 0.27 nm for a given area of $10 \times 10\ \mu m^2$. Raman characterization was carried out using LabRAM 1B from Horiba with a 632 nm Laser and 100x objective. Fig. 3.5(d) is showing the Raman spectra of as grown BN (red line) and transferred graphene on 20 nm BN without annealing (black line). Due to the amorphous nature of as grown BN on SiO_2/Si didn't show any Raman signature peak within 1000 - 2000 cm^{-1}.

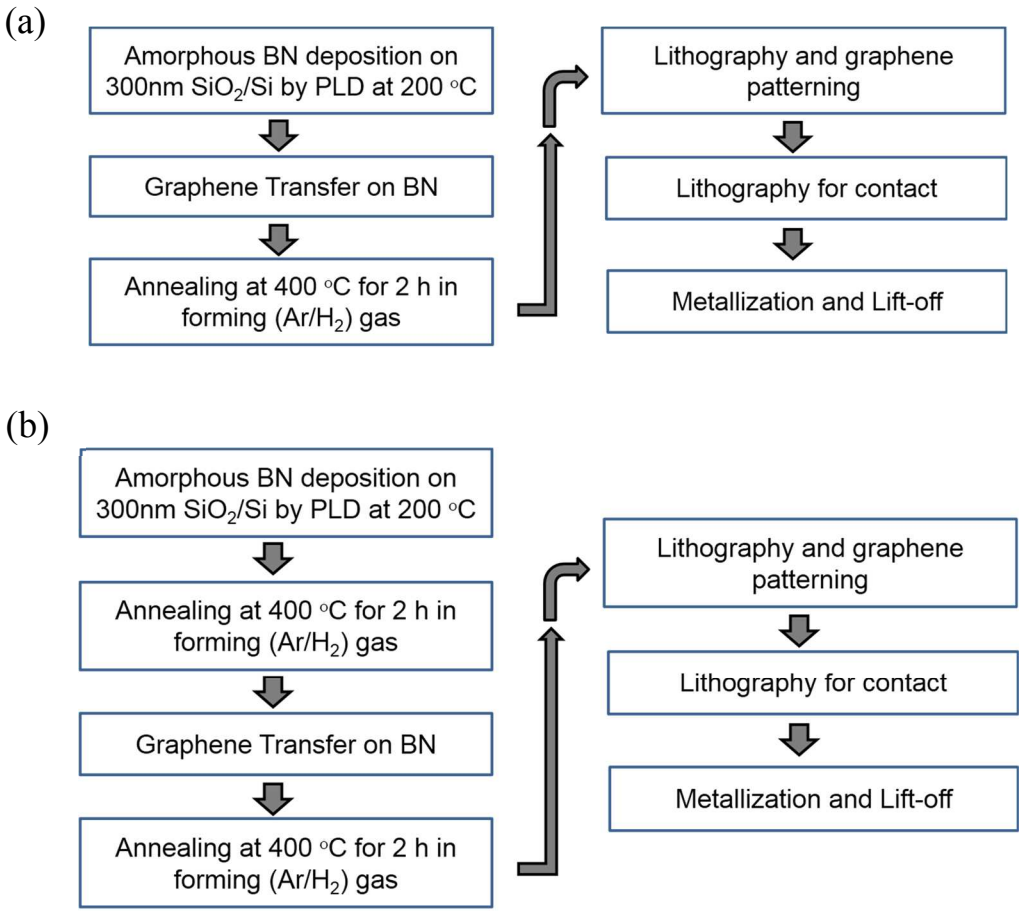

Figure 3.6 Graphene/BN Device fabrication process steps with (a) post transfer annealing and (b) annealing before and after transfer.

3.4 Graphene FET fabrication on PLD Boron Nitride

To study the electrical transport properties, we have started with 20 and 30 nm BN grown

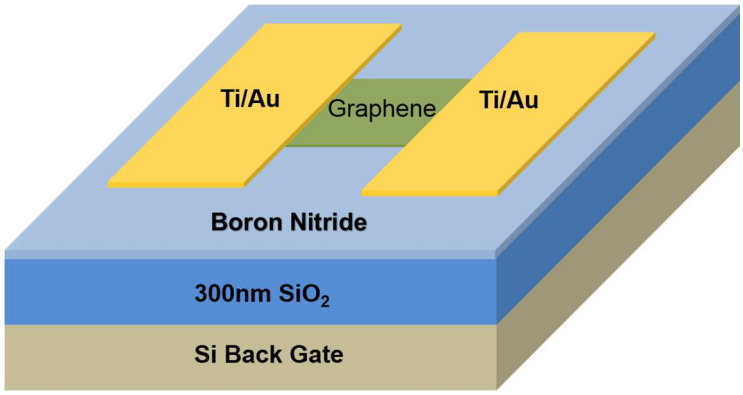

Figure 3.7 Graphene FET device schematic on BN/SiO_2/Si

on 300nm SiO_2/Si. CVD grown graphene on Cu foil was transferred on the as grown BN samples employing already mentioned PMMA assisted wet transfer method. After transfer the samples were annealed in forming gas (H_2/Ar: 200/800 sccm) for 2 hours at 400 °C and at 100 mTorr base pressure to remove the polymer residue and for better adhesion of graphene with the substrate. Adhesion of graphene with the underlying substrate is important to increase the device yield. Next, graphene is patterned by photolithography and O_2 plasma etch in RIE. Finally, Ti/Au (10/80 nm) metallization was done employing following steps: photolithography, electron beam evaporated metal deposition at a base pressure of 10^{-6} Torr and subsequent lift-off in resist remover. Highly doped Si ($\rho \sim 0.008$ Ω-cm) on the back side of the sample has been utilized as the back gate contact. Complete fabrication process flow as discussed is summarized in Fig. 3.6 (a). In addition to back gated field effect transistor (schematically shown in Fig. 3.7), transmission line method

(TLM) patterns were also fabricated on the same chip to characterize graphene contacts on BN substrate.

Annealing in forming gas has been widely used for semiconductor surface passivation. Since in our case, as grown BN is amorphous in nature, there might be surface dangling bonds compared to completely inert surface of exfoliated hBN. For surface passivation, we have carried out the forming gas annealing of as grown 5 nm BN sample also before graphene transfer. Extended process flow is shown in Fig. 3.6(b) which shows two annealing steps before and after graphene transfer. The optical image of 5 nm BN is shown in Fig. 3.8 (a) and (b) before and after annealing, is not showing any significant

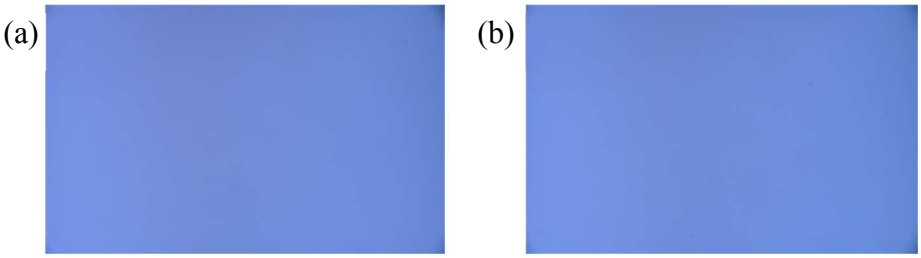

Figure 3.8 Optical Image of 5nm Boron Nitride (a) Before and (b) after annealing

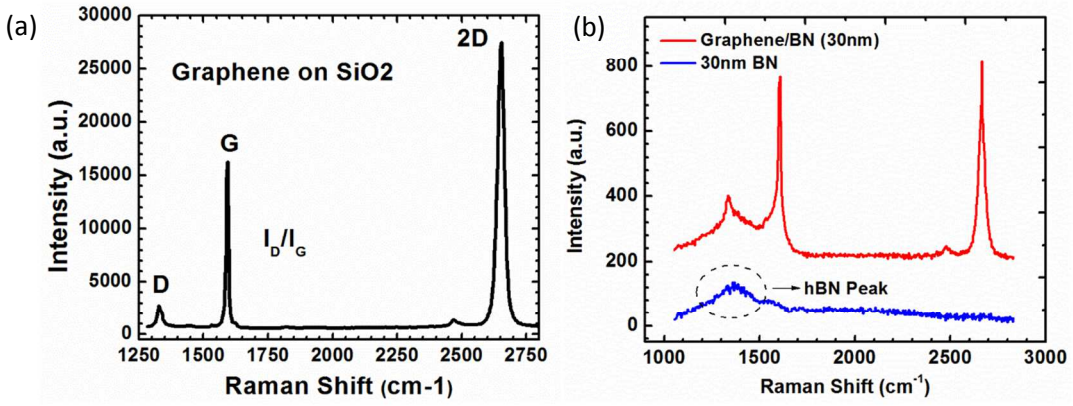

Figure 3.9 Raman spectra of graphene on (a) SiO_2/Si and (b) annealed BN/SiO_2/Si. Extracted peak at 1368 cm^{-1} from the graphene/BN showing the hexagonal nature of BN.

change. Interestingly, after annealing of the BN samples at 400 ^{O}C for 2 hour in forming gas, H_2/Ar (200/800 sccm), the Raman spectra showed [Fig 3.9 (b)] the widely reported E_{2g} shear mode peak, at ~1368 cm^{-1}, characteristics of h-BN. To compare the Raman spectra on SiO_2/Si and annealed BN/SiO_2/Si substrate, both of them are shown in Fig. 3.9 (a) and (b), where graphene on BN is exhibiting partial overlap between graphene D and BN E_{2g} shear mode peak. Similar spectra has been observed by Osama et al. [28] for layer by layer transferred CVD graphene/BN. The slight blue shift from 1365 cm^{-1} has been observed for both exfoliated and CVD grown samples [29,30]. It has been recently reported that in-situ transmission electron microscope (TEM) annealing of amorphous BN for 30 minutes at 600 ^{O}C transforms it into crystallites with average domain size of 100 nm [20]. Hence, this study also supports our claim of transforming a-BN to hBN at low temperature annealing. Thus, low temperature PLD grown a-BN and its transformation to polycrystalline hBN opens up the possibility of synthesis of large area 2D materials at much lower temperature on any desired substrate. Comprehensive Raman study of transferred CVD graphene on the annealed BN of different thickness is currently underway to better understand the interaction and possible charge transfer mechanism between the layers. The effect of annealing of BN on graphene electrical transport properties is analyzed extensively in results section later.

3.5 Graphene on BN Electrical Characterization

Due to the extreme confinement of charge carriers in 2D atomically thin graphene, it easily gets effected by the surroundings. Hence, as every other substrate, BN has its own effect on graphene and its electrical transport properties. To study the effect of graphene TLM pattern with Ti/Au contact has been fabricated and characterized on BN/SiO_2 substrate.

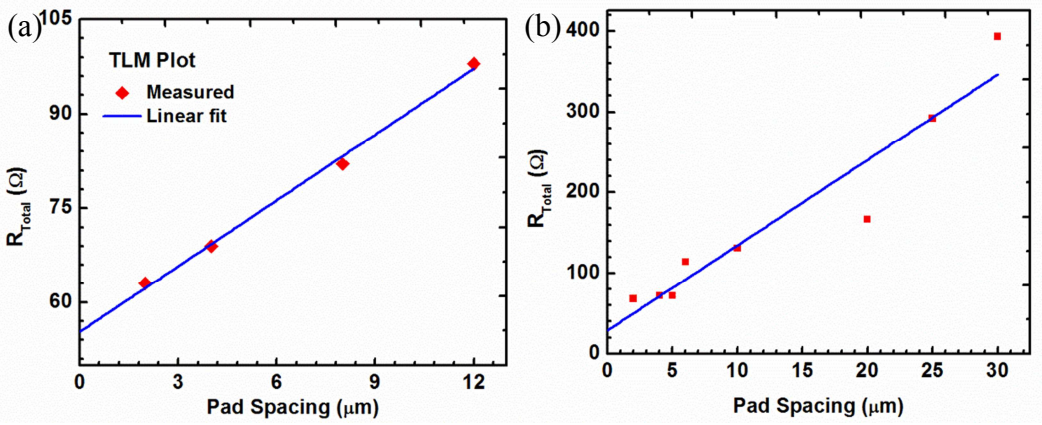

Figure 3.10 TLM Characterization plot of Graphene on (a) 30 nm BN and (b) 5 nm BN.

The voltage was swept from -1 to 1 V at ambient condition and resistance has been extracted from the measured current value. Best fit to the as measured resistance values for different contact pad spacing is shown in Fig. 3.10 for two different thickness. Extracted specific contact resistivity and sheet resistance values from the plot of Fig. 3.10 (a) are 3.9×10^{-4} Ω-cm^{-2} and 628 Ω/square, respectively for 30 nm BN which subjected to only post-graphene transfer annealing. Although the specific contact resistivity is slightly higher [31], the sheet resistance is low compared to that on SiO_2 substrate [32]. The low sheet resistance is probably due to charge transfer between graphene and BN, which transformed from amorphous BN to polycrystalline h-BN after annealing.

For 5 nm BN sample which has been annealed before and after graphene transfer, shown in Fig. 3.10 (b), the specific contact resistivity and sheet resistance values are 3.5×10^{-5} Ω-cm^{-2} and 1903 Ω/square, respectively. Annealing twice has improved the graphene contact, but increased the channel resistance which is most likely from the reduction in intrinsic carrier concentration. Specific contact resistivity showed an improvement of one order over 30nm BN and better than that of SiO_2/Si substrate for the similar fabrication

process steps [31]. The characteristic resistance values are close to that of reported in the literature for CVD and epitaxially grown graphene. The extant of charge transfer between graphene and h-BN, and its effect on graphene electronic spectrum is under further investigation.

For comparison purpose, using graphene from the same copper piece, FET has been fabricated on 300 nm SiO_2/Si substrate cleaved from the same wafer. Representative back gated transfer characteristics is shown in Fig. 3.11 (a) where within 40.0 V back gate bias range the Dirac point was not observed and no sign of current minima is visible. From the transfer characteristics extracted maximum mobility is 1410 cm^2/Vs, which is typical as

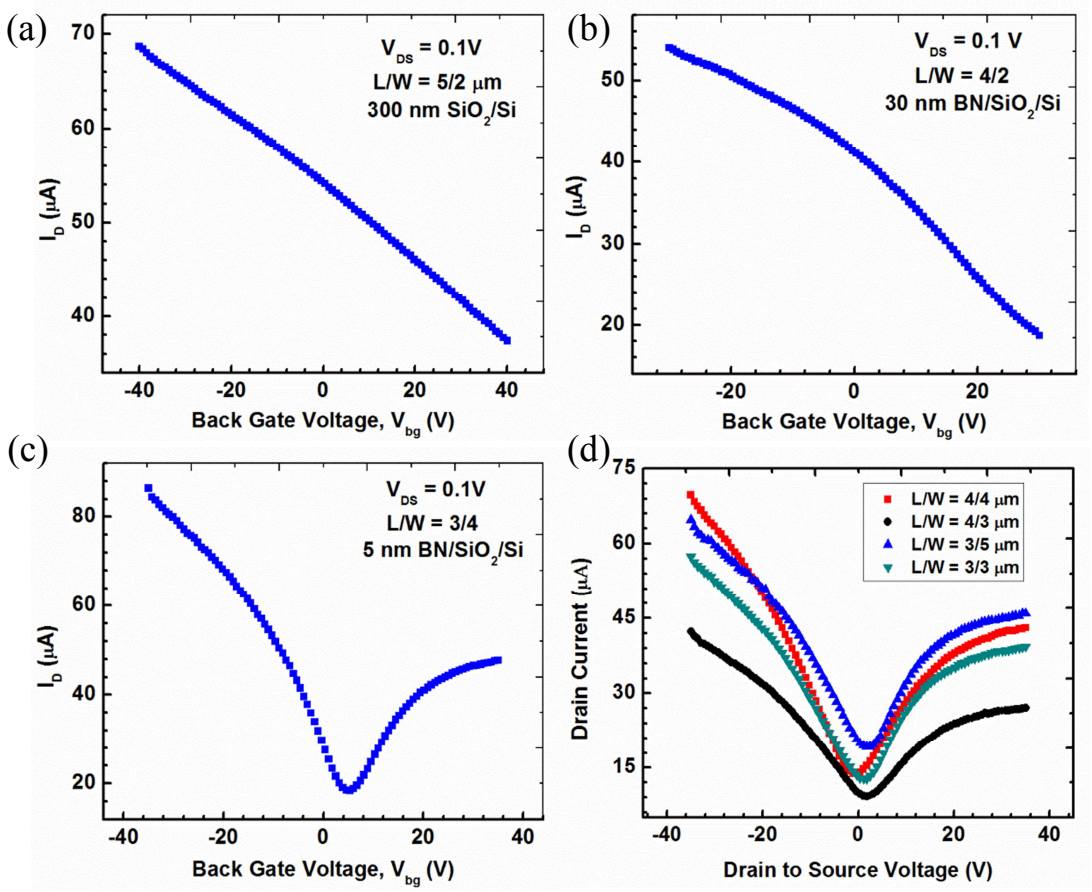

Figure 3.11 Transfer characteristics of graphene from same Cu piece on (a) SiO_2/Si, (b) 30 nm BN/SiO_2/Si, (c) 5 nm BN/SiO_2/Si substrate and several devices with different dimensions on (d) 5 nm BN/SiO_2/Si substrate.

obtained for graphene devices on SiO_2/Si substrate. Representative transfer characteristics of back gated graphene transistor on 30nm BN/SiO_2/Si is shown on Fig. 3.11 (b). Mobility of 2810 cm^2/Vs was extracted for this device, which is reasonably improved compared to only SiO_2/Si substrate. However, graphene residual/impurity carrier concentration is not very low since charge neutrality point/Dirac point has not been observed within back gate bias range of 30V. It can be concluded from the transfer characteristics that, the drain to source current shows distinct slope reduction near 30 V, which indicates p-type doping in graphene in this device. However, from Fig. 3.11 (a), monotonic drain to source current decrease with back gate voltage on SiO_2/Si indicates Dirac point is further away compared to the device on 30 nm BN/SiO_2/Si substrate and hence higher residual or impurity carrier concentration of graphene on SiO_2/Si. Similar characteristics has been observed for more than 40 devices for both 20 and 30nm BN/SiO_2/Si. In addition to the lower impurity carrier concentration in graphene devices on BN/SiO_2/Si substrate, more than 2 times increase in mobility has been observed on 30nm BN substrate compared to SiO_2/Si.

Next, 5 nm of as grown BN was chosen to evaluate its performance as ultrathin substrate due to its promise as ultimately scaled dielectric and tunneling barrier for 2D material based multilayer structure for electronic, photonic and sensing applications. It has been reported in literature that five layers of hBN can effectively screen graphene carriers from dangling bonds associated with the oxide and can provide an atomically smooth surface (roughness < 100 pm). [4] Furthermore, a stack of five layers of BN has been shown to provide sufficient insulation from oxide charge traps (>1 GΩ) [33] as well as excellent thermal conductivity ~ 200 W/mK [7] much higher than SiO_2. Recently, hole mobility of

10000 cm^2/Vs at ultrahigh vacuum (10^{-6} Torr) from layer transferred graphene on five layer BN both grown by CVD on copper has been reported [34].

Afterwards, we have carried out back gated electrical measurements of graphene FET on 5 nm BN where several significant improvements have been observed. One of the important findings is that, the Dirac point of these devices moved really close to zero gate bias even in ambient as seen in Fig 3.11 (c). This is in complete agreement with the reported results of small impurity carrier concentrations in graphene on hBN substrate. Fig 3.11 (d) is showing several other devices with Dirac point in the range of ±1.0 V with reasonable

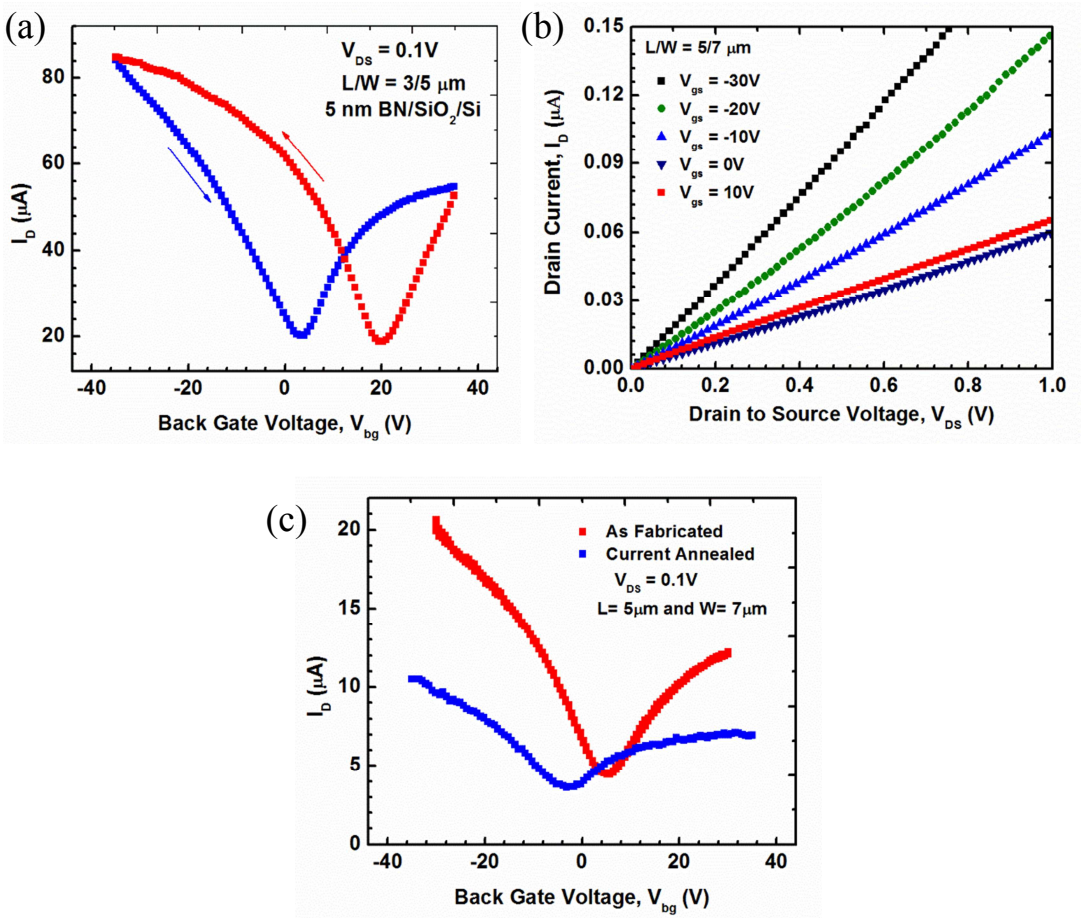

Figure 3.12 (a) Hysteresis in transfer characteristics of graphene FET on 5 nm $BN/SiO_2/Si$, (b) I_D - V_{DS} family of plots at different back gate bias, and (c) effect of current annealing on transfer characteristics of the same device

current on/off ratio. Current minima around zero voltage demonstrates the promise of low temperature grown PLD BN as a substrate and dielectric for graphene and other 2D material based electronics and sensing applications.

Although transfer characteristics in Fig 3.11 (c) of representative device on 5 nm BN is showing the Dirac point close to 0.0V in ambient condition, its current on/off ratio is low which is originating from the defect and imperfections of the BN. Additionally, reverse sweep of the back gate bias showed Dirac point difference of 16.5 V between forward and reverse sweep which is visible in Fig 3.12 (a). The hysteresis indicates the presence of slow trapped charge in BN or at the interfaces between SiO_2 and BN, and/or BN and graphene. It could be reduced by either one or all of the following approaches: phase transforming the hBN nano-crystallites to polycrystalline structure with as large as possible crystal domains, improving the dielectric property of BN and subsequent use of local back gate which will completely eliminate the SiO_2 from the active gate dielectric stack, engineering better interface between graphene and BN, etc. Fig 3.12 (b) shows the family of current response for source to drain voltage at five different back gate bias, where current is decreasing as the gate bias is increasing till 0.0V and trying to increase again with increasing gate bias of 10.0V, confirming the Dirac point position between 0 and 10V. After several measurements of drain current with drain to source voltage as a function of different back gate bias, transfer characteristics was measured again. Both the transfer characteristics plotted in Fig 3.12 (c) where the Dirac point shifted to -3V from +5V although current decreased almost half the initial value. Dirac point shift to negative voltage is due to removal of PMMA residue and other surface impurities by effective current annealing at the time of repetitive measurements. On the other hand current

decrease has also been observed previously by other group [35] which is most likely from the oxidation of graphene in air due to joule heating since the measurements were carried out in air. In this case, the current annealing induced cleaning of graphene and oxidation in air due to joule heating were competing processes at the time of measurements.

Next, hole mobility on 5nm BN has been extracted utilizing the method previously used. Highest hole mobility on 5nm BN/SiO_2/Si substrate is 4976 cm^2/Vs compared to only 1417 cm^2/Vs on SiO_2/Si substrate, which is more than 3.5 times increase. Similarly, average hole mobility on 5nm BN/SiO_2/Si substrate is 1955 cm^2/Vs which is more than

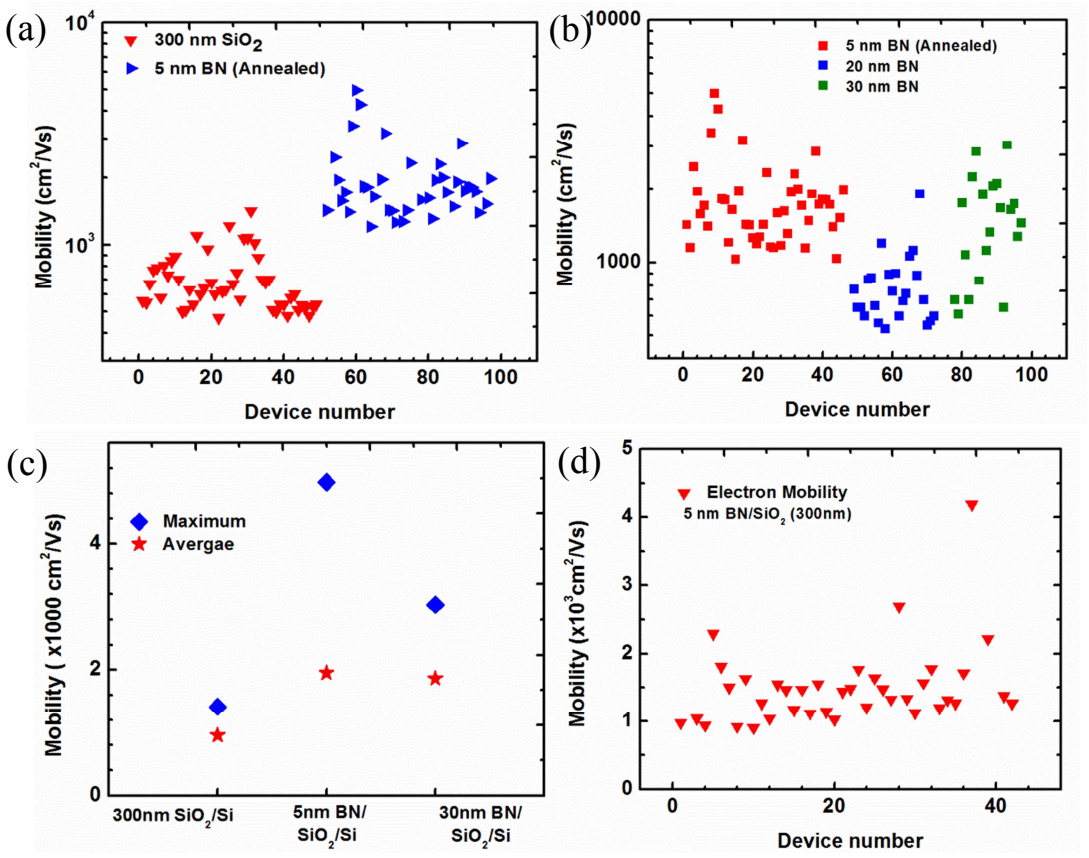

Figure 3.13 Graphene field effect hole mobility (a) comparison on 5 nm BN/SiO_2/Si and 300 nm SiO_2/Si substrate, (b) variation for different BN thickness and annealing twice (c) comparison of average and maximum hole mobility, and (d) Electron Mobility on 5 nm BN/SiO_2/Si substrate.

two times higher than SiO_2/Si substrate in air and ambient condition. Comparison of hole mobility between 300nm SiO_2/Si and 5nm BN/SiO_2/Si substrate for more than forty devices is shown in Fig 3.13 (a). In Fig 3.13 (b) we compared hole mobility for 5, 20 and 30 nm BN where although devices on 20 nm BN substrate showed lower mobility compared to 5 and 30nm, still better than SiO_2/Si substrate [Fig 3.13 (b)]. Possible reason for low mobility on 20 nm BN compared to other 2 thickness is probably originating form variation in process especially at the time of fabrication. The maximum mobility on 20 nm (1910 cm^2/Vs) is higher than SiO_2/Si (1417 cm^2/Vs) while both maximum (3035 cm^2/Vs) and average (1865 cm^2/Vs) mobility on 30nm BN substrate showed more than two times improvement. Among 5 and 30 nm BN, 5 nm showed higher maximum mobility of 4976 cm^2/Vs over 30 nm BN of 3035 cm^2/Vs, although average mobility for 5 nm (1955 cm^2/Vs) is slightly higher than 30 nm BN (1865). Maximum and average mobility for SiO_2/Si, 5 and 30 nm BN is shown in Fig 3.13(c), where both 5 and 30nm BN showed significant improvement over SiO_2/Si substrate. In terms of μ_{max}, for 5 and 30 nm BN improvement is almost 3x and 2x, respectively, while 2 times for both of them in case of $\mu_{average}$. Since the current minima on 5 nm BN sample is at or close to 0.0V, the electron mobility can also be extracted easily. Extracted electron mobility is shown in Fig 3.14(d), where maximum and average electron mobility is 4194 cm^2/Vs and 1555 cm^2/Vs, respectively. The average electron mobility on 5 nm BN is higher than that on SiO_2/Si substrate as discussed in chapter 2.

Dirac point of forty devices on 5nm BN substrate is plotted in the bar chart format in Fig 3.14 (a), where one device showed -0.35 V and all other ranging from 0.0 to 5.75 V with an average of 3.5 V. Fig 3.14 (b) shows the distribution of zero back gate bias or

residual carrier concentration which determines the effect of substrate such as imperfections, water droplets, effect of traps and interface effects, residue from fabrication steps, dielectric environment both bottom and top, doping induced by surroundings including moisture in air, etc. on graphene channel. Minimum residual carrier

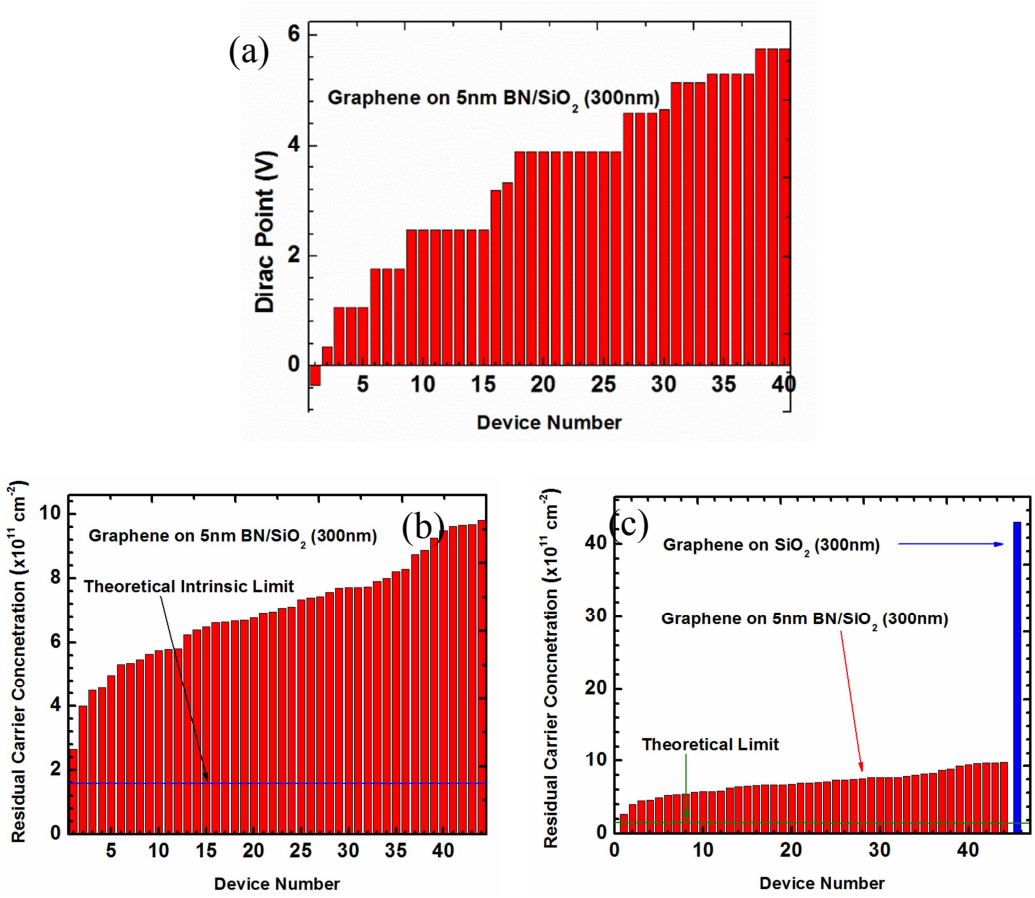

Figure 3.14 (a) Dirac point and (b) residual carrier concentration distribution of graphene on 5 nm $BN/SiO_2/Si$ substrate and (d) comparison with SiO_2/Si substrate.

concentration achieved on 5 nm BN is 2.64×10^{11} cm^{-2} and average over forty devices is 7.0×10^{11} cm^{-2}. Theoretical intrinsic limit of residual carrier concentration for graphene is 1.6×10^{11} cm^{-2} [36] as shown by the blue horizontal line, which is close to the minimum achieved for 5 nm BN/SiO2/Si substrate, 2.64×10^{11} cm^{-2}. Finally, Fig 3.14 (c) shows the

comparison between BN and SiO_2 substrate, p_o is 4.3×10^{12} cm^{-2} for SiO_2 which is more than 6 times higher compared to the achieved average for 5 nm BN.

From the presented results, the significant findings for graphene devices on BN in ambient condition are: both average and maximum mobility increased, average Dirac point is 3.5 V and low residual carrier concentration which is close to theoretical intrinsic limit. These improvements are mutually related in several aspects. Most of the graphene devices are fabricated on SiO_2/Si substrate which show substantial p-type doping in graphene, larger hysteresis (Dirac point difference between forward and reverse sweep) and low mobility. The major source of impurities in graphene are three types: from the SiO_2 surface itself, adsorbed molecules on its surface, and PMMA/resist residues from device fabrication. Since the effect of substrate is more relevant to this research, subsequent discussion is focused on the first two processes.

Due to its polar nature, SiO_2 surface has dangling bonds where various adsorbates can attach themselves ranging from water molecules to PMMA residue. One such example is the coupling of Hydroxyl groups (-OH) to the dangling bonds of the Si and formation of silanol (SiOH) groups which is hydrophilic [37-39]. This hydrophilic nature can attract polar molecules to bond with silanol and participates in charge transfer with graphene leads to unwanted extrinsic doping. Following this mechanism adsorbed water molecules is believed to be the major source of p-type doping in graphene [37, 40-42]. This increase in carrier concentration and accompanying charged impurities result in enhanced coulomb scattering. Due to its polar nature, SiO_2 surface optical phonon induced scattering is another major scattering mechanism in graphene [43].

Introduction of BN in between graphene and SiO_2 reduces the mentioned effects substantially, although BN growth itself is in the very early stage of exploration. Even considering this, from the significant improvement in graphene electrical characteristics, it can be concluded that, the inert, hexagonal and lattice matched structure of BN considerably reduces extrinsic doping and carrier inhomogeneity in graphene. This results in both reduction in residual carrier concentration and Dirac point which is expected to reduce the coulomb scattering. In addition, BN has high optical phonon frequency close to that of graphene which helps in reducing the Optical phonon scattering. Essentially with BN as a substrate, both coulomb and phonon scattering is reduced which significantly enhances the carrier mobility.

CHAPTER 4

FUNCTIONALIZED GRAPHENE/SILICON CHEMI-DIODE H_2 SENSOR WITH TUNABLE SENSITIVITY

4.1. Introduction

Due to its two-dimensional (2D) nature that makes it essentially a surface, and very high carrier mobility [1-6], graphene is especially suited for sensing applications [3-10]. Although it has excellent sensitivity to a large variety of polar molecules, (i.e. NO_2 and NH_3) it is insensitive to most non-polar molecules, such as H_2, with which it does not exchange charge. A surface functionalization is therefore necessary for detecting these non-polar molecules. It has been demonstrated that surface functionalization of graphene by catalytically active noble metals (such as Pd and Pt) leads to charge transfer between graphene and the metal hydride formed in presence of H_2 facilitating its detection [11–13]. There are reports on H_2 sensors utilizing epitaxial graphene [12], graphene synthesized through chemical vapor deposition (CVD) [11], and chemically synthesized graphene nanoribbon networks [13], which are functionalized with either Pd or Pt to impart H_2 sensitivity. Of these, only the chemically synthesized graphene nanoribbon network based sensor has so far shown good H_2 sensitivity (producing ~55% change in resistance for 40 ppm H_2), while others showed much lower sensitivity in the range of few percent for tens

of ppm H_2 exposure. The higher sensitivity of the graphene nanoribbon networks [13]can be attributed to its porous structure and high specific surface area. In general, the sensitivity of these commonly used "chemiresistor" type sensors is dependent on two factors: (i) the amount of charge exchanged from the analytes (facilitated by the functionalization layer), and (ii) the mobility of the charge carriers, since resistivity is inversely proportional to the product of mobility and charge density. The former depends on the material properties and thickness of the functionalization layer used, while the latter is controlled by the graphene quality, and more significantly, by the charge carrier scattering caused by the functionalization layer [14, 15] and substrate underneath the graphene [16]. Although the material property of graphene can be controlled to a large extent through optimization of the synthesis process, in general, the choices are very limited in terms of the substrate and the functionalization layer used to realize the sensors. However, the effects of the last two factors are extremely significant on graphene mobility, which reduces from 200,000 cm^2/Vs for suspended graphene [2] to only a few thousand cm^2/Vs for graphene on SiO_2 or SiC substrates [16, 17]. The functionalization layer can further reduce the mobility [18], and if conducting, can also provide a parallel path for current flow thereby further reducing sensitivity. Therefore, sensing paradigms where the sensitivity of the sensor does not directly depend on the mobility of the charge carriers would be of significant interest.

Recent demonstration of graphene/Si Schottky heterojunction [19], and its usage in several devices from solar cells to "barristors" [20-22] have opened up the possibility for developing a new class of "chemi-diode" sensors. Due to the atomically thin and semimetalic nature of graphene, its Fermi level can be easily modulated by electrical, optical or chemical means which in-turn changes the Schottky barrier height (SBH) at the

heterointerface. This is in contrast to classical metal-semiconductor Schottky junctions, where the Fermi level of the metal remains fixed regardless of external factors. Nevertheless, this property of graphene/Si heterojunctions can be utilized to design sensors with ultra-high sensitivity, since change in SBH induced by adsorbates exchanging charge with graphene, will change the current flowing across the junction exponentially. Graphene/Si Schottky diode based sensor has been demonstrated recently in large forward bias operation, where the diode current is controlled by series resistance, hence, high sensitivity was not observed [23]. In this work, we have demonstrated for the first time, catalytically active noble metal functionalized Graphene/Si Schottky diode H_2 sensor operated in reverse bias, which takes advantage of the exponential change in current due to SBH change, and exhibits several times higher sensitivity compared to the best performance of graphene based chemiresistor type H_2 sensor functionalized similarly. In fact, the sensitivity of the sensor allows us to reach a detection limit close to the atmospheric concentration of H_2 (~0.6 ppm) [24]. The reverse bias operation also allows modulation of the Fermi level of graphene depending on the magnitude of the bias, which can lead to the tuning of sensitivity of the sensor and expansion of the dynamic range. Another advantage of the reverse bias operation of the sensor is its low power requirement due to low steady state current in the range of μA flowing in reverse bias.

4.2. Fabrication and Characterization of Graphene/Si Schottky Diode

In this work, both Pd and Pt-functionalized graphene/p-Si Schottky diodes were investigated in terms of their sensing behavior toward H_2. Graphene samples were synthesized through chemical vapor deposition (CVD) on Cu (catalyst) foils (Alfa Aesar, 99.999% purity) in a quartz tube furnace. The synthesis was performed at 1035 °C and 10

Torr pressure with CH_4 as the precursor (nominal flow rate of 40 sccm) along with H_2 (nominal flow rate 50 sccm), following earlier reports [25, 26]. Graphene on copper foil was lithographically patterned and strips were defined by O_2 plasma etch. The Cu foil with graphene strips was coated with two layers of poly methyl methacrylate (PMMA), to add mechanical strength during subsequent processing, and baked for 1 min at 150 °C. Next, the graphene layer on the back side of the sample was removed by oxygen plasma etching, which was followed by Cu etching in 0.5 M ammonium persulfate solution for more than 12 hour, releasing the graphene/PMMA bi-layer [16]. SiO_2 (100 nm) on p-Si has been selectively removed by 1:5 diluted buffered HF just prior to transfer of graphene. Ti/Au was deposited selectively on top side of Si and annealed in Ar/H_2 atmosphere at 400 °C to form ohmic contacts. After rinsing in deionized water and IPA, the graphene/PMMA bi-layer was scooped and placed on the patterned SiO_2/Si substrate. It was then baked at 220 °C for 5 minutes to reflow the PMMA resulting in more uniformity and less cracking in transferred graphene. Afterwards, the sample was placed in acetone for 2 hour to remove PMMA [16, 27]. Ti (20 nm)/Au (80 nm) contacts were evaporated on graphene transferred on SiO_2/Si using shadow mask. The p-Si used in this work is lightly doped and have resistivity in the range of 1-10 Ω-cm. The device length is 200 μm and width is ~1000 μm in all the cases where ~80% of the total area is functionalized. There is an additional 200 μm Graphene on SiO_2 between the metal contact and Graphene/Si interface. Different thickness (1-3 nm) of Pd and Pt were evaporated on graphene in e-beam metal deposition chamber.

Raman spectra were measured on graphene transferred to the Si substrate to determine the quality of transferred graphene. Figure 4.1 (a), (b), and (c) show the

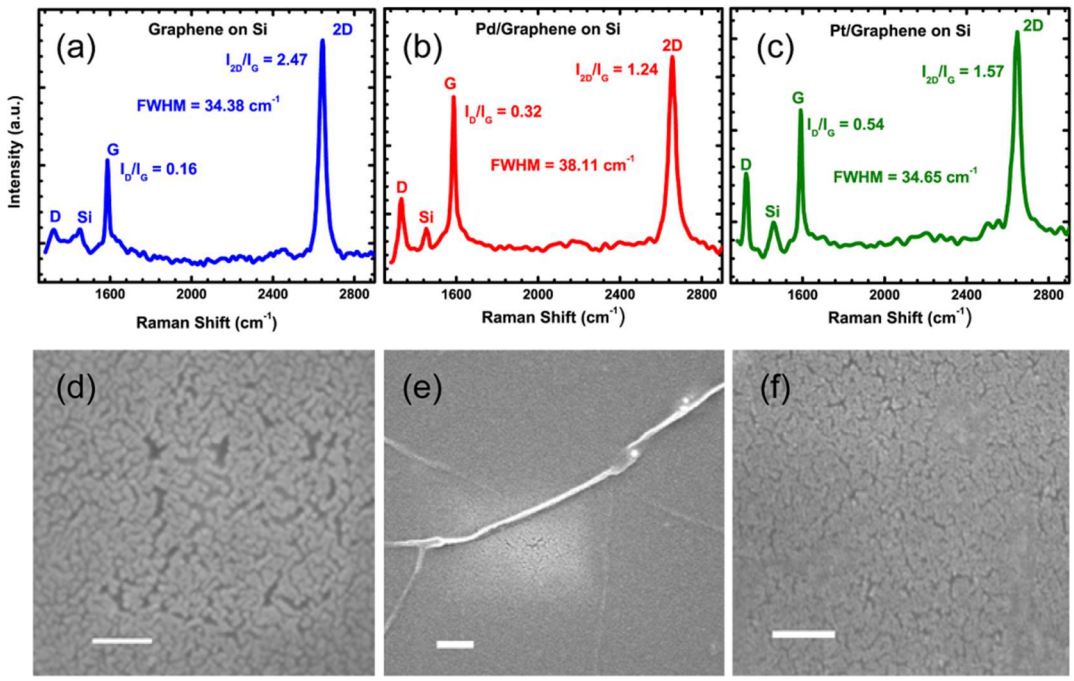

Figure 4.1 Raman spectra of (a) Graphene on p-Si, (b) Pd-deposited graphene on p-Si, (c) Pt-deposited graphene on p-Si; (d) SEM top view image of 3 nm Pd-functionalized graphene on p-Si. Scale Bar is 50 nm. (e) Zoomed out image of that shown in (d) showing graphene wrinkles. Scale Bar is 100 nm. (f) Pt-functionalized graphene on p-Si. Scale Bar is 100 nm.

representative Raman spectra of graphene transferred on Si as well as Pd and Pt decorated graphene on Si. All signature peaks, D, G and 2D, along with the Si peak at 1451 cm^{-1}, can be observed. The transferred graphene layer on top of Si [Figure 4.1(a)] shows intensity ratio, I_D/I_G ratio of 0.16, suggesting high quality graphene [28]. The I_{2D}/I_G ratio of 2.47, and 2D peak full width at half maximum of 34.38 cm^{-1}, are indicative of single layer graphene [29]. The I_D/I_G ratio of 0.32 for Pd decorated graphene [Figure 4.1(b)] suggests some degradation in the quality of graphene following electron beam evaporation of 3 nm thick Pd nanoparticles for functionalization. This degradation might be due to the creation of point defects in graphene by the metal atoms hitting it during e-beam evaporation. For 2 nm thick Pt functionalized graphene the I_D/I_G ratio is higher, 0.54 [Figure 4.1(c)], which

indicates higher defect density in the film. It is probably a consequence of higher film damage caused by heavier Pt atoms during evaporation process compared to Pd atoms. Deposited metal films typically grow on crystalline substrates through nucleation followed by grain growth. The growing grains coarsen and coalesce to form complete film coverage as metal evaporation continues. Figure 4.1(d) captures the initially formed grains of Pd on graphene/Si in a scanning electron microscopy (SEM) micrograph. Due to the small growth duration, (~2 minutes for 3 nm thickness) the Pd grains could not become large enough to coalesce completely, therefore partial coverage of Pd film is observed. A zoomed out SEM micrograph [Figure 1(e)] at the same location shows an overall smooth coverage with a few wrinkles in the graphene layer. Figure 4.1(f) shows an SEM micrograph depicting similar coverage for deposited Pt film with 2 nm thickness.

Figure 4.2(a) shows the schematic of a graphene chemiresistor sensor fabricated side by side with a graphene/Si heterojunction chemi-diode sensor with metal film functionalization layer. Optical microscopy image of the fabricated Pd-functionalized graphene/Si Schottky diode sensor is shown in Figure 4.2(b). The initial electrical characteristic of chemi-diode before Pd and Pt deposition is shown by the solid black curves in Figure 4.2(c) and Figure 4.2(d), respectively, which exhibits typical rectifying characteristic in agreement with previous reports [19-23]. A Schottky type response is expected since the work function of graphene is around 4.5 eV, which is lower than that of p-Si, with an estimated work function of ~4.97 eV (electron affinity and bandgap of Si are

4.05 and 1.12 eV, respectively [30], and from resistivity of 1 – 10 Ωcm for the p-type Si,

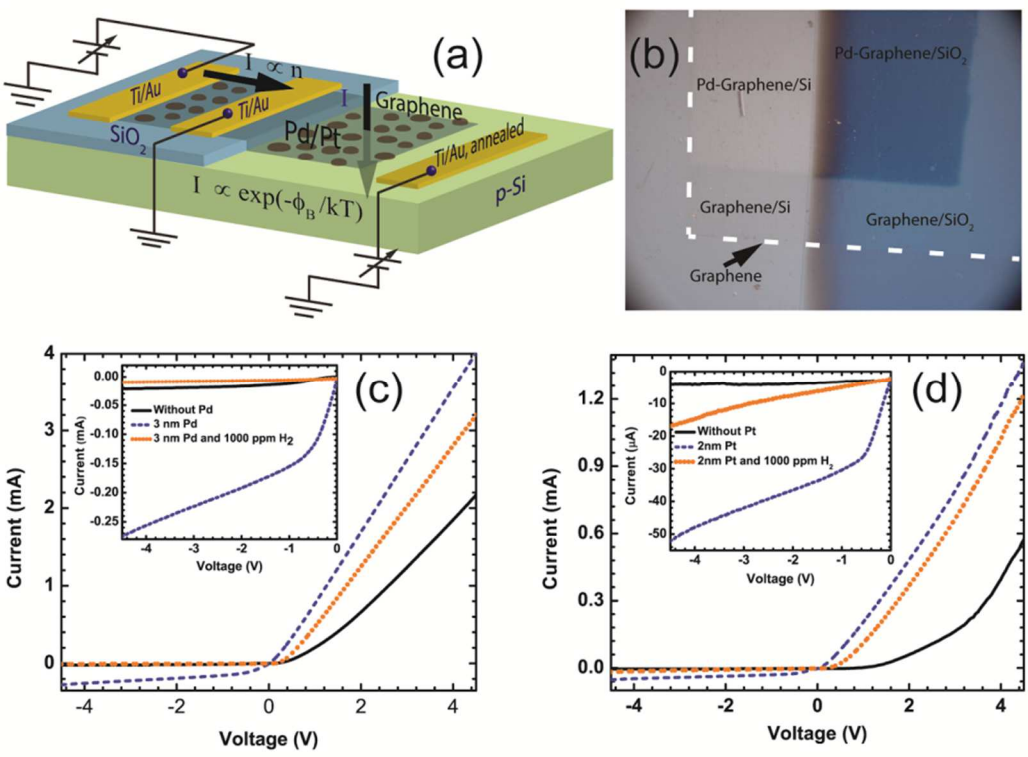

Figure 4.2 (a) Device schematic and biasing scheme of Pt/Pd functionalized graphene chemiresistor and graphene/Si Schottky diode sensors fabricated on the same chip. Gray spots indicate metal decoration. (b) Optical Image of graphene/p-Si heterojunction Schottky diode sensor with H2 nm Pd-functionalization, white dashed box approximately enclosed the graphene on both Si and SiO_2, graphene is visible on SiO_2, and Pd-functionalization is also showing contrast on SiO_2 region covered by graphene. (c) Current-Voltage (I-V) characteristics of graphene/p-Si (black solid line), after Pd-functionalization (blue dashed line), and after 10 minutes exposure of the Pd-functionalized sensor to 1000 ppm H_2 (orange dotted line). (d) I-V characteristics of graphene/p-Si (black solid line), after Pt-functionalization (blue dashed line) and after 10 minutes exposure of the Pt-functionalized sensor to 1000 ppm H_2 (orange dotted

$E_F - E_V$ is estimated to be ~ 0.2 eV). The rectifying current-voltage characteristics of

graphene/Si heterojunction can be expressed using thermionic emission model formulated by the following equation [30],

$$I = I_S\left[e^{\left(\frac{qV}{\eta kT}\right)} - 1\right] = AA^*T^2e^{-\frac{q\phi_B}{kT}}\left[e^{\left(\frac{qV}{\eta kT}\right)} - 1\right] \qquad (4.1)$$

Here, I_S is the reverse saturation current, q is the electronic charge, A is the contact area, A* is the effective Richardson Constant, η is the diode ideality factor, T is the temperature, ϕ_B is the SBH, and k is the Boltzmann constant. The contact area for the junction is 0.2117 mm2 (obtained from SEM image) and A* for p-Si is 46.32 $Acm^{-2}K^{-2}$ [31]. From Figure 4.2(c), the extrapolated ideality factor and SBH using the thermionic emission model are 1.68 and 0.648 eV, respectively, which are quite close to those reported in the literature [20].

The higher ideality factor has been attributed to various factors including SBH variation with reverse bias arising from graphene's bias dependent work function, Schottky Barrier inhomogeneity and image charge induced SBH lowering [32-34]. Due to graphene's bias dependent work function, with the increase in reverse bias magnitude the SBH at graphene/Si interface decreases and correspondingly the reverse current increases, and is noticeable from the inset of Figure 4.2(c).

4.3. Sensing Response

After separate deposition of 3 nm Pd and 2 nm Pt over the graphene/Si heterojunction on two different devices, both forward and reverse currents were found to increase, however, the I-V characteristics still remained distinctly Schottky (dashed blue curve in Figure 4.2(c) and (d)). The increase in current is due to the reduction in graphene/Si barrier height caused by "p-type doping" of the deposited Pd/Pt layer. Such doping of graphene by metallic thin

films resulting in significant movement of the Dirac point, to both right and left (depending on the work function of the deposited metal compared to that of graphene), has been reported earlier [35]. Since the work function of Pd and Pt [36] is much higher than graphene (4.5 eV), electrons from graphene are expected to move to Pd/Pt, effectively inducing p-type doping in graphene, and causing downward movement of its Fermi level. This effect has been both theoretically predicted [37] and experimentally observed for Pt-functionalized graphene [12]. The downward movement of graphene Fermi level would then reduce the hole barrier height at the graphene/Si interface, which was experimentally observed as the SBH changed from 0.648 to 0.546 eV after the 3 nm Pd deposition and 0.643 to 0.592 eV after 2 nm Pt deposition. To investigate the effect of H_2, exposure, the I-V characteristic was retaken after 10 minutes of 1000 ppm H_2 flow as shown by the orange dotted curve in Figure 4.2(c) and (d). From Figure 4.2(c), we find that both forward and reverse currents decreased in magnitude with H_2 exposure, which is expected since the SBH increased from 0.546 to 0.59 eV in case of Pd functionalized device. The SBH increase can be explained by the following mechanism: In presence of Pd or Pt, H_2 dissociates into atomic hydrogen and forms metal hydrides (PdH_x, PtH), which have lower work function then the pure Pd and Pt, respectively [11-13]. This results in electron transfer to graphene reducing its p-doping, and increasing hole barrier height at the graphene/Si interface. However, the percentage change in forward current is much smaller than the reverse current, i.e. at 4V forward bias, the current decreased from 3.56 to 2.81 mA (21.06% change) while at -4 V bias it changed from -256.65 to -9.42 μA (96.33%). We have extracted the series resistance from the diode forward characteristics (following the similar methods employed in reference 20), and found it to change from 1.05 (pre-

exposure) to 1.32 kΩ, after exposure to 1000 ppm H_2, for Pd functionalization. In terms of resistance change, a commonly used metric for H_2 sensing [11-13], the changes at 4 V forward and reverse bias are ~1.26 and ~27 times, respectively. Clearly, the sensitivity (defined as the ratio of change in resistance due to H_2 exposure to the initial resistance before exposure, expressed as a percentage) is dramatically enhanced in reverse bias. In addition, the power consumed is much reduced in reverse bias, only 1.03 mW, compared to 14.24 mW in forward bias, which is ~14 times higher. Reverse bias operating power can be further reduced to μW range simply by scaling down the device dimensions. However, the device dimensions should be carefully chosen to keep signal to noise ratio (SNR) acceptable since SNR degrades as the device is scaled down. A similar response is also observed for Pt functionalization, and shown in Figure 4.2(d), the SBH changed from 0.592 to 0.623 eV with the exposure of 1000 ppm H_2 and at -4 V bias, current decreased from -47.8 to -14.94 μA (68.74% change) which is higher than the response obtained at 4 V forward bias, 1.168 to 1.1017 mA (5.68% change). The series resistance increased from 3.11 to 3.44 kΩ after exposure to 1000 ppm H_2.

Noble metal nanoparticle functionalization induced doping in graphene, resulting decrease in the heterojunction interface Schottky barrier height and subsequent increase after H_2 exposure is also confirmed by capacitance-voltage (C-V) measurement which is discussed at the end of this chapter.

To directly compare the performances of Graphene/Si chemi-diode and graphene chemiresistor, they were fabricated side by side on the same chip (schematically shown in Figure 4.2(a)) using the same graphene sample and functionalized by 3 nm Pd and 2 nm Pt, separately. Performances of both chemi-diode and chemiresistor sensors with 3 nm Pd

functionalization upon exposure to 200 ppm H_2 for 10 minutes, at -5V bias are shown together in Figure 4.3(a). Graphene/Si diode sensor shows 122% resistance change (red curve), while the response for graphene chemiresistor is a mere 2.9% (blue curve). Thus, more than 40 times performance enhancement for the same exposure and bias conditions are observed for the chemi-diode sensor compared to the chemiresistor sensor. Of course,

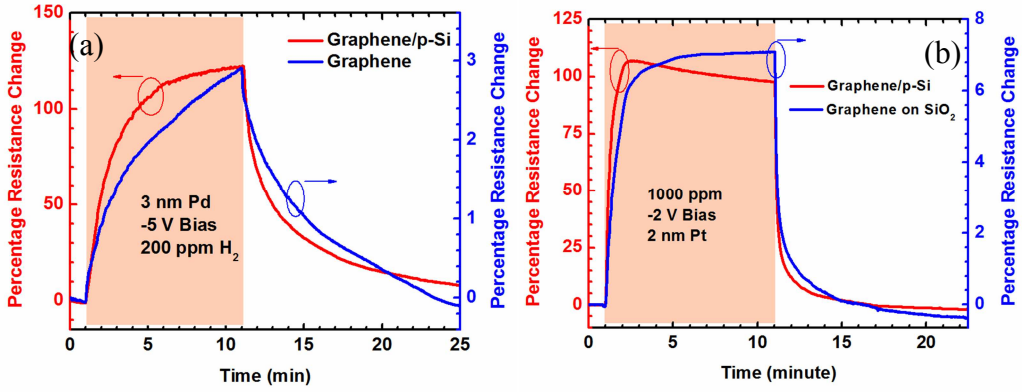

Figure 4.3 (a) Comparison between the H_2 responses for similarly functionalized graphene/p-Si chemi-diode device and graphene chemiresistor on SiO_2, fabricated on the same chip. (a) Response for 200 ppm H_2 (pink box) in case of Pd- functionalization where red one (left y-axis) is for graphene/p-Si chemi-diode and blue one (right y-axis) is for graphene chemiresistor. (b) Response for 1000 ppm H_2 (pink box) when Pt-functionalization was employed where red curve (left y-axis) is for graphene/p-Si chemi-diode and blue curve (right y-axis) is for graphene chemiresistor.

the operating power for chemiresistor is 46.425 mW, which is much higher than 64.7 μW for the diode sensor. The performance enhancement of the graphene/Si diode sensor was verified with 2 nm Pt decoration as well. The responses are shown in Figure 4.3(b) for 10 minutes of 1000 ppm H_2 exposure at -2V bias condition. Once again the diode sensor

showed a much higher sensitivity of 106% compared to only 7% for the chemiresistor, a 15 fold improvement.

We would like to point out here that the performance of our graphene/Si chemi-diode sensor is at least an order of magnitude improved over other graphene based H_2 sensors reported utilizing the same Pd functionalization [11, 38]. The performance is also better compared to the high-sensitivity graphene nano-ribbon based sensor [13], which owes its high sensitivity to the porous nature and large surface area of the nanoribbons. The very high sensitivity of our sensors can be attributed to the usage of a Schottky junction to perform sensing, where the current changes exponentially with the change in SBH induced by H_2 adsorption. The Schottky diode type H_2 sensor based on Pd/semiconductor (i.e. Pd/Si [39] and Pd/InP [40]) junction has been reported earlier, utilizing various methods for depositing Pd contacts and resulting in high H_2 sensitivity. It should, however, be kept in mind that the role of the Pd layer in our sensor is that of a functionalization layer, i.e. it is not directly forming a Schottky contact with the Si, it is just allowing graphene/Si junction to respond to H_2 by facilitating its adsorption and changing the SBH. In addition, the Fermi level of the graphene layer may be altered using the reverse bias to tune the hydrogen sensitivity, a feature that is completely unique to this sensing paradigm as compared to metal/semiconductor Schottky diode where modulation of SBH by inducing strain in a piezoelectric semiconductor, such as ZnO, have shown improvements in tactile [41] and O_2 [42] sensitivity.

The response of Pt (2 nm) functionalized sensor was investigated for H_2 concentration varying from 1000 to 10 ppm at a fixed reverse bias of -4V. The sensing response illustrated in Figure 4.4(a) can be seen to vary from 103 to 5.5% as the H_2

concentration changes from 1000 to 10 ppm, for 15 minutes exposure. As mentioned earlier, an advantage of the sensor operation in reverse bias is that the bias magnitude can be varied to change the Fermi level of graphene and consequently tune the sensor response. With the higher reverse bias applied to the graphene/Si diode, the graphene Fermi level moves further down [33, 43], compared to the donor states induced by the metal hydride and the graphene/Si SBH will decrease. Thus, in presence of H_2, more electrons would transfer to graphene, which will in turn change the SBH by a larger amount, and the sensitivity can be expected to be higher. To verify this concept, negative voltage biases varying from -1 to -5 V were applied to the p-Si (with 1 nm Pt and Pd functionalization layers), and the sensor responses upon exposure to 1000 ppm H_2 were recorded. Here, the statistical errors were within ~ 10% of the mean values of sensitivity plotted in the graph. For the 1 nm Pt deposited device the response varied from 27.5 to 77.5% for the aforementioned voltage range, with higher rise rate observed for the larger reverse bias voltages, which also resulted in higher peak response (Figure 4.4(b)). To further substantiate the idea, the responses of the 2 nm Pt functionalized device (which are shown in Figure 4.4(a) for -4 V bias) were retaken at -8V bias, and shown in Figure 4.4(c). The percentage resistance change increased from 5.5% at -4V to 13% at -8V for 10 ppm H_2 exposure over the same 10 minute duration. In fact, this also enabled detection of H_2 down to 1 ppm level, which is significant, as it is close to the atmospheric background of 0.6 ppm [24].

Since, our sensing experiments were conducted in atmospheric conditions, strictly speaking the sensor response for 1 ppm H_2 exposure actually corresponds to ~0.4 ppm of H_2 concentration. Utilizing an optimized Pd coating the sensor sensitivity was significantly

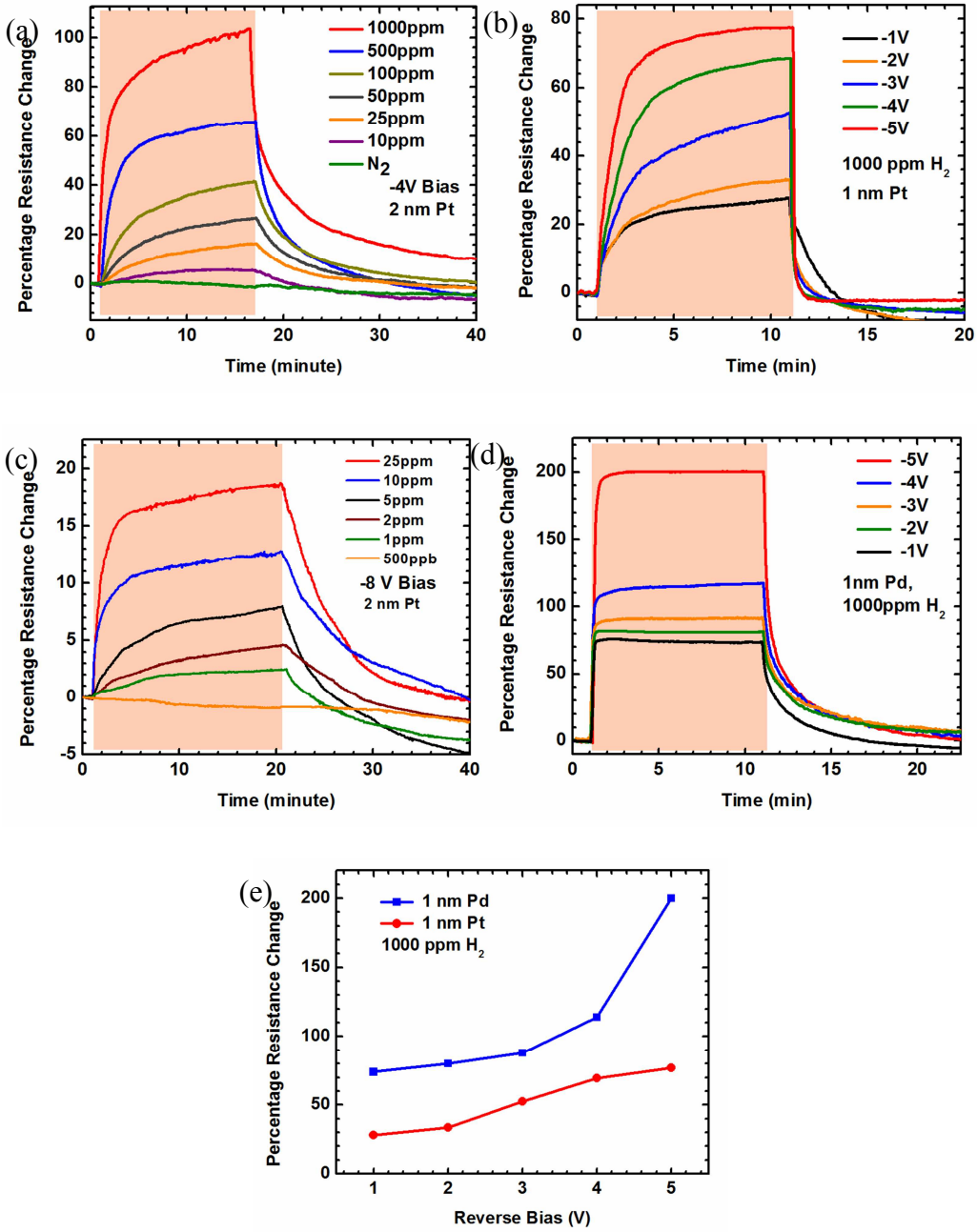

Figure 4.4 (a) Percentage resistance change of Pt-deposited graphene/p-Si device at -4 V bias for different H_2 concentration in the range of 1000-10 ppm and in N_2 environment (pink box). (b) Bias dependence of sensor response for 1000 ppm H_2 (pink box) as the voltage was changed from -1 to -5 V for Pt-functionalized device. (c) Sensitivity enhancement at higher bias (-8V) for the same device with response shown in part (a) for applied bias of -4V. (d) Bias dependence of sensor response for 1000 ppm H_2 (pink box) as the voltage was changed from -1 to -5 V for Pd-functionalized device. (e) Comparison between the responses for Pt and Pd-functionalized sensor at

enhanced (explained later), which highlights the possibility of performing detection of H_2 in the ppb level in a controlled environment. These results clearly indicate that the sensitivity of the graphene/Si chemi-diode sensor is significantly tunable with magnitude of reverse bias, which is not possible with typical metal/semiconductor diode sensors.

Since Pd has a 3 times higher H_2 solubility compared to Pt (while having same H_2 diffusion coefficient) [44], it causes a larger reduction in p-type doping upon H_2 adsorption, which can result in a larger increase in SBH, hence Pd functionalized graphene/Si chemi-diode sensors are expected to show better response than Pt functionalized ones. Indeed for the 1 nm Pd functionalized device the response varied from 200% at -5V to 74% at -1 V (Figure 4.4(d)), which is ~2.5 times higher compared to 1 nm Pt functionalized sensor for the same applied bias (Figure 4.4(b)). Additionally, there are significant differences between the Pt and Pd coated devices in terms of the transient responses. For the former, the response time is much slower than the later, while the recovery time is somewhat faster. This is however expected due to higher H_2 solubility in Pd, which leads to higher concentration in the Pd functionalization layer, which would make the response time faster but the recovery time a little slower. The sensitivity for Pt and Pd functionalized (1 nm thick metal coating) devices are compared in Figure 4.4(e) for various reverse bias voltages from where it is apparent that the later always show better sensitivity to H_2 irrespective of the voltage bias. Interestingly, with increasing reverse bias, the sensitivity of the Pd–coated sensor keeps increasing sharply, while that of the Pt-coated sensor displays a saturating trend.

Defining the response time as the time elapsed to attain 50% of the maximum resistance change, we find that for Pt-functionalization (Figure 4.4(a)), the response time

increases from 38 to 180 sec as the H_2 concentration decreases from 1000 ppm to 25 ppm. This definition of response time deviates from the traditional definition (which considers the time elapsed between 10% and 90% of the maximum value), but is more practical for sensor design since it is proportional to the rise rate, and has been used earlier.[13] The observed variation in response time with concentration is consistent with earlier observations for graphene nanoribbon network based sensor [13], and is actually expected since under lower concentration additional time is needed for same number of H_2 molecules to get adsorbed. Using similar definitions, the recovery time is found to increase from 84 sec for 1000 ppm to 160 sec for 25 ppm H_2. Careful consideration of Figure 4.4(b) and (d) indicates that the response and recovery time generally improves at higher negative biases. For the Pt-functionalized device and 1000 ppm H_2 exposure, the response and recovery times are both ~44 sec for 1 V reverse bias, which reduces to 42 sec and 4 sec, respectively, for 5 V reverse bias. The response times for the Pd functionalized device for 1000 ppm H_2 exposure are much lower at 6 sec for 1 V reverse bias which however remains almost the same for 5 V reverse bias. The recovery times are 34 sec and 18 sec for 1 and 5 V reverse bias, respectively.

Thicker Pd layer is expected to improve the H_2 sensitivity in two ways. First, it would lower the graphene Fermi level by a larger magnitude due to higher p-type doping, which would improve sensitivity as discussed below. Second, it would adsorb higher volume of H_2, and cause higher movement of the graphene Fermi level, thereby resulting in higher sensitivity. In fact, a previous study on graphene chemiresistor based H_2 sensor [38] indicate that 3 nm Pd functionalization layer provides maximum sensitivity to H_2. From the I-V characteristics, we find that higher Pd thickness of 3 nm changes the

graphene/Si SBH by 102 meV compared to 61 meV caused by 1 nm Pd deposition. This means the graphene Fermi level moves further down by 3 nm Pd deposition, which causes the SBH to be lower (lower resistance) initially, so with H_2 adsorption, the relative change in resistance becomes much larger. Sensing experiments were carried out using the 3 nm Pd functionalized chemi-diodes, with the H_2 concentration varying from 1000 to 2 ppm, with exposure duration of 10 minutes, at a fixed reverse bias of -4 V.

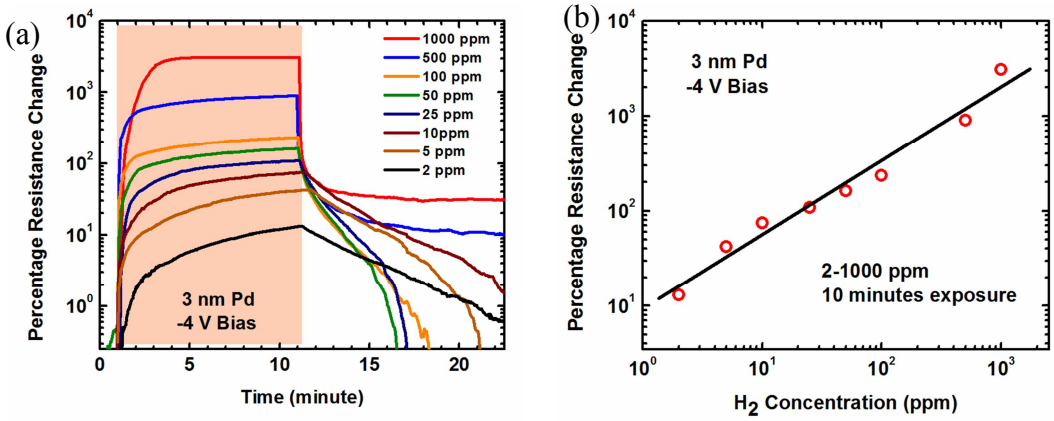

Figure 4.5 (a) Responses of 3 nm Pd functionalized graphene/p-Si device for H_2 concentration ranging from 1000 to 2 ppm (pink box) for 10 minutes exposure. (b) Sensor response as a function of H_2 concentration plotted in log-log scale. The solid straight line shows a least square fit to the data.

We find from figure 5(a) that sensitivity changes from 13.55% to 3088% as the H_2 concentration increases from 2 to 1000 ppm, where, the statistical errors were within ~10% of the mean values of sensitivity plotted in the graph. The response time is increased from 90 sec to 270 sec as the H_2 concentration changes from 1000 to 2 ppm. The recovery times are very fast, taking only 1 sec to recover to 50% of the maximum resistance change for 1000 ppm H_2. Interestingly, the full recovery times are faster for the smaller concentrations of H_2 as can be seen from Figure 4.5(a), with complete recovery observed within a few

minutes for most concentrations other than 500 and 1000 ppm. This is probably due to the larger amount of H_2 adsorption by thicker Pd layer (3nm) functionalized chemi-diode compared to that of 1nm Pd functionalized graphene/p-Si device, which recovered completely as shown in Figure 4.4(d). The plot of sensitivity versus H_2 concentration [Figure 4.5(b)] indicates that the sensitivity in these sensors varies almost linearly with the H_2 concentration when both of them are plotted in logarithmic scale. The work function change of the Pd layer (and hence the SBH) is expected to vary linearly with log of H_2 concentration [40], while the sensor current, which controls the sensitivity, varies exponentially with the SBH. Thus, the log-log relationship between H_2 concentration and sensitivity is expected to be linear as observed in Figure 4.5(b). It is noteworthy that this exponential behavior is different from that obtained previously from graphene and graphene nanoribbon network based chemiresistive H_2 sensors, where the sensitivity got saturated at higher H_2 concentration (plotted in log scale) [11,13,45]. This difference in the sensing response, is however expected, and follows from the difference in the detection principles of the chemiresistor and the proposed reverse biased chemi-diode sensor as discussed above.

To further validate H_2 sensing mechanism of the diode sensor, capacitance-voltage (C-V) measurement has been carried out at three different stages, as fabricated device, after 2 nm Pd deposition and finally, after 1000 ppm H_2 exposure. The C-V measurements were performed on the sensor using HP 4284A Precision LCR Meter with a frequency range of 20 Hz to 1 MHz. A four terminal pair scheme was used for the measurements. The ac signal amplitude was chosen as 50 mV (rms) with a frequency of 3 kHz. The dc reverse bias was

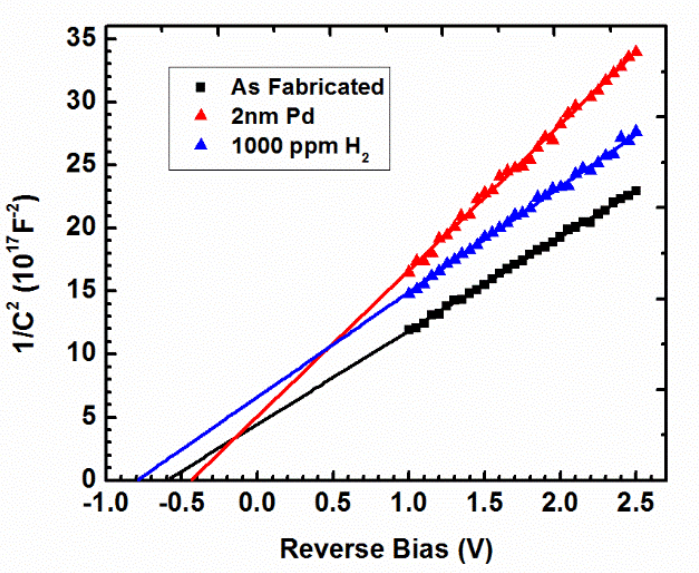

Figure 4.6 Capacitance-Voltage (C-V) plot of Pd-functionalized graphene/p-Si Schottky diode and effect of H_2 exposure.

varied from 1 to 2.5 V. As obtained measurements results are plotted in the widely used $1/C^2$ – V format to extract the built-in voltage (V_{bi}) using the following equation,

$$1/C^2 = 2(V_{bi} + V_R)/(q \in_S N_{A/D}) \qquad (4.2)$$

Here, q is the electronic charge, ε_s is the semiconductor permittivity, and $N_{A/D}$ is the acceptor/donor doping [46]. Figure 4.6 is showing the C-V plots which are linearly extrapolated and V_{bi} are determined as 0.58 eV for the initial diode, 0.44 and 0.79 eV after 2 nm Pd deposition and 10 minutes exposure to H_2, respectively. The graphene/p-Si SBH is given as, $\phi_B = V_{bi} + (E_F - E_V)$, where E_F is the Fermi level and E_V is the valance band edge of Si. $E_F - E_V$ is estimated to be ~ 0.2 eV for the p-type Si used from the resistivity of 1 – 10 Ωcm specified by the manufacturer. Thus, graphene/p-Si diode SBH becomes 0.78 eV, which is in good agreement with earlier results. [33,47] The SBH determined from C-V measurement is higher than that obtained from I-V measurements, i.e. 0.78 and 0.65 eV, respectively for graphene/p-Si diodes. The difference can arise partly from the uncertainty

in determining $E_F - E_V$, and also from Schottky barrier inhomogeneity and additional leakage paths at the junction, which generally underestimates the SBH determined from I-V measurements [32-34]. The SBH reduced from 0.78 to 0.64 eV after 2 nm Pd deposition due to its p-type doping of graphene as explained before. After 10 minutes of 1000 ppm H_2 exposure, the SBH jumped up from 0.64 to 0.99 eV due to PdH_x formation which decreases the hole density in graphene and increases the interface barrier for carrier flow. Large increase in SBH also substantiates the huge response of the diode sensor towards H_2 compared to similar electron donor molecular species NH_3 which has been reported in reference 48.

Finally, both the Pd- and Pt-functionalized graphene/Si diode sensors showed good repeatability in terms of response and recovery when subjected to several cycles of H_2 exposure and recovery in air as shown in Figure 4.7(a) and (b), respectively.

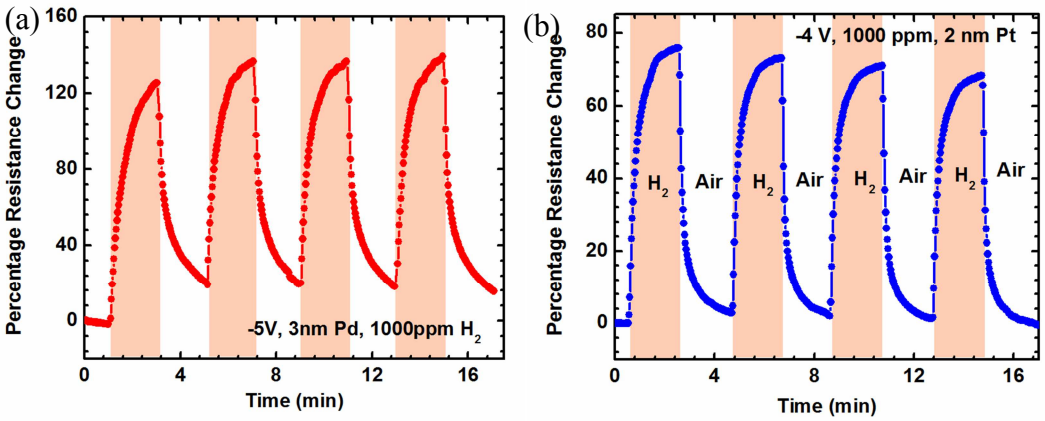

Figure 4.7 Sensor response for repetitive cycles of 1000 ppm H_2 exposure (pink box) and recovery in air for (a) Pd-functionalized, and (b) Pt-functionalized graphene/p-Si Schottky diode sensor. Both the sensors are showing excellent response and recovery even in 2 minutes of exposure and recovery time.

In conclusion, Pt and Pd functionalized graphene/p-Si heterojunction chemi-diode H_2 sensor with very high sensitivity, down to sub-ppm level, has been demonstrated. These heterojunction diode sensors show at least an order of magnitude higher response compared to the graphene based chemiresistor type sensors for both Pd and Pt-functionalization, due to exponential dependence of the reverse bias diode current on the molecular adsorption induced SBH change. In addition, the reverse bias operation of these sensors enables them to perform sensing with very low power consumption. The magnitude of the reverse bias can be effectively utilized to modulate the Fermi level of graphene, and hence the graphene/Si SBH, leading to tunable sensitivity over a wide range of analyte concentration.

CHAPTER 5

IMPEDANCE SPECTROSCOPIC ANALYSIS OF FUNCTIONALIZED GRAPHENE/P-SILICON SCHOTTKY DIODE FOR SENSING APPLICATION

5.1 Introduction

Modulation of electrical properties at the interface of heterostructure comprised of two dimensional (2D) materials themselves as well as with other dimensional materials, gained significant research interest in last few years due to the possibility of applications ranging from electronics to sensing [1-3]. Surface functionalization of 2D materials not only modify structural, electronic and optical properties, also increases the potential applications [4-7]. Metallic nano-particle decoration is one such way of functionalization, in addition to doping of 2D materials, it can enhance the sensitivity of gaseous molecules and also facilitates chemical sensing in cases where the material is not sensitive to particular analyte(s). In order to exploit the complete potential of the sensor, it is necessary to understand the underlying mechanism. In the present study, reverse bias operation of metal nano-particle functionalized graphene/Si diode has been utilized to study polar molecular (NH_3) sensing, the change in reverse current which results from the change in junction resistance and capacitance. For complete understanding of the mentioned electrical characteristics at the graphene/Si hetero-interface, recently impedance spectroscopy (IS) appeared as a helpful technique [8, 9]. Obtained impedance spectra can be interpreted by

fitting with proper circuit model and extrapolation of equivalent electrical parameters. Hence, quantifying the change in equivalent parameters in presence of different molecular analytes would lead to highly sensitive and even selective multimodal sensing system.

There has been several reports on Graphene/Si diode sensor [3,6,8,9], however, the effect of metal nanoparticle (NP) on sensing of polar molecules such as NH_3, and comprehensive impedance spectroscopic analysis especially on functionalized sensor has not been carried out yet. In this work, dc amperometric measurement of graphene/p-Si Schottky diode has been carried out to study the *Polar* gaseous molecular sensitivity enhancement by noble metal (Pt, Pd and Ag) NP functionalization. In addition to the dc amperometric measurement, analyzing the IS response utilizing an equivalent circuit model, the change in junction capacitance and resistance has been obtained for both polar NO_2 and NH_3, and non-polar H_2 gaseous species. Finally, change in 3dB cut-off frequency for each gas exposure has been utilized as a sensing parameter. In addition to ultra high sensitivity, exploitation of changes in the mentioned electrical parameters would pave the path for selective sensing paradigm.

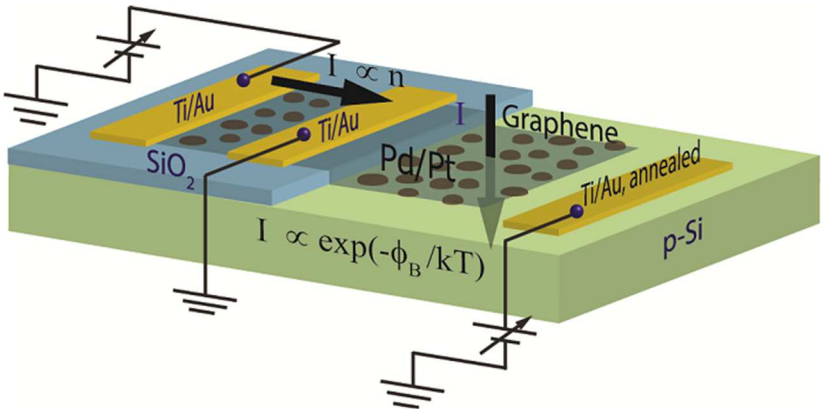

Figure 5.1 Device schematic and biasing scheme of Pt/Pd functionalized graphene chemiresistor and graphene/Si Schottky diode sensors fabricated on the same chip. Gray spots indicate metal decoration.

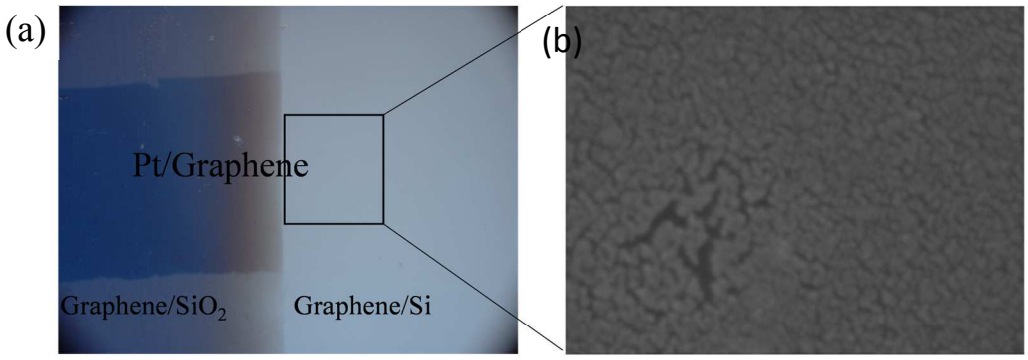

Figure 5.2 (a) Optical Image of graphene/p-Si heterojunction Schottky diode sensor with 2 nm Pt-functionalization, graphene is visible on SiO_2, and Pt-functionalization is also showing contrast on SiO_2 region covered by graphene. (b) SEM top view image showing Pt nanoparticle on graphene lying on Si corresponds to the box approximately from the optical image.

5.2 Sensitivity enhancement by Metal nano-particle functionalization

Graphene/p-Si Schottky diode fabrication steps was described in chapter 3 including Pt and Pd NP functionalization for H_2 sensing. For this study, in addition to Pt and Pd functionalization for sensitivity enhancement, Ag NP functionalization has been utilized. Figure 5.1 shows the functionalized graphene/Si chemi-diode sensor and graphene chemiresistor fabricated on the same chip for comparative study. Figure 5.2(a) and (b) shows the optical and SEM image of the fabricated device with metal NP functionalization. From the SEM, it can be concluded that, due to very small duration of metal deposition, it didn't form a continuous layer. With grain size varying between 20-30 nm, we can easily consider them as nano-particles. 2 nm Ag was deposited by electron beam evaporation method at ultrahigh vacuum of 1.5×10^{-6} Torr. Similar to Pt and Pd NPs, Ag NP also modifies the electrical characteristics of the diode as shown in Fig 5.3. Although forward current decreased and reverse current increased slightly after Ag nano-particle functionalization, the graphene/p-Si device characteristics remained rectifying in nature.

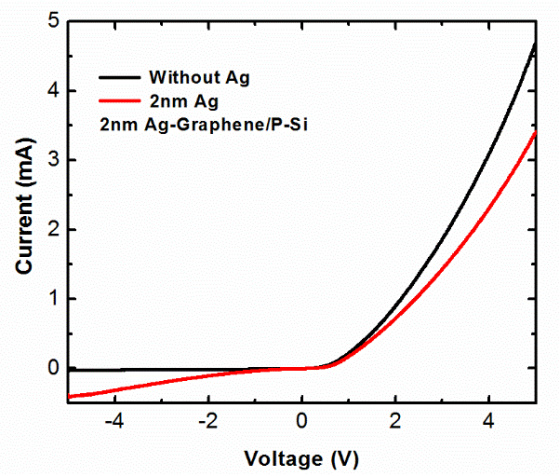

Figure 5.3 Current-Voltage (I-V) characteristics of graphene/p-Si (black) and after 2 nm Ag-functionalization (red) showing rectifying character.

The SBH changed from 0.7 eV to 0.68 eV after Ag NP functionalization as extracted utilizing the thermionic emission model, described by equation 5.1 [10].

$$I = I_S\left[exp\left(\frac{qV}{\eta kT}\right) - 1\right] = AA^*T^2 exp\left(-\frac{\phi_B}{kT}\right)\left[exp\left(\frac{qV}{\eta kT}\right) - 1\right] \qquad (5.1)$$

Here, I_S is the reverse saturation current, q is the electronic charge, A is the contact area, A^* is the effective Richardson Constant, η is the diode ideality factor, T is the temperature, ϕ_B is the SBH, and k is the Boltzmann constant. When plotted in logarithmic scale, the intercept on y-axis will give the saturation current, from which the SBH was determined with the knowledge of the diode area A and Richardson's constant A^*.

Figure 5.4 shows the effect of three different types of NP on NH_3 sensitivity compared to graphene chemiresistor. NH_3 concentration was varied sequentially from 550 ppm to 10 ppm. Pristine graphene chemiresistor showed only 8% sensitivity for 550 ppm NH_3 compared to 40, 33 and 20% for Pt, Pd and Ag NPs, respectively. Increase in sensitivity due to Pt, Pd and Ag NPs can be easily explained by their adsorption of NH_3 and diploe formation at the interface with graphene. NH_3 gas dissociates at the surface of NPs and

dissolve into the particles, and forms dipole. The negative charged part of the dipole is at the interface with graphene and neutralize the p-doping of graphene to some extent. The reduction of holes in graphene increases it resistance, and sensitivity in terms of resistance change increases. The sensitivity enhancement by these NPs directly related to adsorption ability, Pt adsorps the maximum among the three types of nanoparticle [11,12] and showed highest sensitivity. For all three types of NPs, the sensors showed excellent repeatability as well. Desorption of NH_3 from the sensor is enhanced by the presence of oxygen in air [13]. Another important aspect of the NP decoration is that, all three of them showed quick recovery compared to graphene chemiresistor.

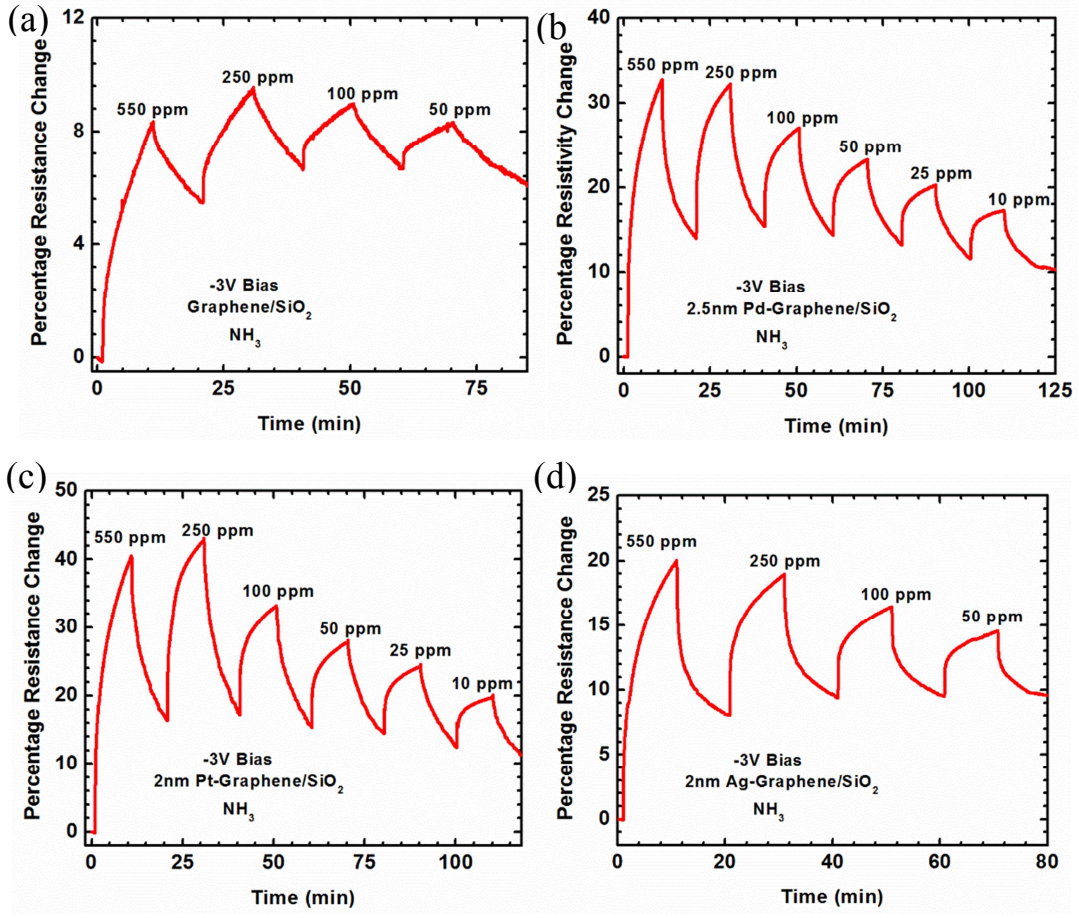

Figure 5.4 Response with NH_3 concentration variation for (a) Graphene, (b) Pd-Graphene, (c) Pt-Graphene and (d) Ag-Graphene on SiO_2 substrate

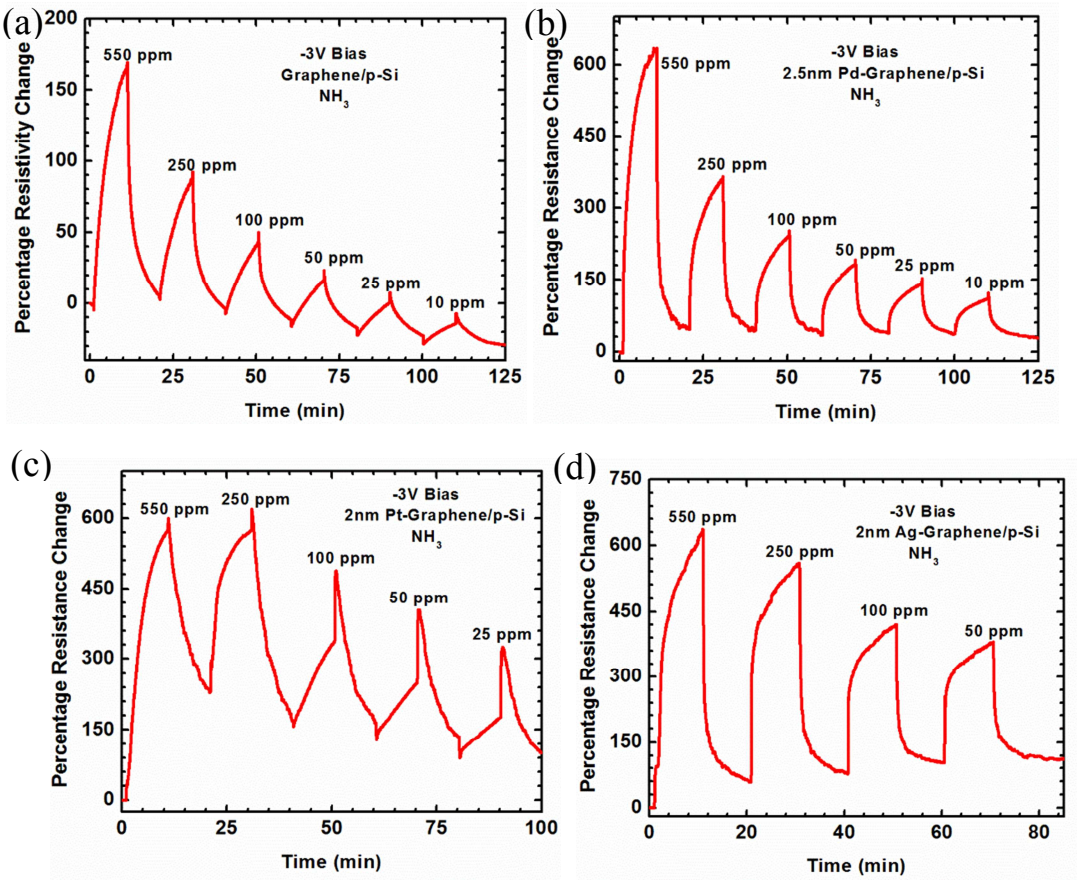

Figure 5.5 Response with NH_3 concentration variation for (a) Graphene/p-Si, (b) Pd-Graphene/p-Si, (c) Pt-Graphene/p-Si and (d) Ag-Graphene/p-Si

Figure 5.5 shows the sensitivity enhancement by NPs for graphene/p-Si Schottky diode. Pristine Graphene/p-Si diode sensor exhibited almost 20 times higher sensitivity compared to graphene chemiresistor and several times higher than the NP decorated graphene sensor. The high sensitivity of diode sensor is the result of different transport mechanism, in presence of gaseous molecules the graphene work function changes, leads to change in Schottky Barrier height (SBH). In reverse bias, current is exponentially proportional to SBH, results in huge sensitivity compared to almost linear carrier change for chemiresistor. All three NPs showed equal sensitivity enhancement in case of Diode sensor and excellent recovery. Similar sensitivity enhancement for all NPs is most likely

originating from the initial sensitivity of the sensors before NP deposition. Although Pt adsorbs the maximum NH_3, the initial sensitivity of Ag decorated device was higher resulting in equal sensitivity after NP decoration. This is also visible from the sensitivity for lower NH_3 concentration, where highest sensitivity was observed for Ag NP.

To confirm the transduction mechanism, the capacitive-voltage (C-V) measurements were carried out for Pt decorated diode sensor as shown in Fig 5.6. The measurement frequency was 3 KHz and applied reverse bias voltage range was from 1.0 to 2.5 V. Comparing Schottky diode in reverse bias condition as a parallel plate capacitor the capacitance and voltage can be described by the following equation 5.2.

$$1/C^2 = 2(V_{bi} + V_R)/q\epsilon_S N_A \qquad (5.2)$$

Here q is the electronic charge, ϵ_S is the semiconductor permittivity, and N_A is the acceptor doping [10]. Extrapolating the $1/C^2$ – V straight lines, the built-in voltage (V_{bi}) is determined as 0.47 eV for pre-exposed condition in air, and in presence of NH_3 it increased to 0.65 eV. The graphene/p-Si SBH is given as, $\varphi_B = V_{bi} + (E_F - E_V)$, where E_F is the

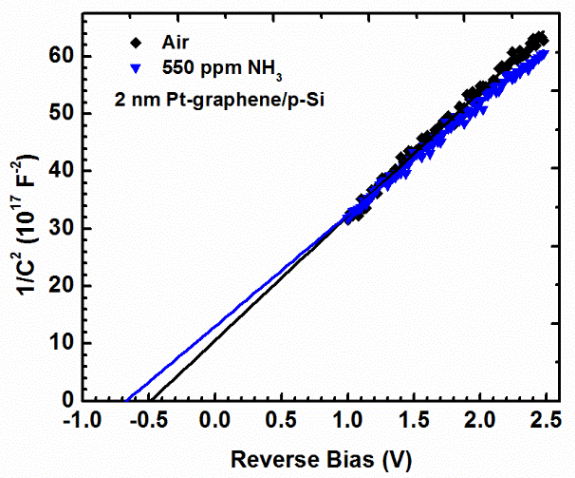

Figure 5.6 Capacitance-Voltage (C-V) plot showing increase in built-in voltage of Pt-Graphene/p-Si for NH_3 exposure

Fermi level and E_V is the valance band edge of Si. $E_F - E_V$ is estimated to be ~ 0.2 eV for the p-type Si extracted from the resistivity of 1 – 10 Ω cm as specified by the manufacturer. Hence, the SBH increase of Pt-functionalized graphene/p-Si Schottky Diode sensor due to 550 ppm NH_3 exposure is 0.18 eV. Inspecting the slope of the two extrapolated $1/C^2$ – V lines, it is obvious that due to NH_3 exposure, slope is decreasing. From equation 5.2, effect of p-Si doping is increasing considering graphene as metal and in another way, the doping in graphene is decreasing since p-Si doping is essentially fixed. Similar change has been observed for NH_3 exposure of non-functionalized graphene/Si diode senor [3] where the SBH change was 0.16 eV, less than Pt-functionalization. This reconfirmed that, noble metal nano-particle functionalization enhances the sensitivity of graphene/p-Si diode sensor by facilitating more adsorption and superior charge transfer mechanism.

5.3 Impedance Spectroscopy of Graphene/Si Diode Sensor for Multimodal Sensing

Impedance Spectroscopy (IS) is a very attractive tool to study the transport mechanism in nanoscale devices and measured impedance spectra can be electrically interpreted with a proper equivalent circuit model. IS can be applied to analyze the electronic sensor operation mechanism and change in equivalent circuit parameters could be extracted. Combining the IS along with the dc amperometric sensing response, multimodal sensing by graphene/Si Schottky diode could be achievable. For IS study, a potentiostat (Series GTM 300, Gamry Instruments, Warminster, PA, USA) has been used. Since diode characteristics is not completely linear, we can input a small AC signal in the following form,

$$E(t) = E_0 \cos(2\pi f t) \qquad (5.3)$$

Where, E(t) is the potential as a function of time, E_0 is the signal amplitude and f is the frequency, is applied to any system and the output is measured. By applying a small enough signal, as shown in Figure 5.6, a nonlinear system can become pseudo-linear with linear output,

$$I(t) = I_O \cos(2\pi ft - \emptyset)$$

$$Z = \frac{E(t)}{I(t)} = Z_O \frac{\cos(2\pi ft))}{\cos(2\pi ft - \emptyset)} \qquad (5.4)$$

Using Euler's formula, $$Z = Z_O(\cos\emptyset + i\sin\emptyset) \qquad (5.5)$$

From the expression of equation 5.5, a Nyquist plot can be made utilizing the real and imaginary parts of the impedance, giving information on the impedance of the device [4]. In addition, plotting the impedance and phase change as a function of frequency leads to bode plot, from which 3dB cut-off frequency and overall impedance change can be obtained. Modelling the device with an equivalent circuit comprised of electrical parameters for different device components which influence the electrical characteristics significantly, and fitting the circuit model with the obtained impedance spectra provides

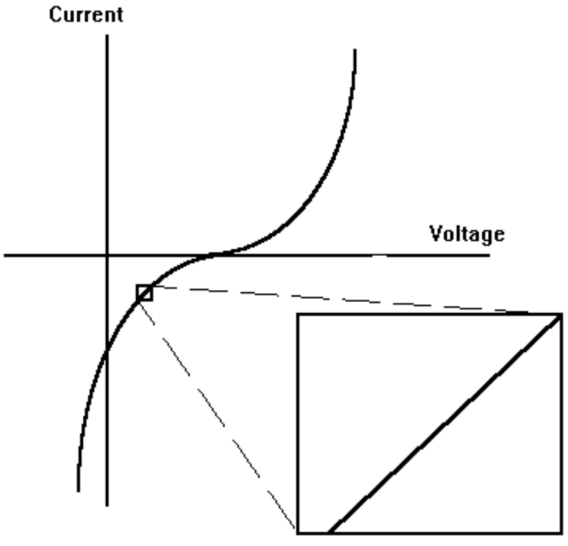

Figure 5.7 Pseudo linear response to small excitation signal

meaningful insights in to the parameters. As for example, reverse biased graphene/Si Schottky junction can be modeled by parallel connected resistor and capacitor, where the capacitance originates from the depletion region of the diode. Next, after careful inspection of the Nyquist plot, more elements can be added to include other important aspects of the real device to completely emulate its electrical response.

For the characterization of (Pt/Pd NP)-graphene/p-Si Schottky diode, 2.0 V reverse bias was applied to avoid the effect of the series resistance effect in forward bias and

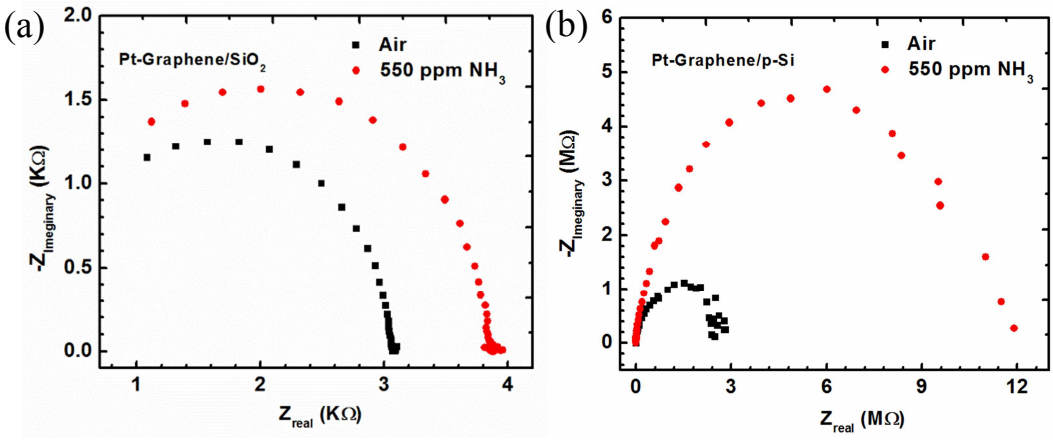

Figure 5.8 Impedance Spectra of (a) Pt-Graphene and (b) Pt-Graphene/p-Si in air and 550 ppm NH_3.

simultaneously take advantage of exponential change in reverse current with graphene work function induced SBH change with gaseous analyte exposure. 10.0 mV ac excitation was superimposed on top of the dc bias and the frequency was varied from 0.1 Hz to 300.00 KHz. The response was taken in air, 0-550 ppm NH_3, 20 ppm NO_2 and 1000 ppm H_2 exposure in ambient condition, and later analyzed with an equivalent circuit model.

For comparison purpose, Pt-graphene chemiresistor has also been characterized as shown in Fig 5.8 (a) in air and in 550 ppm NH_3. Nyquist plot for both the conditions showing the increase of impedance due to NH_3 exposure which was also observed from dc

amperometric measurement. From the partial bell shape of the plots, imaginary part of the impedance is present in addition to the real part. This indicates the presence of reactive element which is most likely from the graphene-metal contact. It has been reported in the literature that, metal-graphene contact is not perfectly ohmic and thermionic emission is the dominant charge transport mechanism across the metal-graphene contact barrier at room temperature [14]. Due to the small potential barrier at metal-graphene contact, it can be treated as reactive element in addition to contact resistance. The curve shifted in both upward and sideways after exposed to NH_3. Although both real and imaginary part of the impedance exhibited increasing nature, the change in real part is higher. Hence, the series resistance change is the dominant sensing mechanism in case of graphene chemiresistor. Also due to increase in channel resistance, injected carriers from metal contact is facing higher barrier, increasing the overall impedance originating from the combination of resistive and reactive element. The impedance of Pt-functionalized graphene/p-Si device is shown by the black dotted curve in Fig 5.8 (b) which is completely semi-circular in shape. After 550 ppm NH_3 exposure, the impedance increased as shown by the red dotted plot, both real and imaginary part was increased more than 4 times. Hence, NH_3 is impacting both resistive and reactive elements of the device impedance confirming the change in junction capacitance in addition to the resistance. Comparing the impedance change of chemiresistor and Chemi-diode, diode showed several times higher response. With NH_3 exposure, the maximum of real and imaginary part of the diode impedance shifted from 3 and 1 MΩ to 12 and 4.8 MΩ, respectively. On the other hand, for chemiresistor the respective changes are from 3.1 and 1.2 KΩ to 3.4 and 1.5 KΩ,

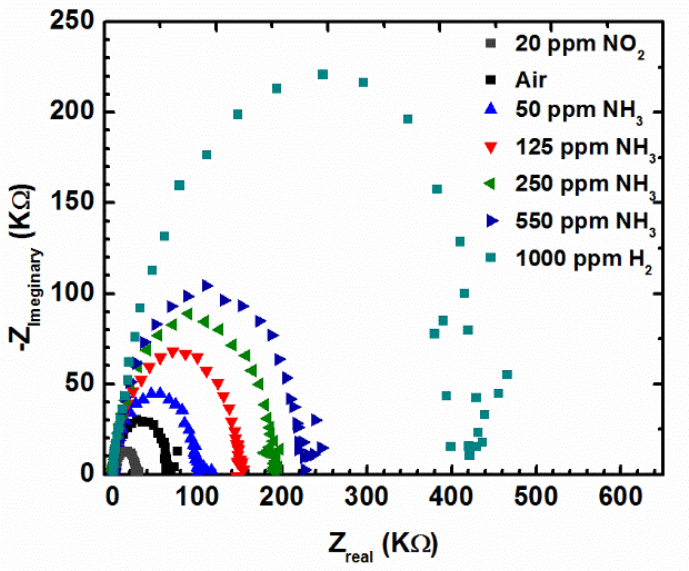

Figure 5.9 Impedance spectra of Pd-Graphene/p-Si with exposure of 20 ppm NO_2, NH_3 (0-550 ppm) and 1000 ppm H_2

respectively. Higher response is the result of different current transport mechanism, current change is almost linear due to linear carrier change in chemiresistor compared to exponential current change in diode. In case of diode, analytes change the graphene work function by linearly changing carrier concentration, work function changes the junction SBH linearly and reverse current is exponentially proportional to SBH leading to high sensitivity of diode sensor.

To examine the overall performance of the diode sensor, we have carried out the NH_3 concentration variation for Pd-functionalized graphene/p-Si device in addition to measuring the NO_2 and H_2 response. The impedance change for different NH_3 concentration is shown in Figure 5.9. With the increase in analyte concentration, the impedance showed monotonic increase and hence the sensitivity. The maximum of imaginary part of the impedance is increased from 29 to 109.72 KΩ while the increase in real part is from 72 to 226 KΩ for air to 550 ppm NH_3 exposure. On the other hand, for

NO_2 which is a hole donor increases graphene's carrier concentration and work function and reduces the interface SBH, impedance spectra reduced substantially, maximum of imaginary and real part reduced to 12.6 and 28 KΩ, respectively. For 1000 ppm H_2 which follows the similar mechanism as NH_3, impedance spectra increased substantially with maximum of imaginary and real part increased up to 220 and 465 KΩ, respectively. The large response for H_2 compared to NH_3 is due to higher H_2 adsorption ability of Pd and resulting change in work function which has been observed for H_2 in reference [6] and for NH_3 in Fig 5.5 (b).

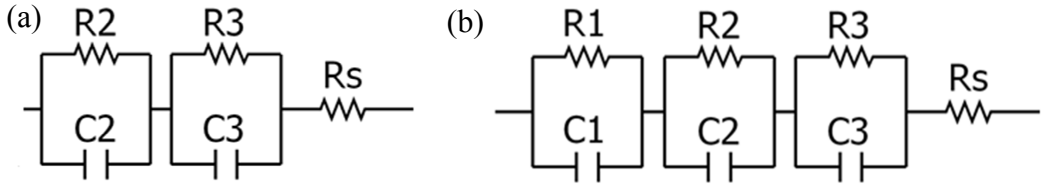

Figure 5.10 Circuit equivalent model for (a) graphene chemiresistor and (b) graphene/p-Si Schottky Diode

5.4 Analysis of Diode Sensor Impedance Spectra by Fitting Equivalent Circuit Model

Since the impedance spectra can be fitted with circuit model, both chemiresistor and diode sensor is modeled by equivalent circuit shown in Figure 5.10 (a) and 5.10 (b), respectively. The chemiresistor is represented by a pair of parallel RC and a resistor, all connected in series, where the RCs represent the graphene-Ti/Au contacts and resistor is for the graphene channel resistance. It has been mentioned already that, small energy barrier exists at graphene-metal contact which is not perfectly ohmic and resulting impedance to current flow includes reactive element. The diode sensor is modeled by three parallel RC and a resistor all connected in series where one RC is for Schottky junction, two other are taking

care of the effects of the contacts between the graphene-Ti/Au, and p-Si substrate-Ti/Au, and resistor is for diode series resistance. For that, diode equivalent circuit elements can be described as, R_S is the diode series resistance, C_1, C_2, and C_3 are the capacitances related to the Au/Ti-graphene, graphene-Si, and Si-Ti/Au interfaces, respectively, with corresponding shunt resistances R_1, R_2, and R_3. Real and imaginary part of the total impedance can be expressed as

$$Z(\omega) = Z_{Real}(\omega) - jZ_{Imaginary}(\omega) \tag{5.6}$$

For mathematical analysis of the equivalent circuit model in Fig. 5.10(b), $Z_{Real}(\omega)$ and $Z_{Imaginary}(\omega)$ can be expressed as

$$Z_{Real}(\omega) = \frac{R_1}{1+(\omega R_1 C_1)^2} + \frac{R_2}{1+(\omega R_2 C_2)^2} + \frac{R_3}{1+(\omega R_3 C_3)^2} + R_S \tag{5.7}$$

$$Z_{Imaginary}(\omega) = \frac{\omega {R_1}^2 C_1}{1+(\omega R_1 C_1)^2} + \frac{\omega {R_2}^2 C_2}{1+(\omega R_2 C_2)^2} + \frac{\omega {R_3}^2 C_3}{1+(\omega R_3 C_3)^2} \tag{5.8}$$

Fitting the circuit model in GamryEchem Analyst software, equivalent circuit parameters were extracted. The fitting of the chemiresistor response is shown by the solid lines in

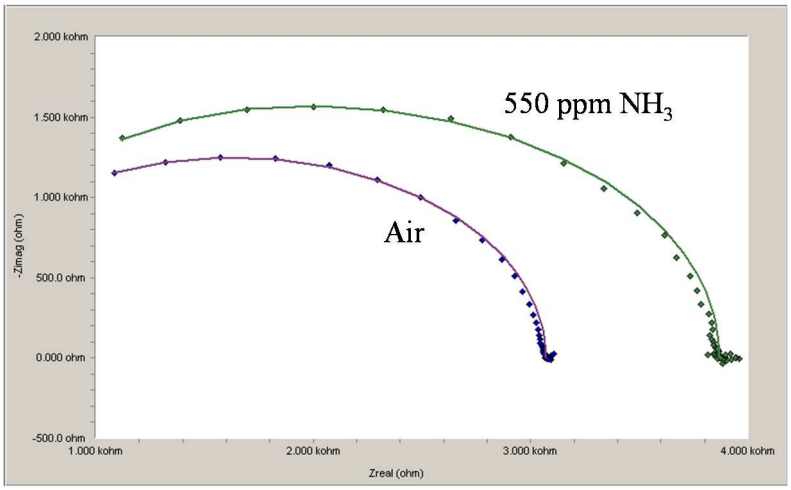

Figure 5.11 Equivalent circuit model fitting of impedance spectra of Graphene in Air and NH_3 where dotted lines are experimental results and solid lines are from circuit model fitting.

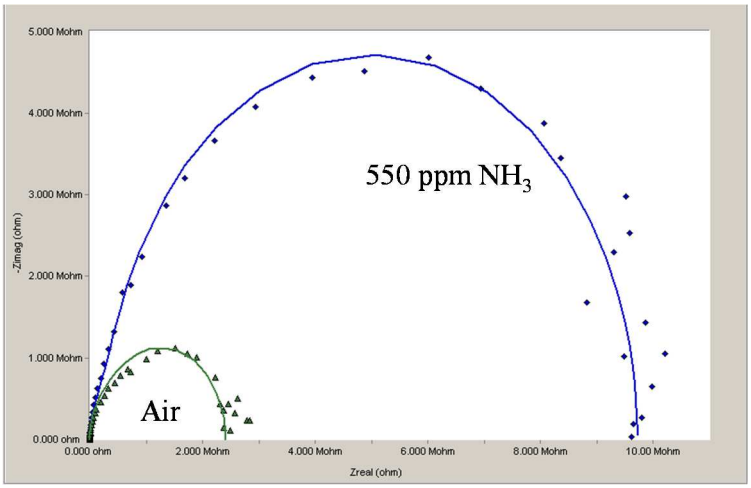

Figure 5.12 Equivalent circuit model fitting of impedance spectra of Graphene/p-Si in Air and NH3 where dotted lines are experimental results and solid lines are from circuit model fitting.

Figure 5.11 along with the experimental results by the dotted lines. The series resistance increased by 30 Ω (11 % for initial resistance of 260 Ω) after NH_3 exposure while contact resistance and capacitance change is insignificant as extracted from the fitting. Figure 5.12 shows circuit fitting for the diode sensor with Pt NP functionalization and 550 ppm NH_3 exposure where the solid lines are from fitting and dotted lines are the experimental response. From the analysis, junction resistance changed from 2 to 9.4 MΩ and junction capacitance increased from 843 to 893 pF while change in other parameters are not that significant. The combined impedance change for the diode is several times higher than the

Table 5.1 Extracted parameters from fitting the circuit models to the IS response

Device	**Parameter**	**Air**	**NH_3**
Chemiresistor	Resistance	260 Ω	290 Ω
Graphene/p-Si	Junction Capacitance	843 pF	896 pF
Graphene/p-Si	Junction Resistance	2 MΩ	9.4 MΩ

resistor and hence the sensitivity. The major change in equivalent circuit parameters are summarized in table 5.1.

Similar fitting of the Pd-functionalized device for NH_3 concentration variation [Fig. 5.13 (a)] provides the changes for junction resistance and capacitance. The change in the resistance and capacitance for different NH_3 concentration is shown in Fig. 5.13 (b), where both the parameters showed sharp increase initially and later hint of saturation for

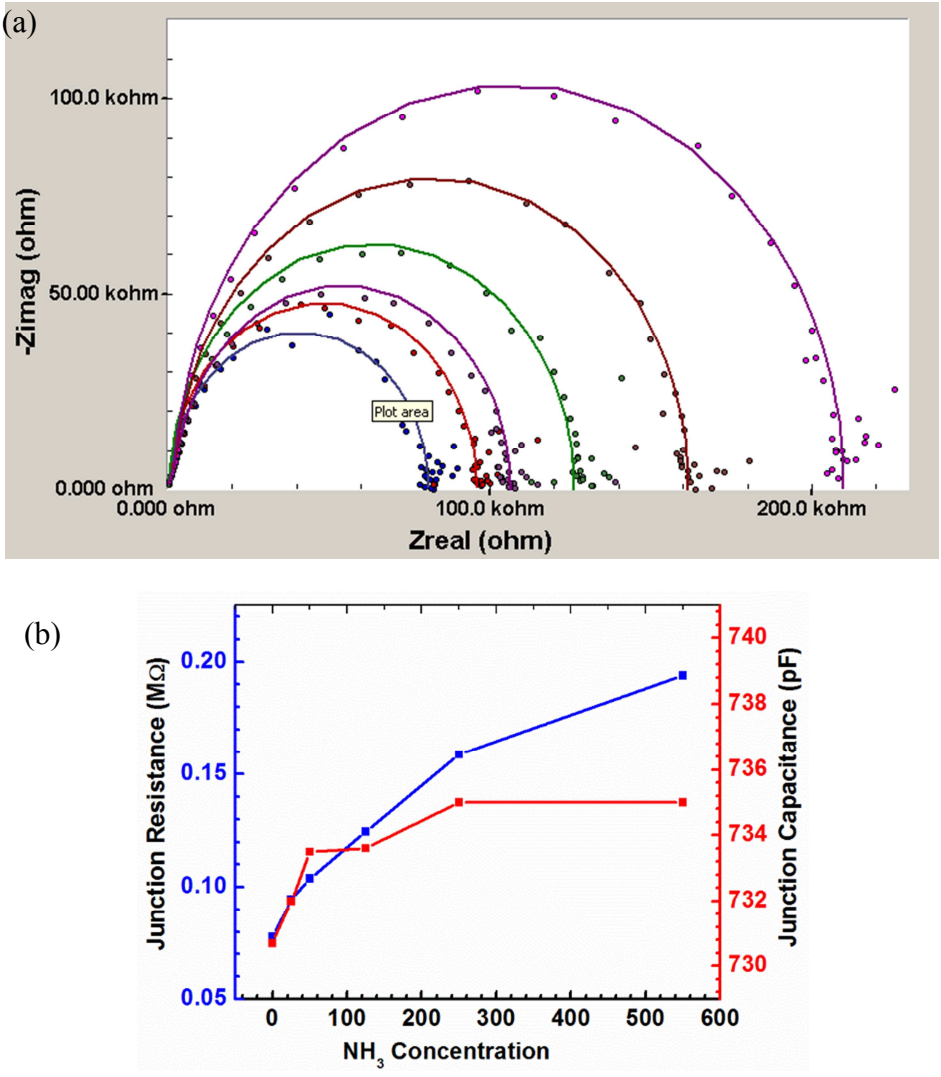

Figure 5.13 (a) Circuit model fitting to NH_3 (25-500 ppm) response of Pd-Graphene/p-Si. (Dotted lines are experimental results and solid lines are from circuit model fitting), and (b) extracted resistance and capacitance variation with NH_3 concentration

resistance and complete saturation for the capacitance change. The resistance increased from 0.075 to 0.2 KΩ and the capacitance change is from 730 to 735 pF. The change for Pd NP device is lower than the Pt due to less NH_3 adsorption ability of the former compared to the later [11]. One more point to mention here, the initial overall impedance of the Pd-functionalized device is much lower than the previously shown Pt-functionalized device

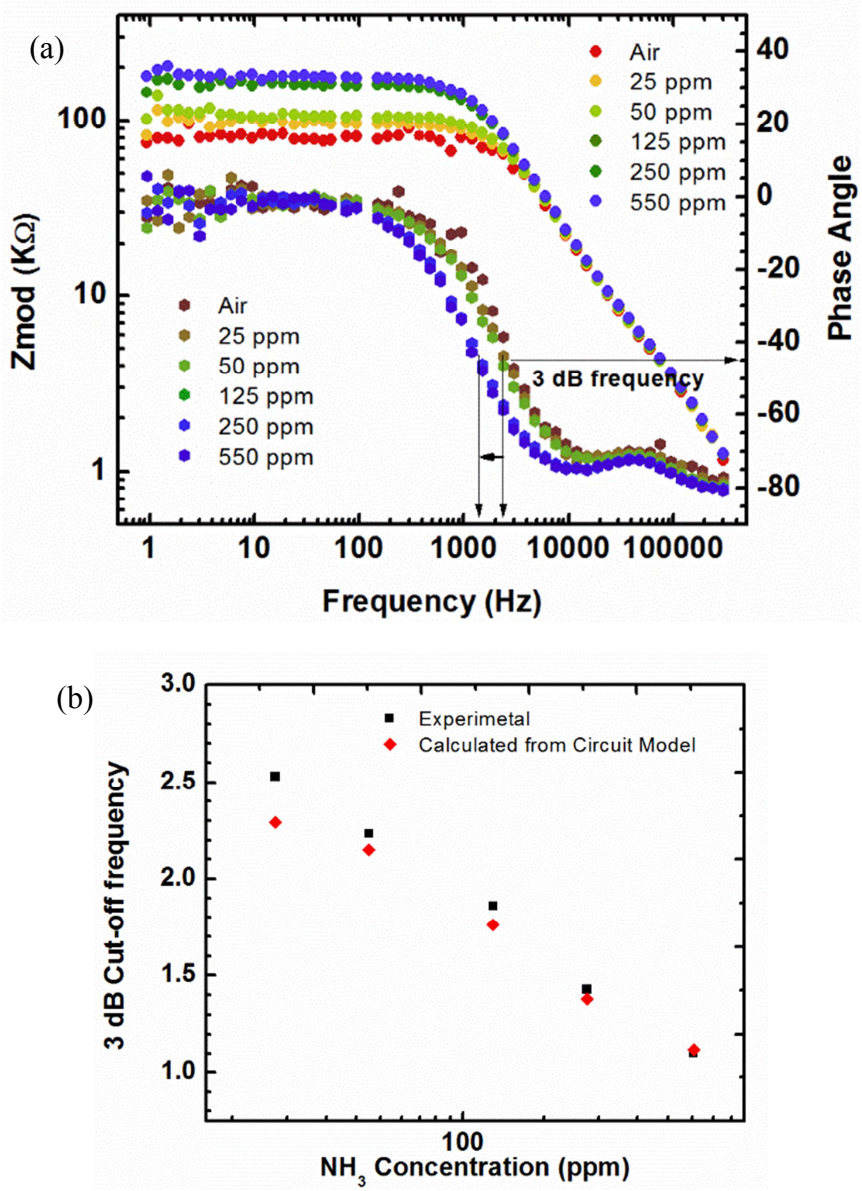

Figure 5.14 (a) Bode plot is showing the 3-dB cut-off frequency shift at different condition (b) Comparison between experimental and theoretical 3-dB cut-off frequency.

even before the metal nano-particle functionalization. This might be another reason for very small amount of capacitance change for Pd NP decorated device.

From the bode plot of Pd NP device for NH_3 concentration variation, the 3-dB cut-off frequency (f_C) has been extracted. 3-dB cut-off frequency is the frequency when the phase shift is -45^o and the impedance value drops to 0.707 of its initial value. Position of f_C for each impedance spectrum is shown in the Fig. 5.14 (a). In addition, from the visual inspection of the bode plot, the device response can be described as a low pass filter where number of dominant pole is one. From the fitted equivalent circuit elements, the theoretical 3-dB cut-off frequency can be calculated and compared with the experimental one. The expression for 3-dB cut-off frequency (f_C) for a low pass filter can be obtained by equating the real and imaginary part of the total impedance. Using equation 5.7 and 5.8 and after simplification, f_C for the diode at each exposure condition has been calculated and compared with the experimentally obtained one which is shown in Fig. 5.14 (b). The slight difference between the experimental and calculated ones are originating from the simplification of the expression for f_C. Maximum disparity was obtained for f_C values in air which is only 10%, this substantiates the validity of the equivalent circuit model and fitting to the experimental results. Analyzing the impedance spectra provides a number of parameters to utilize in multimodal sensing paradigm. Extracted junction resistance, capacitance and experimental cut-off frequency is plotted in the 3-D format (Fig 5.15) showing almost linear variation with NH_3 concentration.

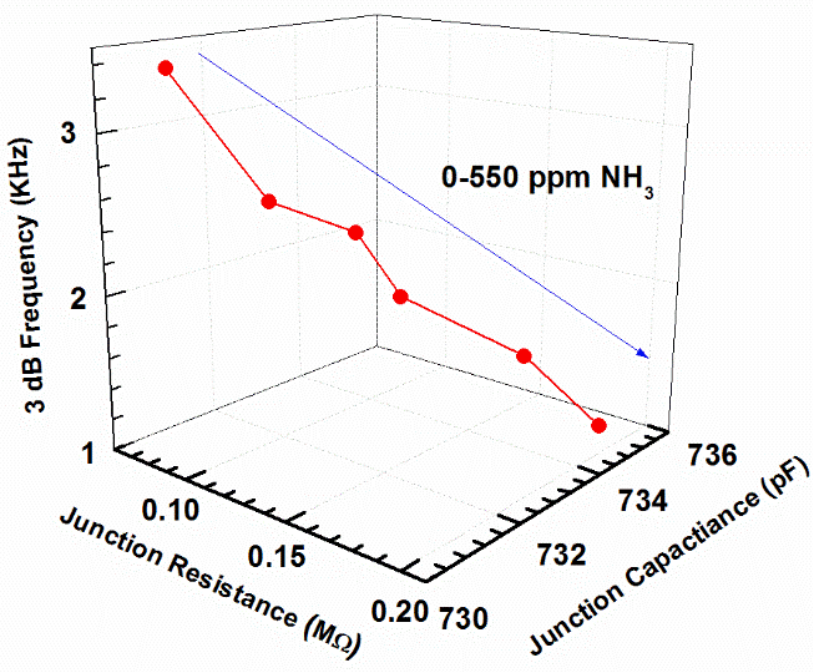

Figure 5.15 3D plot showing the variation of junction resistance and capacitance (extracted from the circuit model fitting) and 3-dB cut-off frequency with NH_3 concentration variation

Selective sensing is a very important performance factor for any sensor to be practically usable in real life, otherwise, false alarm is a big disadvantage which would overshadow other benefits. For that, we circuit simulated and compared the response of the sensor with Pd NP for NO_2, NH_3 and H_2 exposure as shown in Fig 5.16 (a). The dotted and solid lines in Fig 5.16 (a) are the experimental and equivalent circuit model fitting for all three gas exposure condition. Extracted junction resistance, capacitance and cut-off frequency is plotted in 3-D format [Fig 5.16 (b)] as before. From the relative data position and the slope of NH_3 concentration dependent response, it can be concluded that with the variation in concentration for NO_2 and H_2, and relevant slope change, unique signature for each gas might be obtained. Although similar results has been observed for reduced graphene oxide based vapor senor previously [15], graphene/p-Si diode sensor exhibited

much higher sensitivity which might lead to wider dynamic range along with CMOS compatibility and low power consumption.

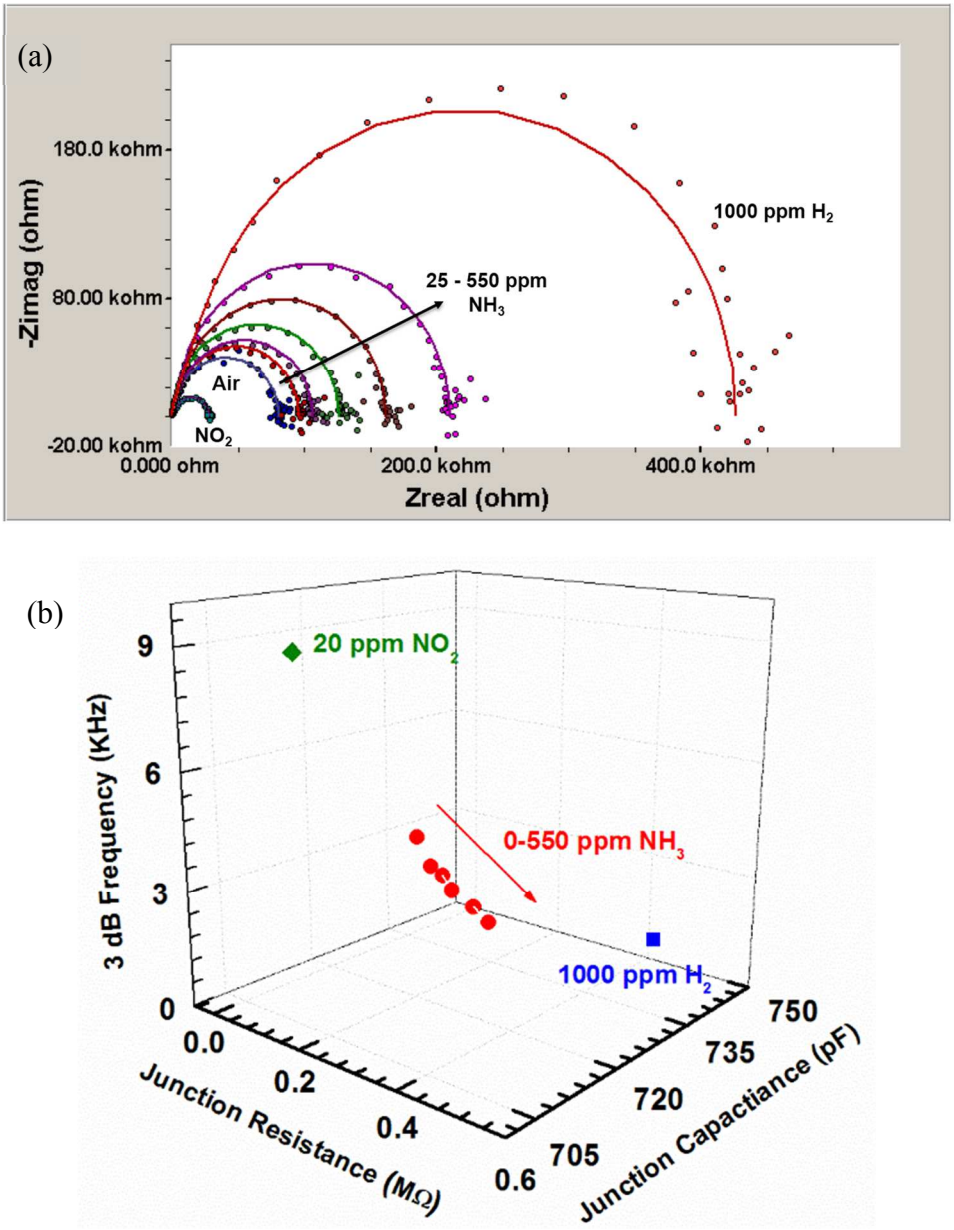

Figure 5.16 (a) Circuit model fitting to NO_2, NH_3, H_2 response for Pd-Graphene/p-Si. (Dotted lines are experimental results and solid lines are from circuit model fitting), and (b) 3D plot showing the variation of junction resistance and capacitance (extracted from the circuit model fitting) and 3-dB cut-off frequency at different condition.

CHAPTER 6

EFFECT OF METAL HYDRIDE SURFACE FUNCTIONALIZATION ON GRAPHENE: A HALL MEASUREMENT STUDY

6.1 Introduction

Due to its two dimensional (2D) nature, charge carriers in graphene are confined within one atomic layer thickness and its properties are easily influenced by the surrounding medium. Influenced properties due to surface effect can include electrical, chemical, optical, mechanical, etc. Over the last decade graphene came up as an exciting material due to its high mobility, carrier velocity, ultimate possible carrier confinement, electrical, optical and chemically tunable work function, high young's modules, optically transparent, etc. [1, 2]. In addition to excellent material properties, ability to form layered heterostructure with other lower dimensional materials, where the interface properties such as barrier height can be modulated, opens up a myriad of possible device and sensing applications. Since graphene properties can be easily influenced by surrounding medium, engineering its surface adds new functionality and is very attractive for device and sensing applications. Metal nano-particle (NP) functionalization of graphene is one such technique to not only change the doping but also facilitate sensing of analytes to which pristine graphene does not respond. In addition to chemical sensing [3], metal nano-particle can

impart lots of other novel functionalities such as tuning device characteristics [4, 5], enhancing optical sensitivity [6], etc. Noble metal NP functionalization of 2D material attracted significant research interest recently for enhancing polar molecule sensitivity [7], facilitating nonpolar molecule such as H_2 sensing [3], acting as dopants [4,5], etc. Although in all the amperometric sensing mechanism involves change in current transport, there has not been any study on change in electrical properties such as mobility for analytes such as H_2 exposure. Understanding the effect of NP functionalization on these properties would pave the path for enabling efficient sensing as well as new applications. In this work, temperature dependent electrical transport study of CVD graphene in Hall geometry has been carried out at different conditions: as fabricated, after Pd NP deposition and with H_2 exposure after NP decoration. Hall measurement of single layer graphene showed increase in mobility with decrease in temperature, which implies that substrate surface optical phonon scattering is the dominant scattering mechanism [8]. For bilayer graphene, Hall mobility increases with temperature in the range of 10 - 298 K, indicating that Coulomb scattering is the most important scattering mechanism [8]. Mobility showed different trend after 2 nm Pd NP deposition by electron beam evaporation. However, with H_2 exposure, Hall mobility of the Pd-functionalized graphene enhances significantly and the dominant scattering mechanism switches to thermal excited substrate optical phonon scattering.

6.2 Hall Effect

Mobility is the measure of how fast a charge carrier can move in an applied electric field and measured by different techniques. One such technique is Hall measurement where the Hall Effect describes the behavior of the free carriers in a semiconductor when applying an electric as well as a magnetic field perpendicular to each other. The experimental setup

for Hall measurement is shown in Figure 6.1, depicts for (a) p-type and (b) n-type uniformly doped semiconductor bar with a rectangular cross section and length L. An electric field is created along the x-direction by applying the voltage V_x between the two opposite side contacts and the magnetic field is applied in the z direction.

As shown in Figure 6.1 (a), the holes move in the same direction of the applied electric field. The magnetic field causes a force on the accelerated charge carriers in a direction dictated by the right hand rule. The resulting force along the *y*-direction F_y deflects the holes from its original moving path along the x-direction to the right direction. However, in steady state the force, F_y is balanced by an electric field, E_y, so that there is no net force on the holes and the whole process develops the Hall voltage, V_H across the

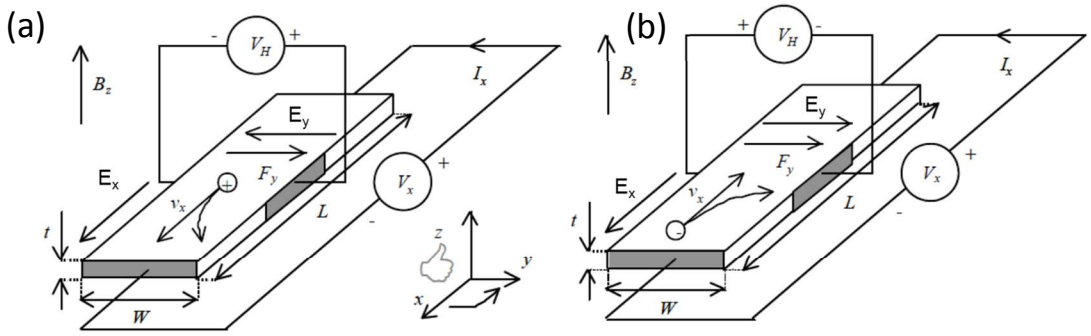

Figure 6.1 Hall Effect as shown schematically for (a) p-type (majority carrier hole) and (b) n-type (majority carrier electron) uniformly doped semiconductor [9]

sample in y-direction. In regularly used sign convention as shown in Figure 6.1(a), the hall voltage is positive for holes, and negative for electrons is shown in Figure 6.1(b) [9].

For the formulation of the Hall field, one can consider the Lorentz force acting on the charge carriers:

$$\bar{F} = q(\bar{E} + \bar{v} \times \bar{B})$$

Considering the applied voltage along x-direction, initially the carriers are flowing along the *x*-direction with a velocity of v_x. The Lorentz force can be given by:

$$\bar{F} = q\bar{E} + \begin{bmatrix} \overline{e_x} & \overline{e_y} & \overline{e_z} \\ v_x & 0 & 0 \\ 0 & 0 & B_z \end{bmatrix} = qE_x\overline{e_x} + q\left(E_y - v_xB_z\right)\overline{e_y} + qE_z\overline{e_z}$$

Due to the flow of carriers only along the x-direction, the y and z component of the force must be zero. Equating the y-component of force to zero yield the relationship between applied magnetic field and the electric field along the *y*-direction,

$$F_y = q\left(E_y - v_xB_z\right) = 0$$

The y-component of electric field can also be rewritten as a function of the current density (J_x) using its relationship with carrier velocity, $J_x = qpv_x$

$$E_y = v_xB_z = \frac{J_x}{qp}B_z$$

This electric field along y-direction is called the Hall field. The Hall coefficient, R_H, is defined as the Hall field divided by the applied current density and magnetic field:

$$R_H = \frac{E_y}{J_xB_z} = \frac{1}{qp}$$

The Hall coefficient can be calculated from the measured current, I_x, and measured voltage, V_H:

$$R_H = \frac{V_H}{I_xB_z}\frac{tL}{W} \qquad (6.1)$$

The hole density can be given by,

$$\Rightarrow p = \frac{1}{qR_H} = \frac{J_xB_z}{qE_y} \qquad (6.2)$$

The carrier mobility can also be extracted from the Hall coefficient and semiconductor resistivity (ρ):

$$\mu = \frac{J_x}{qpE_x} = \frac{R_H}{\rho} \qquad (6.3)$$

From the sign of the Hall voltage, the type of semiconductor (*n*-type or *p*-type) and mobility can be determined easily. Temperature dependent mobility measurement provides wealth of information including the scattering mechanism, effect of substrate and surrounding dielectric medium, etc.

6.3 Fabrication of Hall Bar and Measurement Set-up

Graphene was synthesized by chemical vapor deposition (CVD) on Cu foil and subsequently transferred on SiO_2/Si substrate by PMMA (Poly-methyl methacrylate) assisted wet transfer method. Details of growth and transfer is discussed in chapter 2. The difference in fabrication of Hall pattern is that, the SiO_2/Si substrate had Ti/Au contact before graphene transfer to avoid processing induced damage of graphene as much as possible. For that 300 nm SiO_2/Si substrate was lithographically patterned and 10/80 nm Ti/Au was deposited by electron beam evaporation method at a base pressure of 10^{-6} Torr for metal contact. After graphene transfer on the as-prepared substrate, the PMMA supporting layer was not dissolved to prevent contamination from the subsequent photolithography step. Afterwards another round of photolithography was done to define the active graphene area for Hall measurement study. Next, unwanted graphene with PMMA was etched by O_2 plasma in RIE chamber. Finally photoresist and PMMA were dissolved in Acetone and Methanol. Complete transfer and fabrication process is shown in Figure 6.2 along with the optical image of graphene Hall pattern (20 μm channel width) in the bottom. Measurement of both small and large area devices were carried out initially but for PdHx study only large area devices have been used to avoid process induced damage as much as possible. After initial material and electrical characterization, 2 nm Pd was

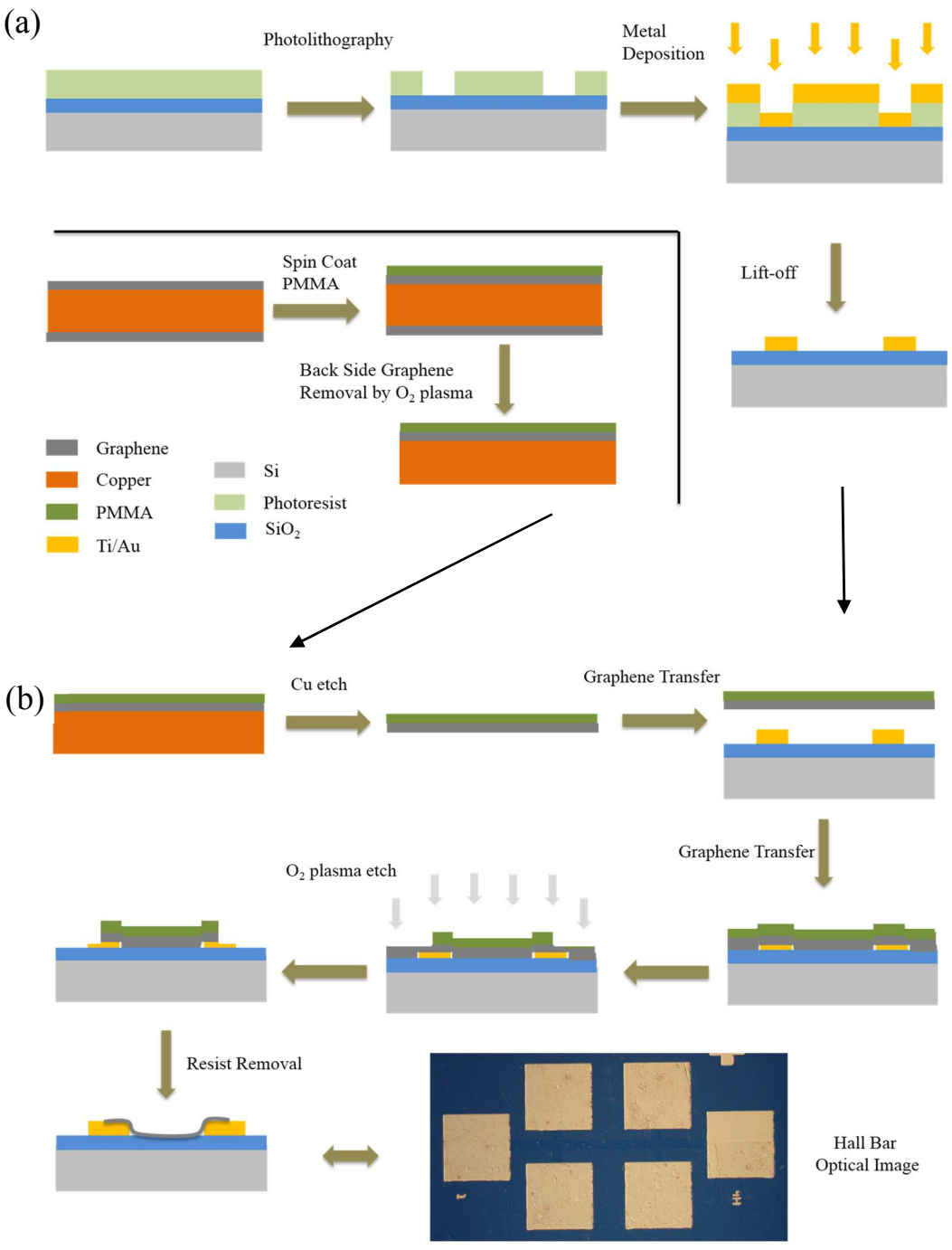

Figure 6.2 Device Fabrication steps (a) Metallization of SiO_2/Si and graphene pre-transfer steps, (b) Graphene transfer, devices processing and optical Image of fabricated Hall bar.

deposited by electron beam evaporation method at a base pressure of 10^{-6} Torr. For Pd NP deposition, shadow mask was used by covering the sample completely except the channel

region. For easy shadow masking, active graphene channel of the Hall pattern is kept in the range of several hundred micrometer.

6.4 Results and Discussion

Raman spectra for single layer graphene is shown again here in Fig 6.3(a) to compare with

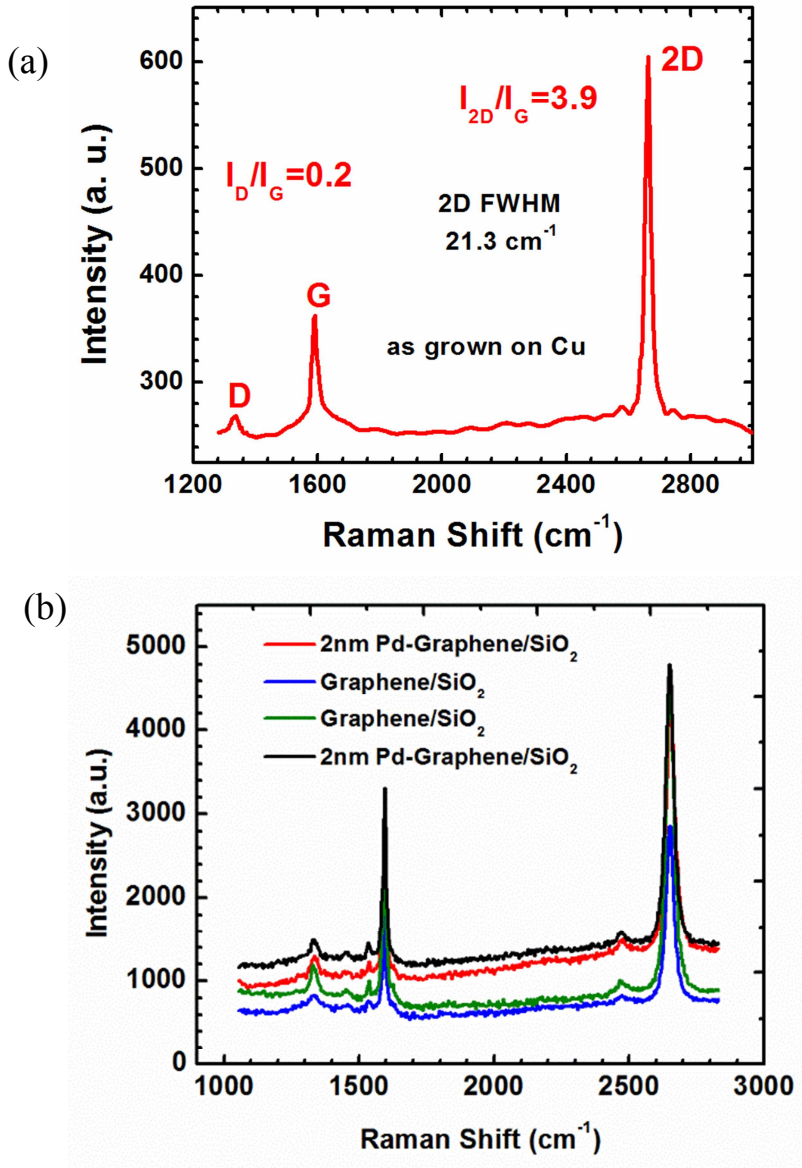

Figure 6.3 Raman spectra of (a) single layer graphene, and (b) bilayer graphene on SiO_2/Si before and after 2 nm Pd deposition.

bilayer graphene. Figure 6.3(b) is showing the Raman spectra of pristine and functionalized

bilayer graphene at two different positions. Initial D/G peak intensity ratio is around 0.1 which does not show significant change after Pd NP deposition, which is different from that of graphene on Si substrate discussed in chapter 4. Graphene on Si showed increase in D/G ratio after Pt/Pd deposition, which is most likely originating from the surface roughness of Si due to SiO_2 removal by buffered HF wet etching. However, here no significant change in D/G ratio and peak position confirm that no degradation or other structural change happened after Pd NP functionalization of graphene on SiO_2 substrate.

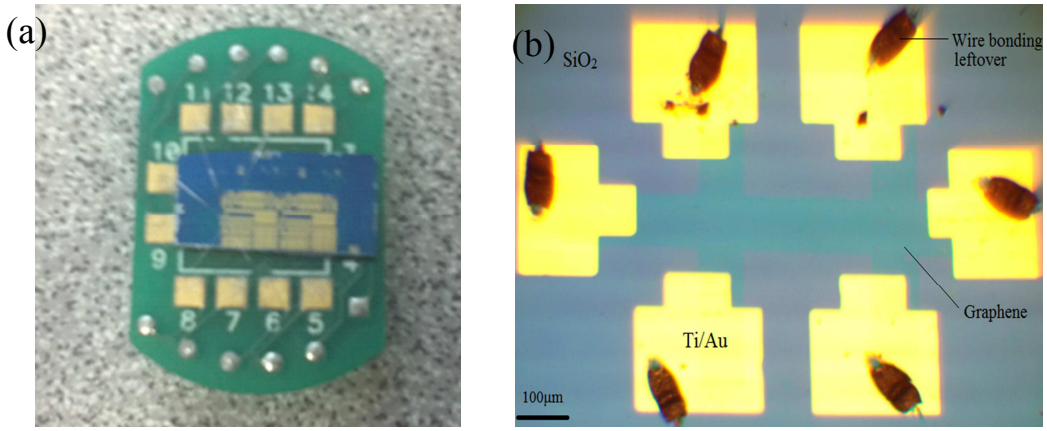

Figure 6.4 (a) Wire bonded sample with small area device on Hall sample holder. (b) Large area graphene Hall bar with bonding marks on the metal pad.

2D/G ratio of 1.65 and 2D peak full width half maximum (FWSM) of ~34 cm^{-1} indicates the presence of bilayer graphene [10] in the sample for which Raman spectra is shown in Fig 6.3(b).

For temperature dependent Hall measurement, devices were wire bonded as shown in Fig. 4(a) on the sample holder. This particular sample has small area devices and wire bonding for both large and small area device is similar. Fig. 4(b) is showing representative image of large area Hall pattern with wire bonding marks on the metal pads and graphene

channel is visible in the middle. Typical four-terminal method is used in our measurement, and the electrical connections for the measurement of resistance and mobility are shown schematically in Fig. 6.5(a) and applied magnetic field is perpendicular to the sample surface. The Physical Property Measurement System (Model 6000) is shown in Fig. 6.5(b).

(a)

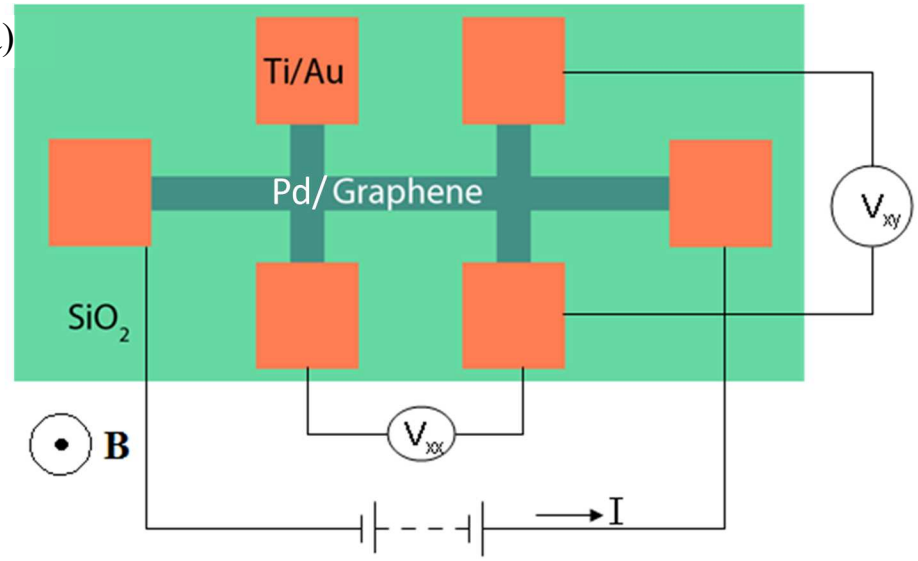

(b)

Figure 6.5 (a) Electrical connections for Hall measurement and the applied magnetic field. (b) The Physical Property Measurement System (Model 6000)

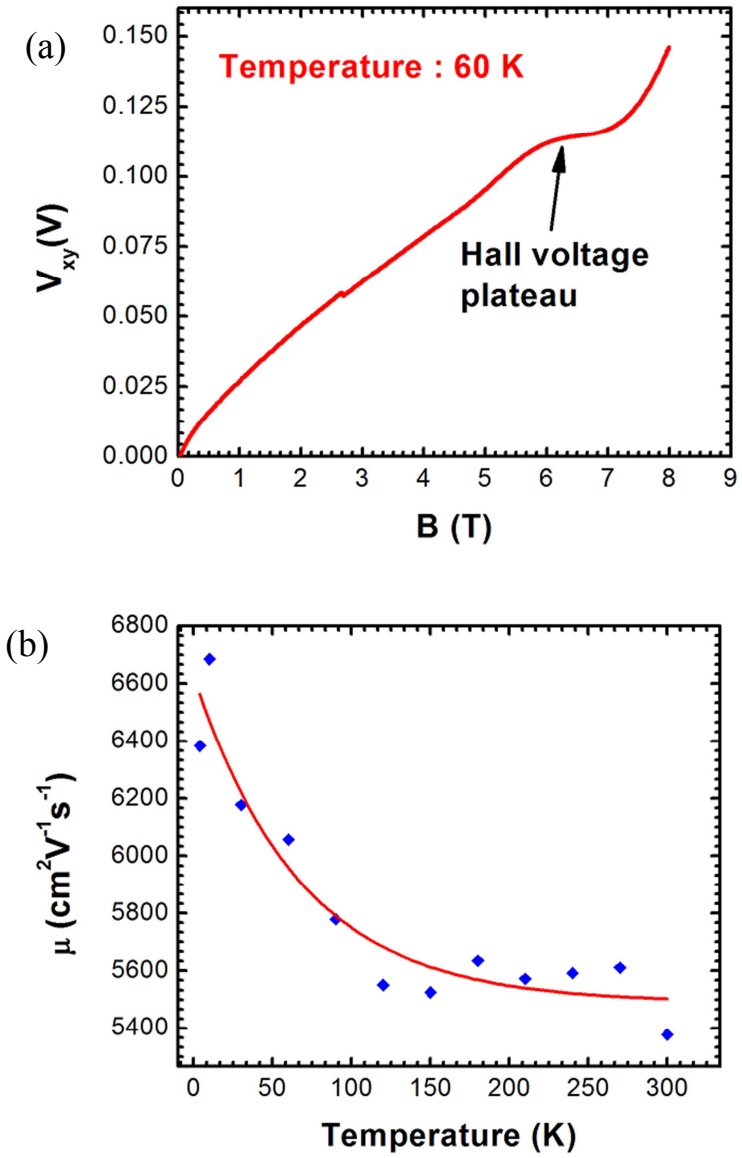

Figure 6.6 (a) Quantum Hall effect is visible from the plateau of Hall voltage V_{xy} at T = 60 K from monolayer graphene sample. (b) Temperature dependence of Hall mobility μ (blue rectangles) from the same sample. The red line is obtained from fitting equation 6.5.

A constant dc current was applied through the devices and the voltages V_{xx} and V_{xy} were measured across the terminals with the magnetic field B varied up to 8 Tesla in perpendicular direction. Out of the devices measured, majority showed the usual Hall Effect, where the Hall Voltage kept increasing with the magnetic field. However, for one

single layer graphene device, Hall voltage V_{xy} showed a plateau such as in the quantum hall effect when it is cooled down to 60 K, as shown in Figure 6.6(a). The value of the plateau fits in equation 6.4 with n = 5, where n is the Landau-level index and I is the current.

$$V_{xy} = {Ih}/{(4n + 2)e^2} \qquad (6.4)$$

The charge carrier densities and charge carrier mobility values were extracted from the hall measurement. The charge carrier density of p ~10^{12} cm^{-2} and mobility at room temperature of μ ~ 2000 cm^2/Vs were found for most of the devices. However, the device which showed the quantum hall effect had the mobility as high as 5400 cm^2/Vs at room temperature and 6600 cm^2/Vs at l0 K, as shown in Figure 6.6(b). The temperature dependence of carrier mobility μ can be expressed by the following equation:

$$\mu = A \times T^B \qquad (6.5)$$

Where A and B are the fitting parameters.

Figure 6.7 is showing the temperature dependent mobility for bilayer graphene exhibiting opposite trend compared to monolayer graphene. The mobility reduced from 2405 cm^2/Vs at room temperature to 2368 cm^2/Vs at 60 K. The different trends in the variation in the carrier mobility in monolayer and bilayer graphene can be explained by differences in their density-of-states and the additional screening of substrate surface polar phonon induced electrical field in bilayer graphene. The mobility in monolayer graphene decreases rapidly with increasing temperature is primarily due to scattering by thermally excited surface polar phonons of the SiO_2 substrate [8, 11-13]. The SiO_2 optical phonons at the substrate/graphene interface modulate the polarizability, which produces an electric field that couples to the moving charge carriers in graphene. The coupling in terms of the effect of electric field depends exponentially on the substrate graphene distance. At the Van der

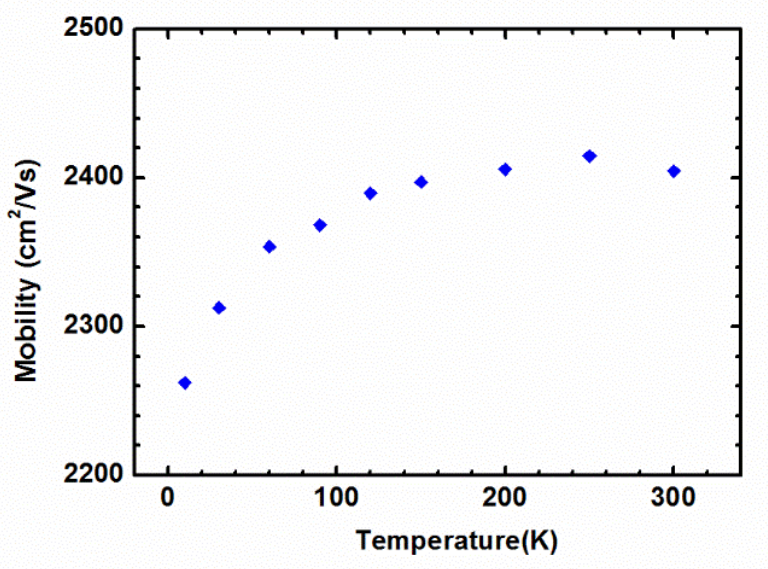

Figure 6.7 Temperature dependent mobility of bilayer graphene

Waals distance of about 0.35 nm, it is much stronger than the coupling of the carriers to the acoustic phonons of graphene becoming the dominant scattering mechanism. Since, the substrate surface polar phonon scattering is proportional to the phonon population number, as the temperature is increased, the mobility is expected to decrease drastically. As observed for bilayer graphene, the mobility increases instead of decreasing as the temperature increases. This is due to the fact that the substrate surface polar phonon induced field is to some extent screened by the additional graphene layer and Coulomb scattering is the dominant for these bilayer graphene devices [8, 14, 15]. Due to the parabolic band structure in bilayer graphene, the energy averaging of the Coulomb

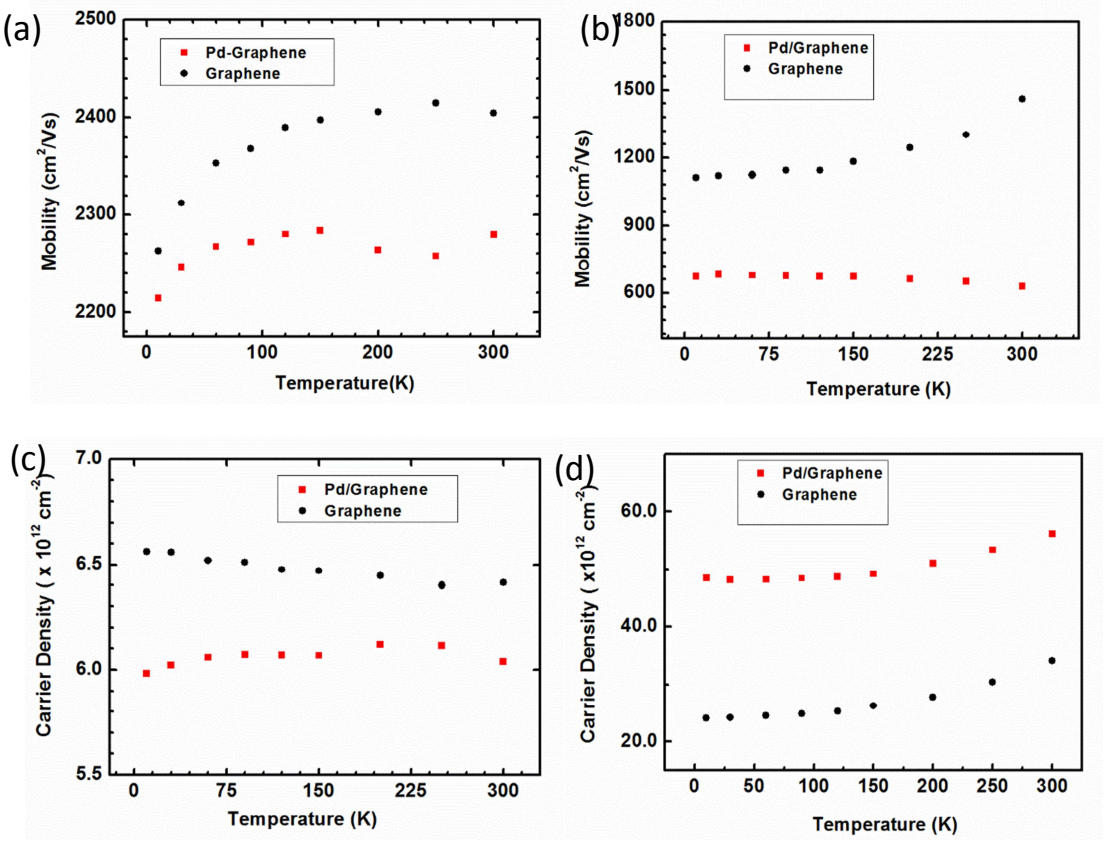

Figure 6.8 Temperature dependent mobility of bilayer graphene before and after 2 nm Pd deposition (a) Sample A and (b) Sample B, and Carrier Density (c) Sample A and (d) Sample B.

scattering time can result in the mobility increasing proportionally with temperature $\mu \propto k_B T$ [16].

Effect of short range and acoustic phonon scattering do not vary with temperature due to the reasons discussed here briefly. Since the density of states and the screening function are energy independent for bilayer graphene, mobility limited by short-range scattering is independent of temperature. In monolayer graphene, when $k_B T \ll E_F$, the temperature dependence of conductivity and hence mobility that is limited by short range scattering is nearly constant [17]. On the other hand, the mobility limited by acoustic phonons in monolayer graphene is inversely proportional to temperature [18]. However,

since the magnitude of the mobility limited by graphene phonon scattering is of the order of 10^5 cm^2/Vs, [19,20] i.e., much larger than the mobilities limited by the Coulomb and short-range scattering mechanisms discussed here, effect of acoustic phonon can be neglected for bilayer graphene.

Fig. 6.8 is showing the effect of 2 nm Pd deposition on graphene, change in mobility and carrier concentration for 2 samples. In both the samples mobility reduced, however in sample A [Fig. 6.8(a)] mobility reduction is much less compared to Sample B [Fig. 6.8(b)]. Room temperature reduction in mobility for sample A is from 2405 to 2279 cm^2/Vs compared to significant reduction of 1460 to 630 cm^2/Vs for sample B. From the Raman spectroscopy of sample B before and after Pd deposition, no significant enchantment of D/G ratio has been observed as shown in Fig. 6.3. With Pd NP, mobility in Sample A followed the previous trend, with minor exception over the temperature range of 250 to 200 K [Fig. 6.8(a)], which is small considering the overall measurement temperature range. However, mobility in sample B increased from 630 to 672 cm^2/Vs as temperature decreased, amounts only to ~6% change which is also within the experimental error of the measurement. From the previous discussion, it can be assumed that, Pd NP effects the temperature dependent mobility in such a way that coulomb scattering is no longer the dominant scattering mechanism for sample B. To probe further carrier density variation at different temperature for both the samples are plotted in Fig. 6.8 (c) and (d). Surprisingly the Pd NP induced doping is opposite for the two samples. For sample A, room temperature hole density decreased from 6.4×10^{12} to 6.04×10^{12} cm^{-2} and for sample B, increased from 3.4×10^{13} to 5.6×10^{13} cm^{-2}, indicating n-type doping for the former and p-type

doping for the later. Considering the higher work function of Pd compared to graphene, the p doping can be easily explained.

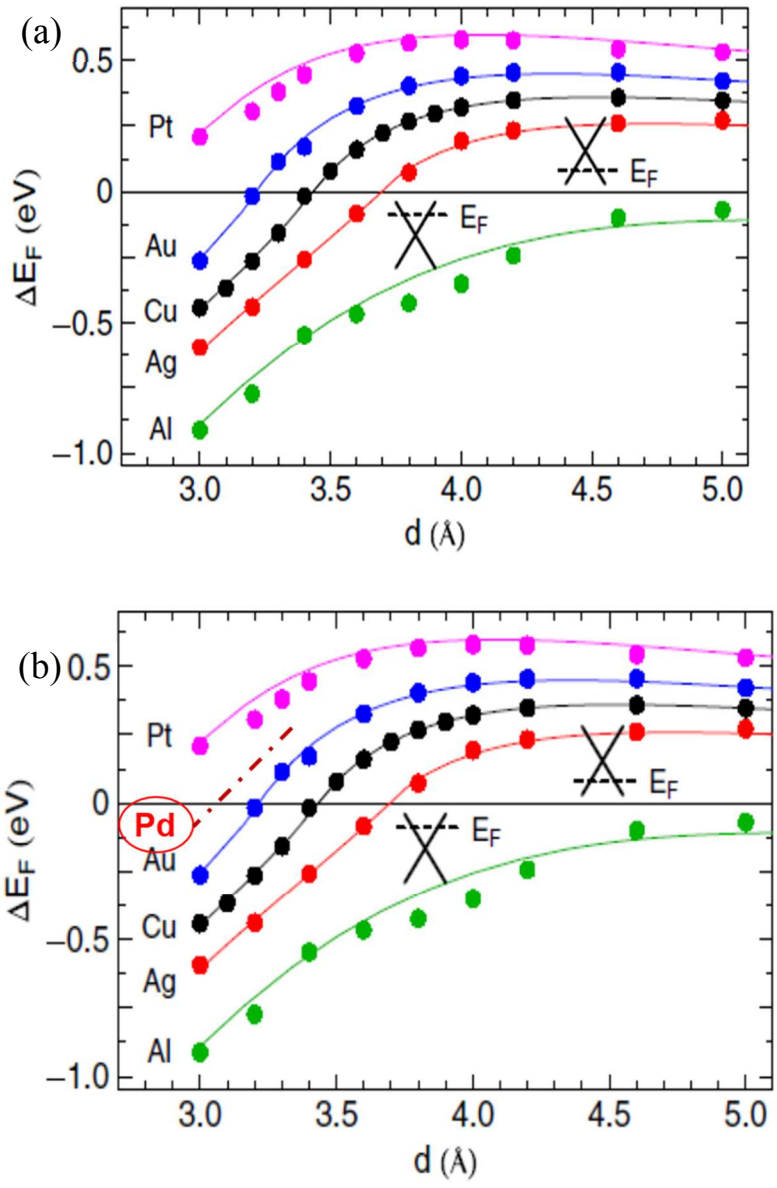

Figure 6.9 (a) Fermi level shifts $\Delta E_F(d)$ as a function of the graphene-metal surface distance d. The dotted lines are obtained numerically from first-principles calculations based on density functional theory and the solid lines give the results obtained from analytical Model [21]. (b) Predicted position is shown by the dashed line for Pd NP in between Pt and Au to explain the results obtained in this study for Pd NP induced doping of bilayer graphene.

To explain the n-type doping, one possible way is to apply the numerical and analytical model developed by Giovannetti et al. [21] for interaction between graphene and metal, such as Al, Ag, Cu, Au, and Pt which forms weak bonding with graphene while preserving its electronic structure. Although graphene electronic structure can be significantly altered by Pd (111), in our case, its thickness is 2 nm which does not form a continuous layer (forms grains of 20-30 nm as seen in SEM image in chapter 4) and any noticeable change has not been observed in Raman spectra shown in Fig. 6.3, the mentioned model can be employed for Pd NP as well. Both from numerical and analytical model in reference 21, nature of charge transfer depends on the separation distance between graphene and metal. Hence, the charge redistribution at the graphene-metal interface is not only the result of an electron transfer between the metal and the graphene levels originated from the difference in work function. There is also a contribution from the metal graphene chemical interaction. Graphene work function is preserved to its freestanding value of 4.5 eV only when graphene-metal distance is greater than 4.2 Å, the potential due to metal graphene chemical interaction is very small and charge transfer depends only on the work function. For smaller distance, chemical interaction induced potential becomes significant which increases the effective graphene work function (W_G) significantly, as for example, at the equilibrium distance of 3.3 Å, theoretically obtained W_G is 5.4 eV much higher than its freestanding value. Defining metal work function as W_M and $\Delta V(d)$ as the potential change generated by the metal-graphene chemical interaction, Fermi level shift in graphene, $\Delta E_F(d)$ as a function of the graphene-metal surface distance (d) can be given by the following equation,

$$\Delta E_F(d) = W_M - \Delta V(d) - W_G \qquad (6.5)$$

Fermi level shift, $\Delta E_F(d)$ as a function of the graphene-metal surface distance (d) for different weakly interacting metal is shown in Figure 6.9(a) where only for Pt which has highest work function, ΔE_F is positive for all d and resultant doping in graphene is always p-type. Considering the opposite doping for sample A and B, Pd NP work function in this work is smaller than Pt, and the trend for Pd might be in between Pt and Au as shown in Figure 6.9(b). For very small interaction distance d between Pd NP and graphene, ΔE_F might be negative and resultant doping is n-type, reducing the p-doing of CVD

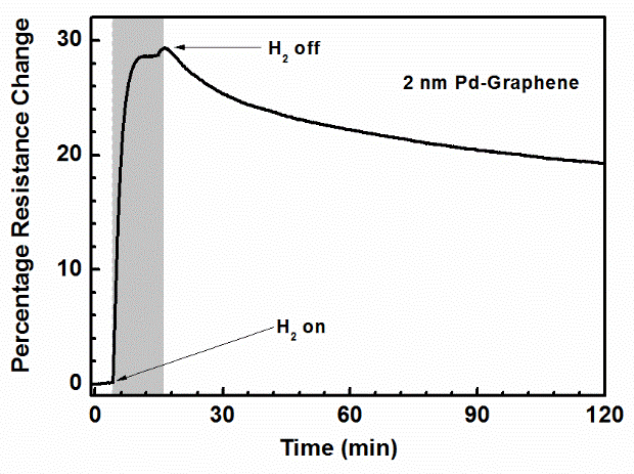

Figure 6.10 Effect of H_2 exposure on the resistance of graphene channel in Hall Bar

graphene which has happened for sample A.

The change in resistance of Pd NP functionalized graphene Sample A for H_2 exposure is shown in Fig 6.10 as a function of time, which completely agrees with the increase in resistance as shown in chapter 3 and chapter 5 for chemiresistor sensor. Here the recovery is slow due to only N_2 exposure instead of air which contains O_2 and helps fast recovery.

Temperature dependent Hall mobility for Sample A is shown in Fig 6.11(a) for H_2 exposure from the temperature range of 300 to 10 K. At room temperature, Hall mobility increased from 2279 to 3840 cm^2/Vs after H_2 exposure. This can be explained by the formation of PdH_x which has higher resistivity compared to metallic Pd [22] and the high dielectric constant of PdH_x [23]. Pd was also deposited on SiO_2/Si at the time of 2 nm Pd

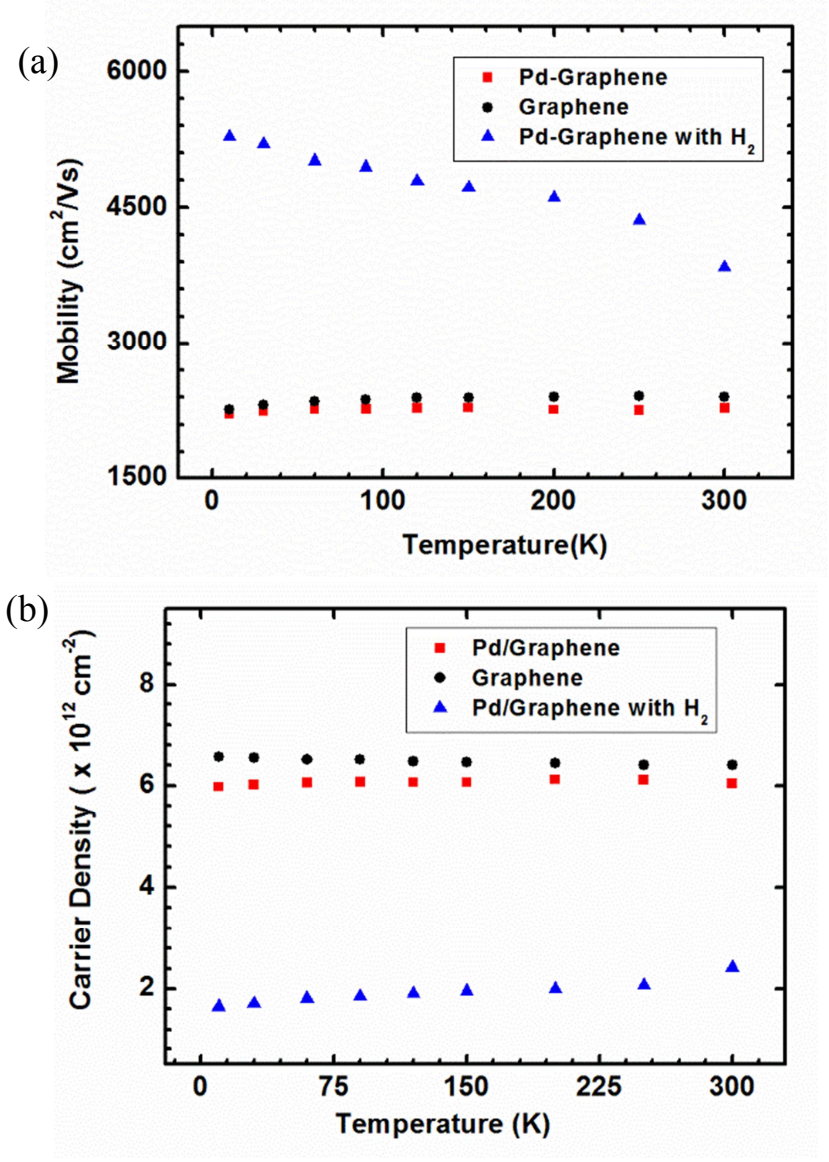

Figure 6.11 Effect of H_2 exposure on (a) mobility and (b) carrier concentration for sample A over the temperature range of 300 to 10 K.

deposition on graphene, and the measured resistance of Pd was in MΩ range. Hence, PdH_x resistance increased to a higher value after H_2 exposure becoming almost insulating. PdH_x is also reducing the carrier concentration of graphene from 6.04×10^{12} to 1.65×10^{12} cm^{-2} as seen in Fig 6.11(b). The mechanism responsible for this reduction has been already described in section 5.2. In addition to reducing the carrier concentration, it has high dielectric constant compared to both Pd and air. Together decrease in carrier

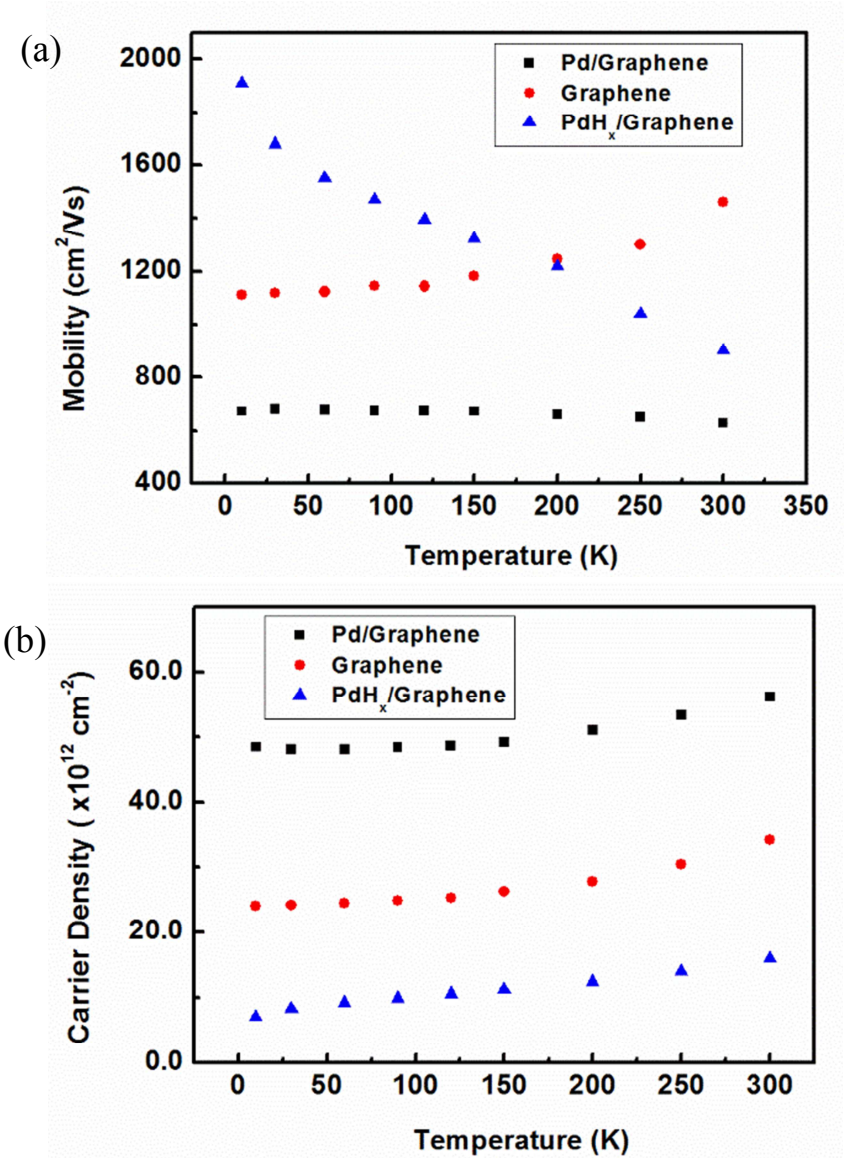

Figure 6.12 Effect of H_2 exposure on (a) mobility and (b) carrier concentration for sample B over the temperature range of 300 to 10 K.

concentration and dielectric screening induced reduction in coulomb scattering greatly enhances the mobility [24]. This is also evident from the temperature dependence of the mobility which increased up to 5278 cm^2/Vs at 10 K [Fig 6.12(a)]. Room temperature mobility increase with H_2 exposure has also been observed for other semiconducting nanostructure such as InAs [26].

Another important point to note regarding the temperature dependence of the mobility for H_2 exposure, mobility increases with the decrease in temperature, which is completely opposite without H_2 exposure. Similar trend has been observed for monolayer graphene, which originates when surface phonon scattering is the dominant mechanism influencing the electrical transport. The nature of temperature dependent Hall mobility of Pd NP-graphene after H_2 exposure completely matches with the effect of high K dielectric as predicted both theoretically [24] and experimentally [25]. Similar nature has been observed for Sample B as well, room temperature mobility increased from 630 to 900 cm^2/Vs with H_2 exposure, which further increased to 1910 cm^2/Vs at 10 K as shown in Fig 6.12 (a). Similarly, the carrier density reduced 5.6×10^{13} to 1.59×10^{13} cm^{-2} at room temperature and further down to $7.09 \times 10^{12} cm^{-2}$ at 10 K. The carrier concentration dependence of mobility can also described by the relationship between these two parameters,

$$\mu(n) \sim n^{-\alpha} \qquad (6.6)$$

Where the value of exponent, α lies between 0.3-0.4 [27]. However, high K dielectric screens the coulomb scattering and tends to increase the mobility which is then partially or completely suppressed by the surface optical phonon scattering from the dielectric itself [27]. As discussed before PdH_x forms a dipole where its negatively charged part is at the

interface with graphene, reduces its majority positive charge carrier density. The electric field from the dipole most likely influences the moving charge carriers in a similar way to that of a polar dielectric with large dielectric constant, where the optical phonon couples with the carriers in the channel and results in scattering which tries to offset the mobility enhancement due to dielectric screening induced reduction in coulomb scattering. Hence, this might be the reason for the change from coulomb to optical phonon scattering dominated Hall mobility variation with temperature for H_2 exposure condition.

Due to these two opposite condition of high dielectric constant to reduce coulomb scattering and high SO phonon frequency to reduce surface optical phonon scattering, we need a substrate which can satisfy both the conditions. In addition, Coulomb and short-range scattering limited mobility for bilayer graphene is inversely proportional to the square of the effective mass. Thus, as the number of graphene layer increases, the effective mass becomes heavier, leading to a higher degradation of the mobility limited by Coulomb and short-range scattering for the same impurity concentration. Hence, to improve the transport properties including mobility in multilayer graphene, it is imperative to reduce the impurity concentration either by process optimization or substrate/dielectric engineering.

Finally, back gated measurements of bilayer graphene device fabricated next to the Hall bar on sample B have been carried out at three different conditions. Initially mobility of graphene was 1735 cm^2/Vs and current minima point is close to 40 V. After 2 nm Pd deposition mobility reduced to 652 cm^2/Vs and from the almost linear nature of current decrease, it can be estimated that, Dirac point shifted to higher positive voltage. This higher Dirac voltage compared to that of before Pd deposition indicates that Pd NP increased

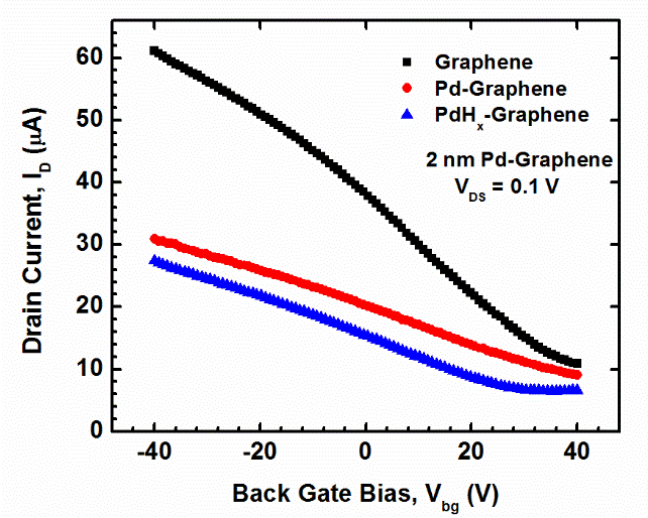

Figure 6.13 Back Gated transfer characteristics of bilayer graphene at three different conditions.

graphene's p-type doping resulting in higher residual carrier concentration. After H_2 exposure although the Dirac point shifted towards left mobility didn't show significant increase. Dirac point shift towards lower positive voltage means PdH_x reduced hole concentration in graphene. With the decrease in carrier concentration, little improvement in mobility has been observed as visible from the slightly higher slope of the blue line. It can be assumed that, coulomb scattering reduced after H_2 exposure, however, PdH_x dipole induced scattering shadowed that advantage at least in room temperature. From the Hall mobility variation with temperature, we can expect that, filed effect mobility with H_2 exposure would also increase at low temperature.

Considering the findings and discussion in chapter 4 on hBN which reduces the residual charge concentration in graphene eliminating the requirement of high dielectric constant and simultaneously have high optical phonon frequency close to that of graphene appeared as better substrate for graphene devices for applications ranging from electronics to sensing including H_2 sensor. Graphene on hBN has high mobility and hence expected to

increase the sensitivity. The improvement in Hall mobility for epitaxial graphene with CVD grown hBN top dielectric compared to HfO_2 [28,29] also supports this proposition.

CHAPTER 7

CONCLUSIONS AND FUTURE DIRECTIONS

This dissertation research started with development of CVD graphene based device fabrication process while improving the quality of graphene growth. After successful fabrication of graphene back gated field effect transistor on SiO_2/Si substrate, later electrical transport properties has been improved on PLD deposited BN. In a parallel effort, to improve the performance of graphene based sensor, reverse bias operation of graphene/Si Schottky diode based sensor with metal nanoparticle functionalization has been proposed. The diode sensor AC impedance spectra has been analyzed with electrical equivalent circuit model and multimodal sensing method is demonstrated. Finally, from the temperature dependent magneto-transport studies of Pd functionalized bilayer graphene, Hall mobility enhancement has been observed for H_2 exposure. The future possibilities for the above mentioned research projects are discussed in the following sections.

From Raman spectra of graphene on BN with four different thickness, as shown in Fig 7.1, both G and 2D peak position and width is varying with BN thickness. hBN peak ~1365 cm^{-1} is also clearly visible in Fig 7.1(a) which most of the time shadowed by graphene D peak. Presence of hBN peak and variation in graphene peaks with hBN thickness, compels a comprehensive study on the effect of hBN layer thickness on graphene electronic spectrum such as charge transfer between these two materials,

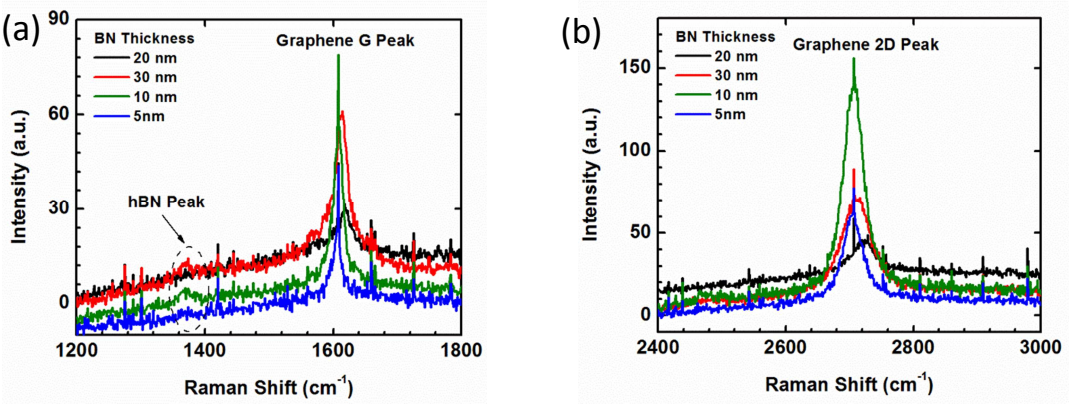

Figure 7.1 Variation of Raman characteristic peaks of graphene with different hBN thickness (a) Graphene G peak position and width, and (b) Graphene 2D peak full width half maximum (FWHM) and position.

modification of graphene secondary Dirac points by hBN potential, etc. Incorporating the charge transfer effect with graphene electrical characteristics would provide opportunities to improve the device performance and new applications. One such opportunity arises when graphene electronic spectrum gets modified by differences between the crystal lattices of graphene and BN. The periodic perturbation originating from the difference between their lattice constants and crystallographic misalignment acts on graphene's charge carriers which results in the generation secondary Dirac points in electronic spectra. The possibility of creating gaps at specifically chosen energies by controllably rotating graphene or other two dimensional crystals can be used to design novel electronic and optoelectronic devices.

Also from the electrical characterization, it has been observed that impurity carrier concentration is much lower for graphene especially on 5 nm BN. However, from the forward and backward back gate sweep, hysteresis is visible which signifies the presence of slow trapped charge in BN. This trap characteristics need to be improved to achieve better device performance. For any transistor device, top gate dielectric is the essential

device component. Thus, PLD BN could be used as top gate dielectric to study the complete transport characteristics. For the development of hBN as a substrate and top dielectric, significant amount of studies are needed. For 2D material based multilayered device structure, hBN could be used as tunneling barrier as shown in Fig 7.2 [1], which would find applications in tunneling transistor, negative differential resistance based devices, etc.

Graphene based sensor development study performed in the present research work, can be extended to any other lower dimensional heterostructure based wide range of device

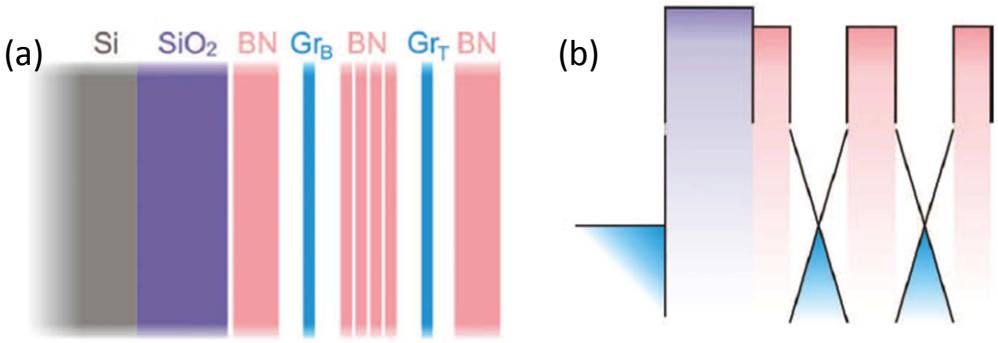

Figure 7.2 (a) Schematic structure of graphene field-effect tunneling transistor with two graphene layers sandwiched between BN layers. (b) The corresponding band structure with no gate voltage applied. [1]

paradigms such as Schottky diode, tunnel transistor, bipolar junction transistor, etc. for better sensitivity, selectivity, and sensing tunability. Impedance spectroscopy can be utilized further to analyze the response of different gases while varying the concentration. Extracted parameters obtained from dc amperometric measurement and impedance spectroscopy, multidimensional plot can be constructed which would be helpful as design space for selective sensing. Temperature dependent magneto-transport study can be further extended by varying the thickness of Pd, depositing other similar material such as Pt, and

comparison between the metals. These types of study can be carried out for other 2D materials such as MoS_2, WSe_2, etc.

REFERENCES

[*References are listed separately for each chapter*]

Chapter 1:

1. Novoselov, Kostya S., Andre K. Geim, S. V. Morozov, D. Jiang, Y. Zhang, S. V. Dubonos, I. V. Grigorieva, and A. A. Firsov. "Electric field effect in atomically thin carbon films." *science* 306, no. 5696 (2004): 666-669.
2. Bolotin, Kirill I., K. J. Sikes, Zd Jiang, M. Klima, G. Fudenberg, J. Hone, P. Kim, and H. L. Stormer. "Ultrahigh electron mobility in suspended graphene."*Solid State Communications* 146, no. 9 (2008): 351-355.
3. Baringhaus, Jens, Ming Ruan, Frederik Edler, Antonio Tejeda, Muriel Sicot, Amina Taleb-Ibrahimi, An-Ping Li et al. "Exceptional ballistic transport in epitaxial graphene nanoribbons." *Nature* 506, no. 7488 (2014): 349-354.
4. Balandin, Alexander A., Suchismita Ghosh, Wenzhong Bao, Irene Calizo, Desalegne Teweldebrhan, Feng Miao, and Chun Ning Lau. "Superior thermal conductivity of single-layer graphene." *Nano letters* 8, no. 3 (2008): 902-907.
5. Lee, Changgu, Xiaoding Wei, Jeffrey W. Kysar, and James Hone. "Measurement of the elastic properties and intrinsic strength of monolayer graphene." *science* 321, no. 5887 (2008): 385-388.
6. Nair, R. R., P. Blake, A. N. Grigorenko, K. S. Novoselov, T. J. Booth, T. Stauber, N. M. R. Peres, and A. K. Geim. "Fine structure constant defines visual transparency of graphene." *Science* 320, no. 5881 (2008): 1308-1308.
7. Yang, Heejun, Jinseong Heo, Seongjun Park, Hyun Jae Song, David H. Seo, Kyung-Eun Byun, Philip Kim, InKyeong Yoo, Hyun-Jong Chung, and Kinam Kim. "Graphene barristor, a triode device with a gate-controlled Schottky barrier." *Science* 336, no. 6085 (2012): 1140-1143.
8. Britnell, L., R. V. Gorbachev, R. Jalil, B. D. Belle, F. Schedin, A. Mishchenko, T. Georgiou et al. "Field-effect tunneling transistor based on vertical graphene heterostructures." *Science* 335, no. 6071 (2012): 947-950.
9. Lin, Yu-Ming, and Phaedon Avouris. "Strong suppression of electrical noise in bilayer graphene nanodevices." *Nano letters* 8, no. 8 (2008): 2119-2125.
10. Rumyantsev, S., G. Liu, W. Stillman, M. Shur, and A. A. Balandin. "Electrical and noise characteristics of graphene field-effect transistors: ambient effects, noise sources and physical mechanisms." *Journal of Physics: Condensed Matter* 22, no. 39 (2010). 395302.

11. Schedin, F., A. K. Geim, S. V. Morozov, E. W. Hill, P. Blake, M. I. Katsnelson, and K. S. Novoselov. "Detection of individual gas molecules adsorbed on graphene." *Nature materials* 6, no. 9 (2007): 652-655.
12. Ferrari, Andrea C., et al. "Science and technology roadmap for graphene, related two-dimensional crystals, and hybrid systems." *Nanoscale* (2014).
13. Neto, AH Castro, F. Guinea, N. M. R. Peres, Kostya S. Novoselov, and Andre K. Geim. "The electronic properties of graphene." *Reviews of modern physics*81, no. 1 (2009): 109.
14. Wallace, Philip Richard. "The band theory of graphite." *Physical Review* 71, no. 9 (1947): 622.
15. Freitag, Marcus. "Graphene: nanoelectronics goes flat out." *Nature nanotechnology* 3, no. 8 (2008): 455-457.
16. Chen, Zhihong, and Joerg Appenzeller. "Mobility extraction and quantum capacitance impact in high performance graphene field-effect transistor devices." In *Electron Devices Meeting, 2008. IEDM 2008. IEEE International*, pp. 1-4. IEEE, 2008.
17. Hwang, E. H., and S. Das Sarma. "Acoustic phonon scattering limited carrier mobility in two-dimensional extrinsic graphene." *Physical Review B* 77, no. 11 (2008): 115449.
18. Adam, Shaffique, E. H. Hwang, V. M. Galitski, and S. Das Sarma. "A self-consistent theory for graphene transport." *Proceedings of the National Academy of Sciences* 104, no. 47 (2007): 18392-18397.
19. Stauber, T., N. M. R. Peres, and F. Guinea. "Electronic transport in graphene: A semiclassical approach including midgap states." *Physical Review B* 76, no. 20 (2007): 205423.
20. Hao, Yufeng, M. S. Bharathi, Lei Wang, Yuanyue Liu, Hua Chen, Shu Nie, Xiaohan Wang et al. "The role of surface oxygen in the growth of large single-crystal graphene on copper." *Science* 342, no. 6159 (2013): 720-723.
21. Zhang, Yuanbo, Victor W. Brar, Caglar Girit, Alex Zettl, and Michael F. Crommie. "Origin of spatial charge inhomogeneity in graphene." *Nature Physics*5, no. 10 (2009): 722-726.
22. Chen, J-H., C. Jang, S. Adam, M. S. Fuhrer, E. D. Williams, and Masa Ishigami. "Charged-impurity scattering in graphene." *Nature Physics* 4, no. 5 (2008): 377-381.
23. Berger, Claire, Zhimin Song, Tianbo Li, Xuebin Li, Asmerom Y. Ogbazghi, Rui Feng, Zhenting Dai et al. "Ultrathin epitaxial graphite: 2D electron gas properties and a route toward graphene-based nanoelectronics." *The Journal of Physical Chemistry B* 108, no. 52 (2004): 19912-19916.
24. Shivaraman, Shriram, M. V. S. Chandrashekhar, John J. Boeckl, and Michael G. Spencer. "Thickness estimation of epitaxial graphene on SiC using attenuation of substrate raman intensity." *Journal of electronic materials* 38, no. 6 (2009): 725-730.
25. Li, Xuesong, Weiwei Cai, Jinho An, Seyoung Kim, Junghyo Nah, Dongxing Yang, Richard Piner et al. "Large-area synthesis of high-quality and uniform graphene films on copper foils." *Science* 324, no. 5932 (2009): 1312-1314.
26. Zhang, Xingwang, Fei Meng, Jeffrey R. Christianson, Christian Arroyo-Torres, Mark A. Lukowski, Dong Liang, Jordan R. Schmidt, and Song Jin. "Vertical Heterostructures

of Layered Metal Chalcogenides by van der Waals Epitaxy."*Nano letters* 14, no. 6 (2014): 3047-3054.
27. Chan, Jack, Archana Venugopal, Adam Pirkle, Stephen McDonnell, David Hinojos, Carl W. Magnuson, Rodney S. Ruoff, Luigi Colombo, Robert M. Wallace, and Eric M. Vogel. "Reducing extrinsic performance-limiting factors in graphene grown by chemical vapor deposition." *ACS nano* 6, no. 4 (2012): 3224-3229.
28. Meric, Inanc, Cory R. Dean, Nicholas Petrone, Lei Wang, James Hone, Philip Kim, and Kenneth L. Shepard. "Graphene field-effect transistors based on boron–nitride dielectrics." *Proceedings of the IEEE* 101, no. 7 (2013): 1609-1619.
29. Wu, Wei, Zhihong Liu, Luis A. Jauregui, Qingkai Yu, Rajeev Pillai, Helin Cao, Jiming Bao, Yong P. Chen, and Shin-Shem Pei. "Wafer-scale synthesis of graphene by chemical vapor deposition and its application in hydrogen sensing." *Sensors and Actuators B: Chemical* 150, no. 1 (2010): 296-300.
30. Chu, Byung Hwan, C. F. Lo, Justin Nicolosi, C. Y. Chang, Victor Chen, W. Strupinski, S. J. Pearton, and F. Ren. "Hydrogen detection using platinum coated graphene grown on SiC." *Sensors and Actuators B: Chemical* 157, no. 2 (2011): 500-503.
31. Johnson, Jason L., Ashkan Behnam, S. J. Pearton, and Ant Ural. "Hydrogen Sensing Using Pd-Functionalized Multi-Layer Graphene Nanoribbon Networks."*Advanced Materials* 22, no. 43 (2010): 4877-4880.
32. Chen, Chun-Chung, Mehmet Aykol, Chia-Chi Chang, A. F. J. Levi, and Stephen B. Cronin. "Graphene-silicon Schottky diodes." *Nano letters* 11, no. 5 (2011): 1863-1867.
33. Li, Xinming, Hongwei Zhu, Kunlin Wang, Anyuan Cao, Jinquan Wei, Chunyan Li, Yi Jia, Zhen Li, Xiao Li, and Dehai Wu. "Graphene-On-Silicon Schottky Junction Solar Cells." *Advanced Materials* 22, no. 25 (2010): 2743-2748.
34. An, Xiaohong, Fangze Liu, Yung Joon Jung, and Swastik Kar. "Tunable graphene–silicon heterojunctions for ultrasensitive photodetection." *Nano letters*13, no. 3 (2013): 909-916.
35. Ren, Yujie, Shanshan Chen, Weiwei Cai, Yanwu Zhu, Chaofu Zhu, and Rodney S. Ruoff. "Controlling the electrical transport properties of graphene by in situ metal deposition." *Applied Physics Letters* 97, no. 5 (2010): 053107.
36. Johnson, Jason L., Ashkan Behnam, Yanbin An, S. J. Pearton, and Ant Ural. "Experimental study of graphitic nanoribbon films for ammonia sensing. "*Journal of Applied Physics* 109, no. 12 (2011): 124301.
37. Schaadt, D. M., B. Feng, and E. T. Yu. "Enhanced semiconductor optical absorption via surface plasmon excitation in metal nanoparticles." *Applied Physics Letters* 86, no. 6 (2005): 063106.
38. Glavin, Nicholas R., Michael L. Jespersen, Michael H. Check, Jianjun Hu, Al M. Hilton, Timothy S. Fisher, and Andrey A. Voevodin. "Synthesis of few-layer, large area hexagonal-boron nitride by pulsed laser deposition." *Thin Solid Films*572 (2014): 245-250.

Chapter 2:

1. Li, Xuesong, Weiwei Cai, Jinho An, Seyoung Kim, Junghyo Nah, Dongxing Yang, Richard Piner et al. "Large-area synthesis of high-quality and uniform graphene films on copper foils." *Science* 324, no. 5932 (2009): 1312-1314.
2. Ferrari, A. C., J. C. Meyer, V. Scardaci, C. Casiraghi, Michele Lazzeri, Francesco Mauri, S. Piscanec et al. "Raman spectrum of graphene and graphene layers." *Physical review letters* 97, no. 18 (2006): 187401.
3. Berciaud, Stéphane, Sunmin Ryu, Louis E. Brus, and Tony F. Heinz. "Probing the intrinsic properties of exfoliated graphene: Raman spectroscopy of free-standing monolayers." *Nano letters* 9, no. 1 (2008): 346-352.
4. Ferrari, Andrea C., and Denis M. Basko. "Raman spectroscopy as a versatile tool for studying the properties of graphene." *Nature nanotechnology* 8, no. 4 (2013): 235-246.
5. Malard, L. M., M. A. Pimenta, G. Dresselhaus, and M. S. Dresselhaus. "Raman spectroscopy in graphene." *Physics Reports* 473, no. 5 (2009): 51-87.
6. Ferrari, Andrea C. "Raman spectroscopy of graphene and graphite: disorder, electron–phonon coupling, doping and nonadiabatic effects." *Solid state communications* 143, no. 1 (2007): 47-57.
7. Chan, Jack, Archana Venugopal, Adam Pirkle, Stephen McDonnell, David Hinojos, Carl W. Magnuson, Rodney S. Ruoff, Luigi Colombo, Robert M. Wallace, and Eric M. Vogel. "Reducing extrinsic performance-limiting factors in graphene grown by chemical vapor deposition." *ACS nano* 6, no. 4 (2012): 3224-3229.
8. Saraswat, Krishna C. "How far can we push Si CMOS and what are the alternatives for future ULSI." In *Device Research Conference (DRC), 2014 72nd Annual*, pp. 3-4. IEEE, 2014.
9. D. K. Schroder, *Semiconductor material and device characterization*: John Wiley & Sons, 2006, Chapter 2.

Chapter 3:

1. Ferrari, Andrea C., Francesco Bonaccorso, Vladimir Falko, Konstantin S. Novoselov, Stephan Roche, Peter Bøggild, Stefano Borini et al. "Science and technology roadmap for graphene, related two-dimensional crystals, and hybrid systems." *Nanoscale* (2014).
2. Meric, Inanc, Cory R. Dean, Nicholas Petrone, Lei Wang, James Hone, Philip Kim, and Kenneth L. Shepard. "Graphene field-effect transistors based on boron–nitride dielectrics." *Proceedings of the IEEE* 101, no. 7 (2013): 1609-1619.
3. Watanabe, Kenji, Takashi Taniguchi, and Hisao Kanda. "Direct-bandgap properties and evidence for ultraviolet lasing of hexagonal boron nitride single crystal." *Nature materials* 3, no. 6 (2004): 404-409.
4. Giovannetti, Gianluca, Petr A. Khomyakov, Geert Brocks, Paul J. Kelly, and Jeroen van den Brink. "Substrate-induced band gap in graphene on hexagonal boron

nitride: Ab initio density functional calculations." *Physical Review B* 76, no. 7 (2007): 073103.
5. Geick, R., C. H. Perry, and G. Rupprecht. "Normal modes in hexagonal boron nitride." *Physical Review* 146, no. 2 (1966): 543.
6. Ohba, Nobuko, Kazutoshi Miwa, Naoyuki Nagasako, and Atsuo Fukumoto. "First-principles study on structural, dielectric, and dynamical properties for three BN polytypes." *Physical Review B* 63, no. 11 (2001): 115207.
7. Lipp, Alfred, Karl A. Schwetz, and Klaus Hunold. "Hexagonal boron nitride: fabrication, properties and applications." *Journal of the European Ceramic Society* 5, no. 1 (1989): 3-9.
8. Dean, C. R., A. F. Young, I. Meric, C. Lee, L. Wang, S. Sorgenfrei, K. Watanabe et al. "Boron nitride substrates for high-quality graphene electronics."*Nature nanotechnology* 5, no. 10 (2010): 722-726.
9. Yankowitz, Matthew, Jiamin Xue, Daniel Cormode, Javier D. Sanchez-Yamagishi, K. Watanabe, T. Taniguchi, Pablo Jarillo-Herrero, Philippe Jacquod, and Brian J. LeRoy. "Emergence of superlattice Dirac points in graphene on hexagonal boron nitride." *Nature Physics* 8, no. 5 (2012): 382-386.
10. Ortix, Carmine, Liping Yang, and Jeroen van den Brink. "Graphene on incommensurate substrates: trigonal warping and emerging Dirac cone replicas with halved group velocity." *Physical Review B* 86, no. 8 (2012): 081405.
11. Kindermann, M., Bruno Uchoa, and D. L. Miller. "Zero-energy modes and gate-tunable gap in graphene on hexagonal boron nitride." *Physical Review B* 86, no. 11 (2012): 115415.
12. Xue, Jiamin, Javier Sanchez-Yamagishi, Danny Bulmash, Philippe Jacquod, Aparna Deshpande, K. Watanabe, T. Taniguchi, Pablo Jarillo-Herrero, and Brian J. LeRoy. "Scanning tunnelling microscopy and spectroscopy of ultra-flat graphene on hexagonal boron nitride." *Nature materials* 10, no. 4 (2011): 282-285.
13. Decker, Régis, Yang Wang, Victor W. Brar, William Regan, Hsin-Zon Tsai, Qiong Wu, William Gannett, Alex Zettl, and Michael F. Crommie. "Local electronic properties of graphene on a BN substrate via scanning tunneling microscopy." *Nano letters* 11, no. 6 (2011): 2291-2295.
14. Park, Cheol-Hwan, Li Yang, Young-Woo Son, Marvin L. Cohen, and Steven G. Louie. "Anisotropic behaviours of massless Dirac fermions in graphene under periodic potentials." *Nature Physics* 4, no. 3 (2008): 213-217.
15. Wallbank, J. R., A. A. Patel, M. Mucha-Kruczyński, A. K. Geim, and V. I. Fal'ko. "Generic miniband structure of graphene on a hexagonal substrate."*Physical Review B* 87, no. 24 (2013): 245408.
16. Song, Li, Lijie Ci, Hao Lu, Pavel B. Sorokin, Chuanhong Jin, Jie Ni, Alexander G. Kvashnin et al. "Large scale growth and characterization of atomic hexagonal boron nitride layers." *Nano letters* 10, no. 8 (2010): 3209-3215.
17. Ismach, Ariel, Harry Chou, Domingo A. Ferrer, Yaping Wu, Stephen McDonnell, Herman C. Floresca, Alan Covacevich et al. "Toward the controlled synthesis of hexagonal boron nitride films." *ACS nano* 6, no. 7 (2012): 6378-6385.

18. Shi, Yumeng, Christoph Hamsen, Xiaoting Jia, Ki Kang Kim, Alfonso Reina, Mario Hofmann, Allen Long Hsu et al. "Synthesis of few-layer hexagonal boron nitride thin film by chemical vapor deposition." *Nano letters* 10, no. 10 (2010): 4134-4139.
19. Glavin, Nicholas R., Michael L. Jespersen, Michael H. Check, Jianjun Hu, Al M. Hilton, Timothy S. Fisher, and Andrey A. Voevodin. "Synthesis of few-layer, large area hexagonal-boron nitride by pulsed laser deposition." *Thin Solid Films* 572 (2014): 245-250.
20. Alam, Tarek, Baoming Wang, Raghu Pulavarthy, M. A. Haque, Christopher Muratore, Nicholas Glavin, Ajit K. Roy, and Andrey A. Voevodin. "Domain engineering of physical vapor deposited two-dimensional materials." *Applied Physics Letters* 105, no. 21 (2014): 213110.
21. N. Alem, R. Erni, C. Kisielowski, M.D. Rossell, W. Gannett, A. Zettl, Atomically thin hexagonal boron nitride probed by ultrahigh-resolution transmission electron microscopy, Phys. Rev. B Condens. Matter Mater. Phys. 80 (15) (2009) 155425.
22. A.G.F. Garcia, M. Neumann, F. Amet, J.R. Williams, K. Watanabe, T. Taniguchi, D. Goldhaber-Gordon, Effective cleaning of hexagonal boron nitride for graphene devices, Nano Lett. 12 (9) (2012) 4449.
23. Y. Wang, Z. Shi, J. Yin, Boron nitride nanosheets: large-scale exfoliation in methanesulfonic acid and their composites with polybenzimidazole, J. Mater. Chem. 21 (30) (2011) 11371.
24. P. Sutter, J. Lahiri, P. Zahl, B.Wang, E. Sutter, Scalable synthesis of uniform few-layer hexagonal boron nitride dielectric films, Nano Lett. 13 (1) (2013) 276.
25. M. Sajjad, G. Morell, P. Feng, Advance in novel boron nitride nanosheets to nanoelectronic device applications, ACS Appl. Mater. Interfaces 5 (11) (2013) 5051.
26. Y.C. Lin, N. Lu, N. Perea-Lopez, J. Li, Z. Lin, X. Peng, C.H. Lee, C. Sun, L. Calderin, P.N. Browning, M.S. Bresnehan, M.J. Kim, T.S. Mayer, M. Terrones, J.A. Robinson, Direct synthesis of van der Waals solids, ACS Nano 8 (4) (2014) 3715–3723.
27. M.S. Bresnehan, M.J. Hollander,M. Wetherington, K.Wang, T.Miyagi, G. Pastir, D.W. Snyder, J.J. Gengler, A.A. Voevodin, W.C. Mitchel, J.A. Robison, Prospects of direct growth boron nitride films as substrates for graphene electronics, J. Mater. Res. 29 (3) (2014) 459–471.
28. Nayfeh, Osama M., A. Glen Birdwell, Cheng Tan, Madan Dubey, Hemtej Gullapalli, Zheng Liu, Arava Leela Mohana Reddy, and Pulickel M. Ajayan. "Increased mobility for layer-by-layer transferred chemical vapor deposited graphene/boron-nitride thin films." *Applied Physics Letters* 102, no. 10 (2013): 103115.
29. Gorbachev, Roman V., Ibtsam Riaz, Rahul R. Nair, Rashid Jalil, Liam Britnell, Branson D. Belle, Ernie W. Hill et al. "Hunting for monolayer boron nitride: optical and Raman signatures." *Small* 7, no. 4 (2011): 465-468.

30. Mahvash, Farzaneh, Etienne Paradis, Dominique Drouin, Thomas Szkopek, and Mohamed Siaj. "Space-charge limited transport in large-area monolayer hexagonal boron nitride." Nano letters (2015).
31. Ghoneim, Mohamed T., Casey E. Smith, and Muhammad M. Hussain. "Simplistic graphene transfer process and its impact on contact resistance."*Applied Physics Letters* 102, no. 18 (2013): 183115.
32. Peng, Song-ang, Zhi Jin, Peng Ma, Da-yong Zhang, Jing-yuan Shi, Jie-bin Niu, Xuan-yun Wang et al. "The sheet resistance of graphene under contact and its effect on the derived specific contact resistivity." *Carbon* 82 (2015): 500-505.
33. Britnell, Liam, Roman V. Gorbachev, Rashid Jalil, Branson D. Belle, Fred Schedin, Mikhail I. Katsnelson, Laurence Eaves et al. "Electron tunneling through ultrathin boron nitride crystalline barriers." *Nano letters* 12, no. 3 (2012): 1707-1710.
34. Qi, Zhengqing John, Sung Ju Hong, Julio A. Rodríguez-Manzo, Nicholas J. Kybert, Rajatesh Gudibande, Marija Drndić, Yung Woo Park, and A. T. Johnson. "Electronic Transport in Heterostructures of Chemical Vapor Deposited Graphene and Hexagonal Boron Nitride." *Small* (2014).
35. Moser, Joel, Amelia Barreiro, and Adrian Bachtold. "Current-induced cleaning of graphene." *Applied Physics Letters* 91, no. 16 (2007): 163513.
36. Chowdhury, Sk Fahad, Sushant Sonde, Somayyeh Rahimi, Li Tao, Sanjay Banerjee, and Deji Akinwande. "Improvement of graphene field-effect transistors by hexamethyldisilazane surface treatment." *Applied Physics Letters* 105, no. 3 (2014): 033117.
37. Lafkioti, Myrsini, Benjamin Krauss, Timm Lohmann, Ute Zschieschang, Hagen Klauk, Klaus V. Klitzing, and Jurgen H. Smet. "Graphene on a hydrophobic substrate: doping reduction and hysteresis suppression under ambient conditions." *Nano letters* 10, no. 4 (2010): 1149-1153.
38. Asay, David B., and Seong H. Kim. "Evolution of the adsorbed water layer structure on silicon oxide at room temperature." *The Journal of Physical Chemistry B* 109, no. 35 (2005): 16760-16763.
39. Asay, David B., Anna L. Barnette, and Seong H. Kim. "Effects of Surface Chemistry on Structure and Thermodynamics of Water Layers at Solid− Vapor Interfaces." *The Journal of Physical Chemistry C* 113, no. 6 (2008): 2128-2133.
40. Leenaerts, O., B. Partoens, and F. M. Peeters. "Adsorption of H_2O, NH_3, CO, NO_2, and NO on graphene: A first-principles study." *Physical Review B*77, no. 12 (2008): 125416.
41. Wehling, T. O., M. I. Katsnelson, and A. I. Lichtenstein. "Adsorbates on graphene: Impurity states and electron scattering." *Chemical Physics Letters*476, no. 4 (2009): 125-134.
42. Wehling, Tim O., Alexander I. Lichtenstein, and Mikhail I. Katsnelson. "First-principles studies of water adsorption on graphene: The role of the substrate."*Applied Physics Letters* 93, no. 20 (2008): 202110-202110.

43. Konar, Aniruddha, Tian Fang, and Debdeep Jena. "Effect of high-κ gate dielectrics on charge transport in graphene-based field effect transistors." Physical Review B 82, no. 11 (2010): 115452.

Chapter 4:

1. Geim A K and Novoselov K. S. 2007 The rise of graphene Nature Mater. 6 pp 183-191.
2. Bolotin K I, Sikes K J, Hone J, Stormer H L and Kim P 2008 Temperature-dependent transport in suspended graphene Phys. Rev. Lett. 101 096802.
3. Schedin F, Geim A K, Morozov S V, Hill E W, Blake P, Katsnelson M I and Novoselov K S 2007 Detection of individual gas molecules adsorbed on graphene Nature Mater 6 pp 652-655.
4. Novoselov K S A, Geim A K, Morozov S, Jiang D, Grigorieva M K I, Dubonos S V and Firsov A A 2005 Two-dimensional gas of massless Dirac fermions in graphene Nature 438 pp 197-200.
5. Novoselov K S, Jiang D, Schedin F, Booth T J, Khotkevich V V, Morozov S V and Geim A K 2005 Two-dimensional atomic crystals Proceedings of the National Academy of Sciences of the United States of America 102 pp 10451-10453.
6. Zhang Y, Tan Y W, Stormer H L and Kim P 2005 Experimental observation of the quantum Hall effect and Berry's phase in graphene Nature 438 pp 201-204.
7. Nomani M W, Shishir R, Qazi M, Diwan D, Shields V B, Spencer M G, Tompa G S, Sbrockey N M and Koley G 2010 Highly sensitive and selective detection of NO2 using epitaxial graphene on 6H-SiC Sensors and Actuators B: Chemical 150 pp 301-307.
8. Potyrailo R A, Surman C, Nagraj N and Burns A 2011 Materials and transducers toward selective wireless gas sensing Chemical reviews 111 pp 7315-7354.
9. Rumyantsev S, Liu G, Shur M S, Potyrailo R A and Balandin A A 2012 Selective gas sensing with a single pristine graphene transistor Nano Lett. 12 pp 2294-2298.
10. Singh A K, Uddin M A, Tolson J T, Maire-Afeli H, Sbrockey N, Tompa G S, Spencer M G, Vogt T, Sudarshan T S and Koley G 2013 Electrically tunable molecular doping of graphene Appl. Phys. Lett. 102 pp 043101-043101.
11. Wu W, Liu Z, Jauregui L A, Yu Q, Pillai R, Cao H, Bao J, Chen Y P and Pei S S 2010 Wafer-scale synthesis of graphene by chemical vapor deposition and its application in hydrogen sensing Sensors and Actuators B 150 pp 296-300.
12. Chu B H, Lo C F, Nicolosi J, Chang C Y, Chen V, Strupinski W, Pearton S J and Ren F 2011 Hydrogen detection using platinum coated graphene grown on SiC Sensors and Actuators B 157 pp 500-503.
13. Johnson J L, Behnam A, Pearton S J and Ural A 2010 Hydrogen Sensing Using Pd-Functionalized Multi-Layer Graphene Nanoribbon Networks Adv. Mater. 22 pp 4877-4880.
14. Wehling T O, Yuan S, Lichtenstein A I, Geim A K and Katsnelson M I 2010 Resonant scattering by realistic impurities in graphene Phys. Rev. Lett. 105 056802.

15. Sarkar S, Zhang H, Huang J W, Wang F, Bekyarova E, Lau C N and Haddon R C 2012 Organometallic Hexahapto Functionalization of Single Layer Graphene as a Route to High Mobility Graphene Devices Adv. Mater. 25 1131.
16. Chan J, Venugopal A, Pirkle A, McDonnell S, Hinojos D, Magnuson C W, Ruoff R S, Colombo L, Wallace R M and Vogel E M 2012 Reducing extrinsic performance-limiting factors in graphene grown by chemical vapor deposition ACS Nano 6 pp 3224-3229.
17. Tedesco J L, VanMil B L, Myers-Ward R L, McCrate J M, Kitt S A, Campbell P M, Jernigan G G, Culbertson J C, Eddy C R and Gaskill D K 2009 Hall effect mobility of epitaxial graphene grown on silicon carbide Appl. Phys. Lett. 9512 pp 122102
18. Zhang H, Bekyarova E, Huang J W, Zhao Z, Bao W, Wang F, Haddon R C and Lau C N 2011 Aryl functionalization as a route to band gap engineering in single layer graphene devices Nano Lett. 11 pp 4047-4051.
19. Chen C C, Aykol M, Chang C C, Levi A F J and Cronin S B 2011 Graphene-silicon Schottky diodes Nano Lett. 11 pp 1863-1867.
20. Li X, Zhu H, Wang K, Cao A, Wei J, Li C, Yi J, Li Z, Li X and Wu D 2010 Graphene-On-Silicon Schottky Junction Solar Cells Adv. Mater. 22 pp 2743-2748.
21. Yang H, Heo J, Park S, Song H J, Seo D H, Byun K E, Kim P, Yoo I, Chung H J and Kim K 2012 Graphene barristor, a triode device with a gate-controlled Schottky barrier Science 336 pp 1140-1143.
22. An X, Liu F, Jung Y J and Kar S 2013 Tunable Graphene–Silicon Heterojunctions for Ultrasensitive Photodetection Nano Lett. 13 pp 909-916.
23. Kim H Y, Lee K, McEvoy N, Yim C and Duesberg G S 2013 Chemically Modulated Graphene Diodes Nano Lett. 13 pp 2182-2188.
24. Glueckauf E and Kitt G P 1957 The hydrogen content of atmospheric air at ground level Q. J. R. Meteorol. Soc. 83 pp 522-528.
25. Li X et al. 2009 Large-area synthesis of high-quality and uniform graphene films on copper foils Science 324 pp 1312-1314.
26. Bhaviripudi S, Jia X, Dresselhaus M S and Kong J 2010 Role of kinetic factors in chemical vapor deposition synthesis of uniform large area graphene using copper catalyst Nano Lett. 10 pp 4128-4133.
27. Suk J W, Kitt A, Magnuson C W, Hao Y, Ahmed S, An J H, Swan A K, Goldberg B B and Ruoff R S 2011 Transfer of CVD-grown monolayer graphene onto arbitrary substrates. ACS Nano 5 pp 6916-6924.
28. Ferrari, A. C. 2007 Raman spectroscopy of graphene and graphite: disorder, electron–phonon coupling, doping and nonadiabatic effects Solid State Communications 143 pp 47-57.
29. Ferrari A C et al. 2006 Raman spectrum of graphene and graphene layers Phys. Rev. Lett. 97 187401.
30. Sze S M 1981 Physics of Semiconductor Devices (John Wiley: New York) 245.
31. Mishra U K and Singh J 2007 Semiconductor Device Physics and Design (Springer: Dordrecht, The Netherlands) 226.

32. Tung R T 2001 Recent Advances in Schottky Barrier Concepts Mater. Sci. Eng. R 35 1.
33. Tongay S, Lemaitre M, Miao X, Gila B, Appleton B R and Hebard A F 2012 Rectification at graphene-semiconductor interfaces: zero-gap semiconductor-based diodes Phys. Rev. X 2 011002.
34. Shivaraman S, Herman L H, Rana F, Park J and Spencer M G 2012 Schottky barrier inhomogeneities at the interface of few layer epitaxial graphene and silicon carbide Appl. Phys. Lett. 100 pp 183112-183112.
35. Ren Y, Chen S, Cai W, Zhu Y, Zhu C and Ruoff R S 2010 Controlling the electrical transport properties of graphene by in situ metal deposition Appl. Phys. Lett. 97 pp 053107-053107.
36. Michaelson H B 1977 The work function of the elements and its periodicity J. Appl. Phys. 48 pp 4729-4733.
37. Giovannetti G, Khomyakov P A, Brocks G, Karpan V M, Van den Brink J and Kelly P J 2008 Doping graphene with metal contacts Phys. Rev. Lett. 101 026803.
38. Chung M G et al. 2012 Flexible hydrogen sensors using graphene with palladium nanoparticle decoration Sensors and Actuators B 169 pp 387-392.
39. Skucha K, Fan Z, Jeon K, Javey A and Boser B 2010 Palladium/silicon nanowire Schottky barrier-based hydrogen sensors Sensors and Actuators B 145 pp 232-238.
40. Chou Y I, Chen C M, Liu W C and Chen H I 2005 A new Pd-InP Schottky hydrogen sensor fabricated by electrophoretic deposition with Pd nanoparticles IEEE Electron Device Letter, 26 pp 62-65.
41. Wu W, Wen X, and Wang Z L 2013 Taxel-Addressable Matrix of Vertical-Nanowire Piezotronic Transistors for Active and Adaptive Tactile Imaging Science 340 pp 952-957.
42. Niu S, Hu Y, Wen X, Zhou Y, Zhang F, Lin L, Wang S and Wang Z L 2013 Enhanced Performance of Flexible ZnO Nanowire Based Room-Temperature Oxygen Sensors by Piezotronic Effect Adv. Mater. 25 pp 3701–3706.
43. An Y, Behnam A, Pop E and Ural A 2013 Metal-semiconductor-metal photodetectors based on graphene/p-type silicon Schottky junctions Appl. Phys. Lett. 102 pp 013110-013110.
44. Lundström I and Söderberg D 1982 Hydrogen sensitive mos-structures part 2: characterization Sensors and Actuators 2 pp 105-138.
45. Chu B H, Nicolosi J, Lo C F, Strupinski W, Pearton S J and Ren F 2011 Effect of coated platinum thickness on hydrogen detection sensitivity of graphene-based sensors Electrochemical and Solid-State Letters 14 pp K43-K45.
46. R. S. Muller, T. I. Kamins, M. Chan, Metal-Semiconductor Contacts. In *Device Electronics for Integrated Circuits*, John Wiley, NY, USA **2003**.
47. Tongay, S., T. Schumann, X. Miao, B. R. Appleton, and A. F. Hebard. "Tuning Schottky diodes at the many-layer-graphene/semiconductor interface by doping." *Carbon* 49, no. 6 (2011): 2033-2038.

48. Singh, Amol, Md Uddin, Tangali Sudarshan, and Goutam Koley. "Tunable Reverse-Biased Graphene/Silicon Heterojunction Schottky Diode Sensor."*Small* 10, no. 8 (2014): 1555-1565.

Chapter 5:

1. Yang, Heejun, Jinseong Heo, Seongjun Park, Hyun Jae Song, David H. Seo, Kyung-Eun Byun, Philip Kim, InKyeong Yoo, Hyun-Jong Chung, and Kinam Kim. "Graphene barristor, a triode device with a gate-controlled Schottky barrier." *Science* 336, no. 6085 (2012): 1140-1143.
2. Liu, Fangze, and Swastik Kar. "Quantum Carrier Reinvestment-Induced Ultrahigh and Broadband Photocurrent Responses in Graphene–Silicon Junctions." *ACS nano* 8, no. 10 (2014): 10270-10279.
3. Singh, Amol, Md Uddin, Tangali Sudarshan, and Goutam Koley. "Tunable Reverse-Biased Graphene/Silicon Heterojunction Schottky Diode Sensor."*Small* 10, no. 8 (2014): 1555-1565.
4. Ren, Yujie, Shanshan Chen, Weiwei Cai, Yanwu Zhu, Chaofu Zhu, and Rodney S. Ruoff. "Controlling the electrical transport properties of graphene by in situ metal deposition." *Applied Physics Letters* 97, no. 5 (2010): 053107.
5. Johnson, Jason L., Ashkan Behnam, Yanbin An, S. J. Pearton, and Ant Ural. "Experimental study of graphitic nanoribbon films for ammonia sensing."*Journal of Applied Physics* 109, no. 12 (2011): 124301.
6. Uddin, Md Ahsan, Amol Kumar Singh, Tangali S. Sudarshan, and Goutam Koley. "Functionalized graphene/silicon chemi-diode H2 sensor with tunable sensitivity." *Nanotechnology* 25, no. 12 (2014): 125501.
7. Sarkar, Deblina, Xuejun Xie, Jiahao Kang, Haojun Zhang, Wei Liu, Jose Navarrete, Martin Moskovits, and Kaustav Banerjee. "Functionalization of Transition Metal Dichalcogenides with Metallic Nanoparticles: Implications for Doping and Gas-Sensing." *Nano Letters* (2015).
8. Yim, Chanyoung, Niall McEvoy, and Georg S. Duesberg. "Characterization of graphene-silicon Schottky barrier diodes using impedance spectroscopy."*Applied Physics Letters* 103, no. 19 (2013): 193106.
9. Fattah, Ali, Saeid Khatami, Carmen C. Mayorga-Martinez, Mariana Medina-Sánchez, Luis Baptista-Pires, and Arben Merkoçi. "Graphene/Silicon Heterojunction Schottky Diode for Vapors Sensing Using Impedance Spectroscopy." *Small* 10, no. 20 (2014): 4193-4199.
10. S. M. Sze and K. K. Ng, *Physics of semiconductor devices*: John Wiley & Sons, 2006.
11. Lundström, Ingemar, Anita Spetz, Fredrik Winquist, U. Ackelid, and Hans Sundgren. "Catalytic metals and field-effect devices—a useful combination."*Sensors and Actuators B: Chemical* 1, no. 1 (1990): 15-20.

12. Lechuga, Laura M., A. Calle, Dolores Golmayo, and F. Briones. "Different catalytic metals (Pt, Pd and Ir) for GaAs Schottky barrier sensors." *Sensors and Actuators B: Chemical* 7, no. 1 (1992): 614-618.
13. Johnson, Jason L., Ashkan Behnam, Yanbin An, S. J. Pearton, and Ant Ural. "Experimental study of graphitic nanoribbon films for ammonia sensing. "*Journal of Applied Physics* 109, no. 12 (2011): 124301.
14. Xia, Fengnian, Vasili Perebeinos, Yu-ming Lin, Yanqing Wu, and Phaedon Avouris. "The origins and limits of metal-graphene junction resistance." *Nature nanotechnology* 6, no. 3 (2011): 179-184.
15. Borini, Stefano, Richard White, Di Wei, Michael Astley, Samiul Haque, Elisabetta Spigone, Nadine Harris, Jani Kivioja, and Tapani Ryhänen. "Ultrafast graphene oxide humidity sensors." *ACS nano* 7, no. 12 (2013): 11166-11173.

Chapter 6:

1. Geim, Andre K., and Konstantin S. Novoselov. "The rise of graphene." *Nature materials* 6, no. 3 (2007): 183-191.
2. Ferrari, Andrea C., Francesco Bonaccorso, Vladimir Falko, Konstantin S. Novoselov, Stephan Roche, Peter Bøggild, Stefano Borini et al. "Science and technology roadmap for graphene, related two-dimensional crystals, and hybrid systems." *Nanoscale* (2014).
3. Uddin, Md Ahsan, Amol Kumar Singh, Tangali S. Sudarshan, and Goutam Koley. "Functionalized graphene/silicon chemi-diode H2 sensor with tunable sensitivity." *Nanotechnology* 25, no. 12 (2014): 125501.
4. Ren, Yujie, Shanshan Chen, Weiwei Cai, Yanwu Zhu, Chaofu Zhu, and Rodney S. Ruoff. "Controlling the electrical transport properties of graphene by in situ metal deposition." Applied Physics Letters 97, no. 5 (2010): 053107.
5. Sarkar, Deblina, Xuejun Xie, Jiahao Kang, Haojun Zhang, Wei Liu, Jose Navarrete, Martin Moskovits, and Kaustav Banerjee. "Functionalization of Transition Metal Dichalcogenides with Metallic Nanoparticles: Implications for Doping and Gas-Sensing." Nano Letters (2015).
6. Schaadt, D. M., B. Feng, and E. T. Yu. "Enhanced semiconductor optical absorption via surface plasmon excitation in metal nanoparticles." Applied Physics Letters 86, no. 6 (2005): 063106.
7. Johnson, Jason L., Ashkan Behnam, Yanbin An, S. J. Pearton, and Ant Ural. "Experimental study of graphitic nanoribbon films for ammonia sensing. "Journal of Applied Physics 109, no. 12 (2011): 124301.
8. Zhu, Wenjuan, Vasili Perebeinos, Marcus Freitag, and Phaedon Avouris. "Carrier scattering, mobilities, and electrostatic potential in monolayer, bilayer, and trilayer graphene." *Physical Review B* 80, no. 23 (2009): 235402.
9. Van Zeghbroeck, Bart. "Principles of electronic devices." *University of Colorado* (2011), Chapter 2.

10. Ferrari, A. C., J. C. Meyer, V. Scardaci, C. Casiraghi, Michele Lazzeri, Francesco Mauri, S. Piscanec et al. "Raman spectrum of graphene and graphene layers." Physical review letters 97, no. 18 (2006): 187401.
11. Chen, Jian-Hao, Chaun Jang, Shudong Xiao, Masa Ishigami, and Michael S. Fuhrer. "Intrinsic and extrinsic performance limits of graphene devices on SiO2." *Nature nanotechnology* 3, no. 4 (2008): 206-209.
12. Fratini, Simone, and F. Guinea. "Substrate-limited electron dynamics in graphene." *Physical Review B* 77, no. 19 (2008): 195415.
13. Rotkin, Slava V., Vasili Perebeinos, Alexey G. Petrov, and Phaedon Avouris. "An essential mechanism of heat dissipation in carbon nanotube electronics."*Nano letters* 9, no. 5 (2009): 1850-1855.
14. Ohta, Taisuke, Aaron Bostwick, Jessica L. McChesney, Thomas Seyller, Karsten Horn, and Eli Rotenberg. "Interlayer interaction and electronic screening in multilayer graphene investigated with angle-resolved photoemission spectroscopy." *Physical Review Letters* 98, no. 20 (2007): 206802.
15. Guinea, F. "Charge distribution and screening in layered graphene systems. "*Physical Review B* 75, no. 23 (2007): 235433.
16. D. Ferry, Transport in Nanostructure, Cambridge University Press, Cambridge, England, 2009, Chap. 2.
17. Hwang, E. H., and S. Das Sarma. "Screening-induced temperature-dependent transport in two-dimensional graphene." *Physical Review B* 79, no. 16 (2009): 165404.
18. L. Pietronero, S. Strässler, H. R. Zeller, and M. J. Rice, *Physical Review B* 22 (1980): 904.
19. Du, Xu, Ivan Skachko, Anthony Barker, and Eva Y. Andrei. "Approaching ballistic transport in suspended graphene." *Nature nanotechnology* 3, no. 8 (2008): 491-495.
20. Hwang, E. H., and S. Das Sarma. "Acoustic phonon scattering limited carrier mobility in two-dimensional extrinsic graphene." *Physical Review B* 77, no. 11 (2008): 115449.
21. Giovannetti, G., P. A. Khomyakov, G. Brocks, V. M. Karpan, J. Van den Brink, and P. J. Kelly. "Doping graphene with metal contacts." *Physical Review Letters* 101, no. 2 (2008): 026803.
22. Greenwood, Norman N.; Earnshaw, Alan (1997). *Chemistry of the Elements,* 2nd Edition, Butterworth-Heinemann. pp. 1150–151.
23. Vargas, W. E., I. Rojas, D. E. Azofeifa, and N. Clark. "Optical and electrical properties of hydrided palladium thin films studied by an inversion approach from transmittance measurements." *Thin Solid Films* 496, no. 2 (2006): 189-196.
24. Jena, Debdeep, and Aniruddha Konar. "Enhancement of carrier mobility in semiconductor nanostructures by dielectric engineering." *Physical review letters* 98, no. 13 (2007): 136805.
25. Hollander, Matthew J., Michael LaBella, Zachary R. Hughes, Michael Zhu, Kathleen A. Trumbull, Randal Cavalero, David W. Snyder et al. "Enhanced transport and transistor performance with oxide seeded high-κ gate dielectrics on wafer-scale epitaxial graphene." *Nano letters* 11, no. 9 (2011): 3601-3607.

26. Nah, Junghyo, S. Bala Kumar, Hui Fang, Yu-Ze Chen, Elena Plis, Yu-Lun Chueh, Sanjay Krishna, Jing Guo, and Ali Javey. "Quantum size effects on the chemical sensing performance of two-dimensional semiconductors." *The Journal of Physical Chemistry C* 116, no. 17 (2012): 9750-9754.
27. Konar, Aniruddha, Tian Fang, and Debdeep Jena. "Effect of high-κ gate dielectrics on charge transport in graphene-based field effect transistors."*Physical Review B* 82, no. 11 (2010): 115452.
28. Bresnehan, Michael S., Matthew J. Hollander, Maxwell Wetherington, Michael LaBella, Kathleen A. Trumbull, Randal Cavalero, David W. Snyder, and Joshua A. Robinson. "Integration of hexagonal boron nitride with quasi-freestanding epitaxial graphene: toward wafer-scale, high-performance devices." *ACS nano*6, no. 6 (2012): 5234-5241.
29. Hollander, Matthew J., Ashish Agrawal, Michael S. Bresnehan, Michael LaBella, Kathleen A. Trumbull, Randal Cavalero, David W. Snyder, Suman Datta, and Joshua A. Robinson. "Heterogeneous integration of hexagonal boron nitride on bilayer quasi-free-standing epitaxial graphene and its impact on electrical transport properties." *physica status solidi (a)* 210, no. 6 (2013): 1062-1070.

Chapter 7:

1. Britnell, L., R. V. Gorbachev, R. Jalil, B. D. Belle, F. Schedin, A. Mishchenko, T. Georgiou et al. "Field-effect tunneling transistor based on vertical graphene heterostructures." *Science* 335, no. 6071 (2012): 947-950.